



MASTER'S THESIS

Ultrascaled Germanium Nanowires for Highly Sensitive and Spatially Resolved Photon Detection

submitted in partial fulfillment
of the requirements of the degree of
Master of Science

at Technische Universität Wien
Institute of Solid State Electronics

under supervision of
Ao.Univ.Prof. Dipl.Ing. Dr.techn. Alois Lugstein

by
Philipp Staudinger, BSc
Matr.-Nr. 1155653
Pürstling 16
4844 Regau

Vienna, December 2016

Statutory Declaration

I declare, that I have authored the present work independently according to the code of conduct, that I have not used other than the declared sources and that I have explicitly marked all material quoted either literally or by content from the used sources. This work was not yet submitted to any examination procedure neither in Austria, nor in any other country.

Vienna, December 2016

.....

Philipp Staudinger

Abstract

Low dimensional nanostructures such as semiconductor nanowires (NW) have recently attracted increasing attention for their potential use as photodetectors in future optical on-chip interconnectors. In particular, germanium (Ge) may be a promising material, due to its CMOS compatibility and exceptional electrical and optical properties. However, the application of Ge NWs as highly sensitive photoconductive elements has been largely overlooked up till now.

This work is dedicated to the systematic study of the electro-optical properties of vapor-liquid-solid (VLS) grown Ge NWs. Therefore, monolithic Al-Ge-Al NW heterostructures featuring abrupt interfaces and reliable high- κ passivation were established during the course of this thesis. The employed fabrication techniques thereby allowed for the formation of ultrasmall Ge segments without being limited by the alignment of a lithography tool. For such NW systems integrated in back gated field effect transistors, transfer characteristics revealed p-type behavior, which is attributed to trapping effects at the surface. Further, by controlling the charge carrier density through electrostatic gating, a time-dependent change in conductivity over more than 3 orders of magnitude could be observed, with relaxation times in the range of several minutes. To explain this phenomenon, a model was developed in which the slow redistribution of surface charges compensates external electrical fields on the longterm.

It was shown that the interplay of electrostatic gating and trap population can cause the charge transport to be electron dominated for several minutes, which was substantiated by the observation of negative differential resistance (NDR) in this regime. Further, low temperature measurements confirmed the proposed kinetic trapping barriers and numerous optical experiments demonstrated dynamic behavior as expected from trapping time constants of surface states in GeO_x . Optical experiments were carried out by using a specifically designed measurement setup featuring a spectrally tunable laser source and a lock-in amplifier. Investigations revealed photoconductive gains exceeding 10^7 , which is, to the best of my knowledge, the highest ever reported in Ge NWs. In agreement with literature, this was attributed to the photo-enhanced trapping of charge carriers at the surface. Moreover, this high sensitivity remains effective for the whole visible spectral range and for modulation frequencies up to 10 kHz. By systematically reducing channel lengths, ultrasmall photodetectors could be established with feature sizes far below the diffraction limit of incident light.

Acknowledgments

This diploma project and my whole studies would not have been possible without the guidance and support of many individuals. It is a pleasure for me to convey my gratitude and appreciation to all of them in this acknowledgment.

First, I would like to express my utmost gratitude to my supervisor Alois Lugstein for his continuous advice and encouragement throughout the course of this thesis. Thank you for providing an inspiring and motivating environment, for your everlasting enthusiasm and making my time in this group most pleasant and exciting.

Many thanks go in particular to my colleague and advisor Johannes Greil, who introduced me into the topic and guided me through the steps required to complete this thesis. Thank you for your valuable ideas, helpful advices and constant support.

I am very thankful to Masiar Sistani for allowing me to use his devices and introducing me to all the nanofabrication processes required in order to fabricate them by myself. It was a great pleasure for me to work with you.

Further on, I would like to thank all my colleagues at the Institute of Solid State Electronics and the Center for Micro- and Nanostructures for their persistent assistance and enlightening discussions. Thank you all for making this institute an amazing place to work at.

My deepest gratitude goes to my family for their unconditionally love and encouragement throughout my life. Without their support, both spiritually and materially, I would have never come this far.

Last but not least I would like to thank Viktoria for always giving me strength and joy and for being there when I needed someone to talk to.

Contents

1	Introduction	1
2	Theory	3
2.1	Nanowires	4
2.1.1	Properties of 1D Nanostructures	4
2.1.2	Nanowire Synthesis	5
2.2	Germanium	6
2.3	Electronic Properties of Semiconductors	8
2.3.1	Band Structure	8
2.3.2	Carrier Concentration	9
2.3.3	Charge Carrier Transport	12
2.3.4	Recombination in Semiconductors	14
2.3.5	Light Absorption in Semiconductors	16
2.3.6	Negative Differential Resistance	18
2.4	Surface Trapping in Germanium	19
2.4.1	Trapping Mechanism	19
2.4.2	Oxide Traps	21
2.4.3	Germanium Surface	22
2.4.4	Surface Charge Induced Band Bending	23
2.4.5	Trapping in Nanowires	25
2.5	Nanowire Photodetectors	26
2.5.1	Photoconducting Mechanism	27
2.5.2	Photoconductive Gain in Nanowires	29
2.5.3	Light Absorption in Nanowires	31

3	Experimental	35
3.1	Device Integration	36
3.2	Electrical Characterization	39
3.2.1	I/V Characteristics	40
3.2.2	Transfer Characteristics	41
3.2.3	Transient Characteristics	41
3.2.4	Characterization at Cryogenic Temperatures	42
3.2.5	Negative Differential Resistance	42
3.3	Optical Characterization	42
3.3.1	I/V Characteristics under Illumination	44
3.3.2	Laser Beam Power Dependent Measurements	45
3.3.3	Modulation Frequency Dependent Measurements	46
3.3.4	Wavelength Dependent Measurements	46
3.3.5	Lock-In Amplifier Measurement Technique	47
3.3.6	Determination of the Laser Beam Profile	48
3.3.7	Calculation of the Photoconductive Gain	49
4	Results and Discussion	53
4.1	Electrical Characterization	54
4.1.1	I/V Characteristics	54
4.1.2	Transfer Characteristics	57
4.1.3	Transient Characteristics	59
4.1.4	Trapping Time Constants	64
4.1.5	Characterization at Cryogenic Temperatures	65
4.1.6	Negative Differential Resistance	67
4.2	Optical Characterization	69
4.2.1	I/V Characteristics under Illumination	70
4.2.2	Dynamic Response of the Photocurrent	71
4.2.3	Low Power Measurements	75
4.2.4	Photoconductive Gain in Germanium Nanowires	77
4.2.5	Wavelength Dependent Measurements	79
5	Conclusion and Outlook	81

List of Figures	83
List of Tables	87
Appendix	89
A Device Processing	89
B Symbols	96
C Abbreviations	99
References	101

Introduction

Already in 1965, Gordon E. Moore published his prediction that the number of transistors on a single chip will double approximately every two years [1]. By continuously shrinking feature sizes and thus increasing operation frequencies of integrated circuits (IC), this astonishingly simple yet profound prognosis remained valid for more than five decades [2, 3]. As conventional planar CMOS technology followed this rapid downscaling, various issues arose and new materials and device concepts emerged in order to further satisfy this so-called “Moore’s Law”, including strained silicon [4], high- κ metal gate transistors [5] and most recently the integration of the non-planar tri-gate architecture [6]. Today, interconnects play an increasingly important role when it comes to design criteria such as delay time, power consumption, bandwidth and noise, and have become the primary bottleneck in IC design [7, 8]. For conventional copper based metalizations, it becomes more and more challenging to satisfy these requirements, as they suffer from scaling due to electromagnetic interferences [9] and increasing resistances [10] by reducing dimensions. Thus, novel concepts for on-chip communication are required in order to overcome current limitations of data rates in computers and in general high speed data processing.

Intrachip optical interconnects offer the promise of decreasing time delays and providing higher bandwidth at lower power consumption, while simultaneously being persistent to interferences such as they occur in electrical wires. Thus, they have the potential to ultimately solve the interconnect bottleneck and are considered as promising candidates for future generations of high performance ICs [11]. However, wavelengths of light are more than one order of magnitude larger than current

feature sizes, leading to tremendous challenges both technological and architectural. While the guiding of light with mode confinement below the diffraction limit has been repeatedly shown in the past by using e.g. plasmonic waveguides [12–14], the generation, modulation and detection of light at such dimensions remains challenging. Semiconductor NWs are considered as most promising candidates for these missing building blocks due to their compact footprints and unique properties, which has led to remarkable research progress in this area during the last few years [15–19].

Recently, especially Ge NWs gained increasing attention, due to their CMOS compatibility and superior electrical and optical properties [20, 21]. The possibility of tuning Ge NWs to be direct semiconductors by straining [22] or alloying [23], combined with their high surface to volume ratio allows both the efficient emission and detection of light at sizes well below the diffraction limit [24]. By exploiting a thermal exchange reaction between Al and Ge [25], the fabrication of short semiconductor segments has been shown [26], giving an ideal platform for the study of photoconductive properties of Ge at sizes desired for the integration into modern CMOS devices without being limited by the resolution of the lithography system. Besides their use as building blocks for optical interconnects, ultra-sensitive Ge NW photodetectors may also find applications in other areas. Their extremely large photosensitivity could for example ultimately enable single-photon detection at room temperature, which could further pave the way towards quantum computing [27]. Furthermore, combined with their potential for dense spatial integration, optical image sensors featuring spatial sensitivities in sub-wavelength range are conceivable [28]. By using light sensitive quantum structures enabling ballistic transport, the exploration of completely novel device concepts such as the light effect transistor (LET) can be achieved [29], which could pave the way towards optical logic gates and even optical computing [30, 31].

The aim of this work is to explore photoconducting properties of Ge NWs in the context of surface related trapping effects and to study their applicability for key elements in future ICs. To do so, Al-Ge-Al NW heterostructures with defined geometry are fabricated by using vapor-liquid-solid (VLS) grown Ge NWs combined with a sophisticated integration scheme. The electrical as well as optical properties seem to critically depend on surface trapping effects, which is why they are studied beforehand. Subsequently, optical measurements are carried out on a specifically designed setup in order to deduce variable properties such as the photoconductive gain. At the beginning of this work, theoretical aspects required for the study on Ge NWs are reviewed. This is followed by an overview on the experimental methods employed in device integration and characterization. Experimental results are discussed subsequently, followed by a short conclusion in the last chapter.

Theory

The following chapter addresses the theoretical aspects needed for the work on Ge NWs with special attention to trap related effects and light absorption. In the first section a brief motivation for NWs in general and their applications is given followed by theoretical aspects of NW synthesis with focus on the VLS growth. After discussing the basic properties of Ge in the second part of this chapter, an overview of fundamental semiconductor physics is presented. Further on, surface trapping in Ge and its consequences on electrical transport in NWs is reviewed. The last section deals with theoretical aspects on photodetectors and how surface trapping can be exploited for achieving high photoconductive gain.

2.1 Nanowires

Nanowires (NW) are commonly defined as rod-like nanostructures with diameters below 100 nm and lengths exceeding several micrometers. In very thin wires, the momentum of an electron is confined in two dimensions and the movement of charge carriers can therefore only follow one direction, which is why NWs are often referred to as quasi one-dimensional (1D). This reduction in dimensionality results in unique size dependent effects, which drastically change the electrical, chemical, and mechanical properties of the materials involved [32]. Further, very thin NWs allow even the direct observation of various quantum effects, which opens a highly interesting research field for both experimentalists and theorists.

2.1.1 Properties of 1D Nanostructures

Many electrical and optical properties of semiconductor materials are primarily determined by the electronic density of states $D(E)$, which describes the number of possible energy states per unit energy and volume. For bulk material (3D), $D(E)$ is a continuous value increasing monotonically with E , as is shown in figure 2.1. By reducing dimensions, quantum confinement takes place leading to a reduction of the overall number of allowed energy states and an increasingly discretized curve shape of $D(E)$. Eventually, in 0D systems, such as atoms or quantum dots, there is only a

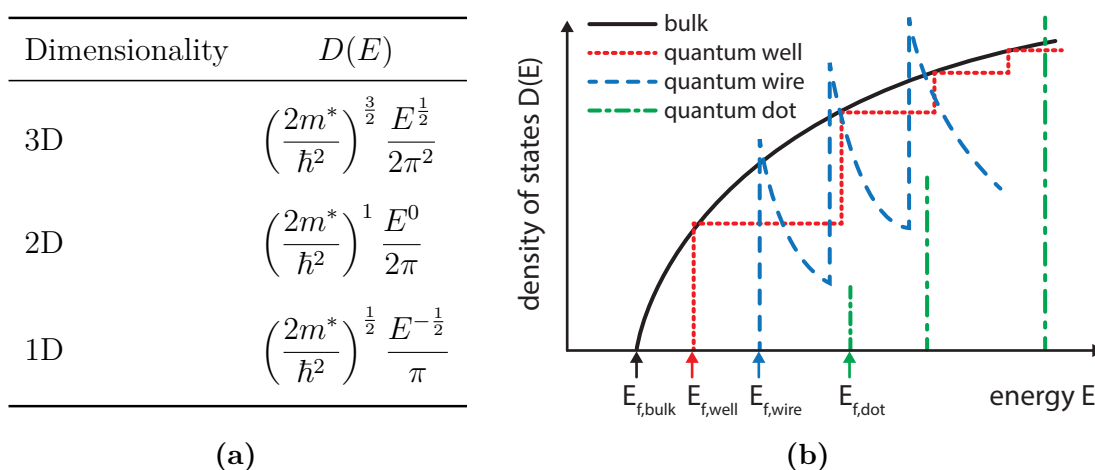


Figure 2.1: (a) Theoretical expression and (b) qualitative diagram of the density of states of different nanostructures compared to bulk material showing the effects of dimensionality on basic material properties. Image adapted from [33].

discrete number of allowed energies available to be occupied by electrons (indicated by the vertical green lines in figure 2.1b) giving rise to many possible application such as the single electron transistor [34].

In 1D structures, sharp spikes of $D(E)$ appear at certain energies which lead to strong signals in various electrical and optical measurements. Also the band gap tends to be higher than in bulk material and can be further tuned for specific applications by controlling the dimensions of the NW [32]. Furthermore, their high surface to volume ratio causes their properties to be predominately defined by the surface area rather than the material itself, which results in interesting effects depending on diameter and surface conditions. Because of these unique properties combined with the huge design freedom concerning material and dimensions, NWs have received significant research interest over the past decades [35] and are promising candidates for many electronic and photonic applications such as gate-all-around transistors [36], single photon detectors [37], solar cells [38] and batteries [39], to name but a few.

2.1.2 Nanowire Synthesis

NW synthesis can be accomplished by a large variety of technologies including several top-down (e.g. optical or electron beam lithography in combination with anisotropic etching techniques [40]) and bottom-up approaches such as the solid-liquid-solid [41], the solution-liquid-solid [42] or the vapor-liquid-solid (VLS) mechanism. The VLS growth mechanism introduced by Wagner and Ellis in 1964 [43] is the most common among them allowing the direct growth of a high variety of materials including Si [44], Ge [45], GaAs [46] and ZnO [47] as well as in-situ doping [48] and the growth of axial [49] or radial [50] heterostructures. Since the Ge NWs used in the experiments presented in this thesis were also grown by this technique, some peculiarities will be discussed in more detail.

The VLS mechanism is based on the well-known chemical vapor deposition (CVD) technique using a metal nanoparticle as catalyst. Most commonly, gold is sputtered on a Si substrate and annealed to form nano-droplets (figure 2.2a). For Ge NW growth, the substrate is subsequently put into a germane atmosphere and heated up above 360 °C, which is the eutectic temperature of the Au-Ge system [51]. Due to the adsorption and diffusion of Ge into the droplet, an alloy forms, which is liquid at a Ge concentration of 28 % [51] (figure 2.2b). The continuous supply of germane causes then supersaturation and nucleation of Ge on the substrate resulting in the formation of mono-crystalline quasi 1D structures as depicted in figure 2.2c. While the diameter of the NW is determined by the dimensions of the gold catalyst, the

length can be controlled mainly by the growth duration, temperature and germane partial pressure in the chamber [52].

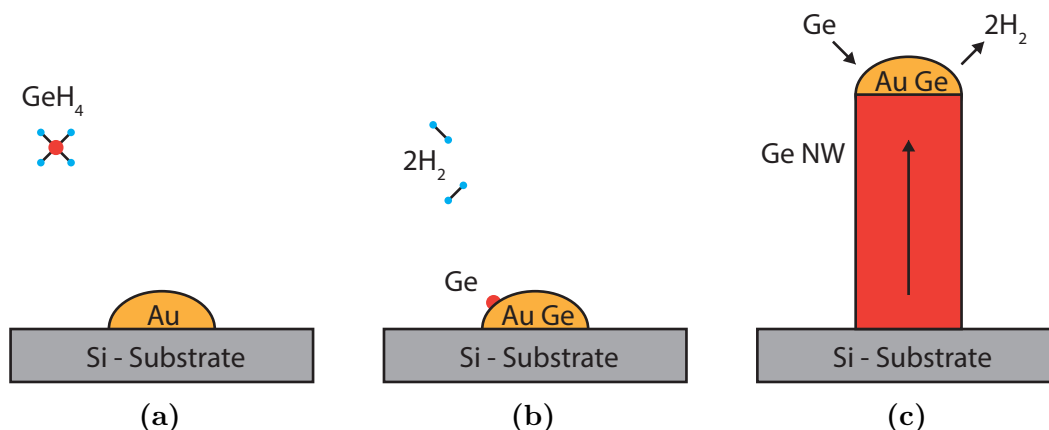


Figure 2.2: VLS growth mechanism for the synthesis of Ge NWs: (a) Au is deposited as a catalyst and annealed to form small droplets. Germane (GeH_4) is used as a precursor gas. (b) Germane decomposes at the Au surfaces forming an Au-Ge alloy leaving H_2 in the growth chamber. (c) Supersaturation of the droplet results in nucleation and directional growth of the Ge NW.

2.2 Germanium

Germanium (Ge) was first described by Clemens Winkler in 1886 [53] and named after his home country Germany. It is a group IV element with the atomic number 32 and a relative atomic mass of 72.61 [54]. As a typical elementary semiconductor, Ge crystallizes in the diamond structure exhibiting a lattice constant a of 6.659 Å at room temperature [54]. As depicted in figure 2.3a, the diamond lattice structure is consisting of two interpenetrating face-centered cubic (fcc) lattices shifted by one quarter of the lattice constant in all three dimensions. Each Ge atom forms a tetrahedron with its four surrounding neighbor atoms, which equals the number of valence electrons.

Ge is an indirect semiconductor with a band gap of $E_g = 0.66$ eV at room temperature, which is relatively small compared to silicon (Si) with 1.11 eV [54]. The direct band gap at the Γ -point is only 0.14 eV larger with $E_{\Gamma 1} = 0.8$ eV, as figure 2.3b illustrates. Thus, Ge exhibits a significantly higher absorption coefficient for incident photons than Si [55] making it suitable for many optical devices. Simulations have shown that because of this small energy difference strained Ge even becomes a direct

semiconductor [56], which opens the way to light emitting diodes (LED) or even lasers [22]. The next conduction band valley at the Δ -point has again only a slightly higher energy, which causes nonlinear electron transport phenomena like the negative differential resistance (NDR) [57]. This effect could be of great interest for future applications and will be further discussed in section 2.3.6. Moreover, compared to Si, Ge exhibits significantly higher carrier mobilities of $\mu_n = 3800 \text{ cm}^2/\text{Vs}$ and $\mu_p = 1820 \text{ cm}^2/\text{Vs}$ [54]. For holes, this is even the highest mobility of all known semiconductors [58], which is a great advantage for CMOS circuits.

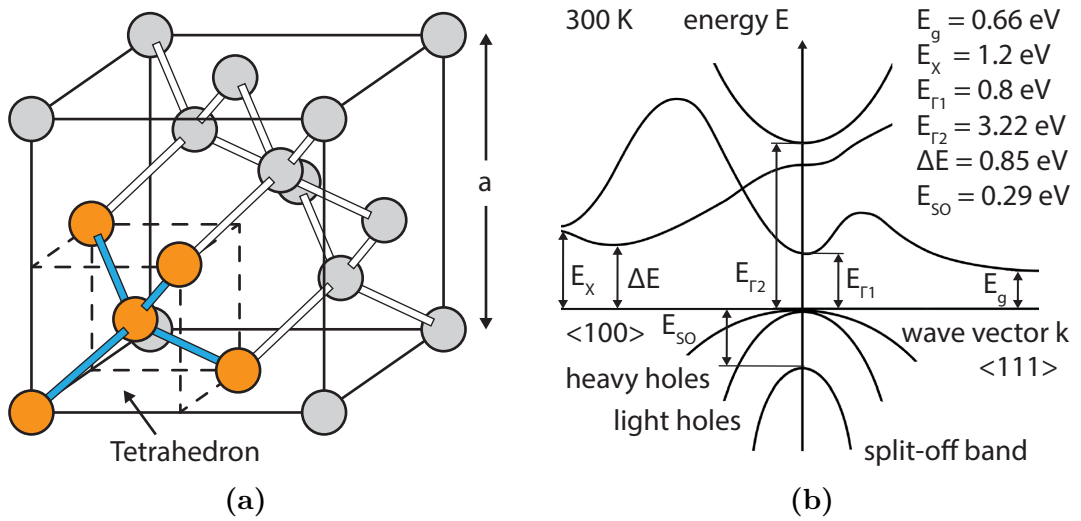


Figure 2.3: (a) The diamond lattice structure of Ge consisting out of two interpenetrating fcc lattices. Each atom has four surrounding neighbor atoms, which are arranged in a tetrahedral shape. Image adapted from [59]. (b) Energy band diagram of Ge at 300 K. Ge exhibits the indirect band gap at the L-point minimum with a band gap energy of $E_g = 0.66 \text{ eV}$. The direct band gap is located at the Γ -point and only 0.14 eV larger. After [60].

Despite these and numerous further advantages, Ge has been playing only a minor role in transistor technology during the past decades. Besides several other reasons like the higher fabrication costs, this can be mainly attributed to the fact that Si naturally produces a high quality oxide which is a very good insulator and stable at high temperatures and ambient conditions. In contrast, the oxide of Ge is unstable, soluble in water and can exhibit very high surface state densities up to 10^{15} cm^{-2} [61], which serve as recombination centers. Nevertheless, high- κ dielectrics have already shown the formation of high quality interfaces to Ge [62], making it a promising candidate for future transistor technologies again [60, 62].

2.3 Electronic Properties of Semiconductors

The scope of this section is to review basic semiconductor physics with special attention to Ge. Unless otherwise specified, the source of this chapter is the textbook «*The Physics of Semiconductors*» from M. Grundmann [63], where also further details and derivations can be found.

2.3.1 Band Structure

The electronic properties of solids are mainly determined by their crystal lattice (e.g. diamond lattice with $a = 6.659 \text{ \AA}$ for Ge as stated in section 2.2). By solving the Schrödinger equation with the help of Bloch's theorem for distinct crystals, their band structure ($E - k$ relation) can be obtained. Due to the short inter-atomic distances, broad continuous energy bands are formed, which determine the allowed states for electrons. Between those bands also energy regions may occur with no allowed states at all. If the Fermi energy happens to be in such a range, the material is either a semiconductor or insulator depending on the distance to the neighboring bands, which are called valence and conduction band. They are of particular interest, since they are the primary source of charge carrier transport. If the valence band maximum occurs at the same momentum as the conduction band minimum, the semiconductor is called direct (e.g. GaAs), otherwise indirect (e.g. Si, Ge). The gap between those bands is called the band gap.

The band structure defines how electrons move in this specific material, i.e. how much energy they exhibit at a certain momentum. If this dispersion relation is parabolic as in free space but with different curvature, it can be described using the same formalism by just replacing the mass of the electron with its effective mass. For the conduction band this gives

$$E(k) = E_C + \frac{\hbar^2 k^2}{2m^*} \quad (2.1)$$

where E_C is the conduction band minimum, $\hbar = h/(2\pi)$ is the reduced Planck constant and m^* is the effective mass, which is a characteristic of the respective semiconductor. This so-called effective mass approximation is valid for most common semiconductors near the band gap. A similar relation can be written for holes in the valence band, where typically two different effective masses exist for heavy and light holes (compare figure 2.3b).

2.3.2 Carrier Concentration

The carrier concentration describes the filling of the conduction and valence band and is therefore a crucial quantity for determining the carrier transport properties. To calculate this value, the density of states $D(E)$ has to be known, which describes the number of energy states per energy interval. Assuming parabolic band edges (i.e. the effective mass approximation holds) it is given by

$$D(E) = \left(\frac{2m^*}{\hbar^2}\right)^{\frac{3}{2}} \frac{(E - E_C)^{\frac{1}{2}}}{2\pi^2} \quad (2.2)$$

which is graphically indicated for the conduction and valence band in figure 2.4a. This assumption is valid for ideal 3D systems (compare figure 2.1) and a good approximation for most semiconductors. In figure 2.4b, the Fermi distribution function $f(E)$ is plotted, which describes the general filling of energy states as a function of temperature. It is given by

$$f(E) = \frac{1}{1 + \exp\left(\frac{E - E_F}{k_B T}\right)} \quad (2.3)$$

where k_B is the Boltzmann constant and T is the temperature. The Fermi level E_F is defined as the energy where at 0 K all energy states below are filled and above remain empty. In order to obtain the carrier concentration n in the conduction band, the

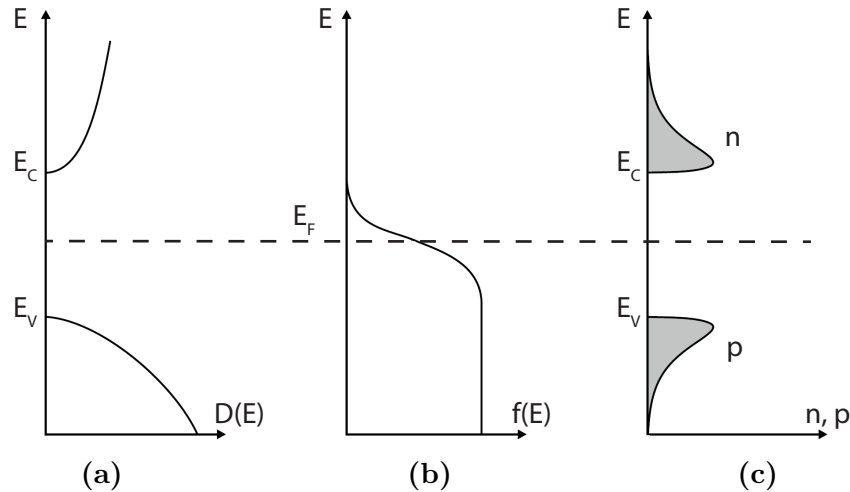


Figure 2.4: (a) Density of states, (b) Fermi distribution and (c) carrier concentration for an intrinsic semiconductor in thermal equilibrium at finite temperature. Image adapted from [63].

integral of $D(E)$ and $f(E)$ is calculated for the desired energy range as illustrated in figure 2.4c:

$$n = \int_{E_C}^{\infty} D(E)f(E)dE. \quad (2.4)$$

Only a small amount of electrons is promoted to the conduction band depending highly on band gap and temperature, which is why intrinsic semiconductors behave very similar to insulators. By introducing the Boltzmann distribution instead of the Fermi distribution, which is a good approximation for non-degenerated semiconductor ($E - E_F \gg k_B T$), a simple analytical solution of this integral can be found:

$$n = N_C \exp\left(\frac{E_F - E_C}{k_B T}\right) \quad (2.5)$$

where N_C is the effective density of states in the conduction band. Analogously, the hole concentration in the valence band calculates to

$$p = N_V \exp\left(-\frac{E_F - E_V}{k_B T}\right) \quad (2.6)$$

where N_V is the effective density of states in the valence band. It holds that

$$np = N_C N_V \exp\left(-\frac{E_g}{k_B T}\right) \quad (2.7)$$

is independent of the Fermi level, which is called the mass-action law. E_g denotes the band gap energy and is therefore given by $E_C - E_V$. In intrinsic semiconductors at thermal equilibrium n equals p , because for every generated electron in the conduction band there is a corresponding hole in the valence band. This value

$$n_i = n = p = \sqrt{N_C N_V} \exp\left(-\frac{E_g}{2k_B T}\right) \quad (2.8)$$

is another important characteristic of a semiconductor and is called the intrinsic carrier density. For Ge, n_i equals $2.33 \cdot 10^{13} \text{ cm}^{-3}$ at 300 K [54]. As can be seen in (2.8), n_i is exponentially dependent on the temperature which is the main reason why the temperature range of semiconductor devices is limited by their band gap. The intrinsic Fermi level calculates to

$$E_{Fi} = \frac{E_V + E_C}{2} + \frac{k_B T}{2} \ln\left(\frac{N_V}{N_C}\right) \quad (2.9)$$

which is for most semiconductors close to the middle of the band gap.

2.3 Electronic Properties of Semiconductors

The carrier density can be controlled by adding a defined number and kind of impurity atoms, which is called doping. For example, a group V atom that substitutes a Ge atom in the crystal lattice has an additional electron, which is only weakly bonded. This results in a shift of the Fermi level to higher energies. Similar, doping with a group III element produces an additional hole and lowers the Fermi energy. More precisely and under the approximation that all dopant atoms are ionized

$$E_F = E_C + k_B T \ln \left(\frac{N_D}{N_C} \right) \quad (2.10)$$

for group V (n-type) doping and

$$E_F = E_V - k_B T \ln \left(\frac{N_A}{N_V} \right) \quad (2.11)$$

for group III (p-type) doping with N_D and N_A being the doping concentrations of donors and acceptors respectively. The resistivity of semiconductors can thus be tuned in a wide range by introducing impurity atoms as depicted for Ge in figure 2.5. Due to the lower mobility of holes, ρ tends to be higher for p-type doping at equal concentrations.

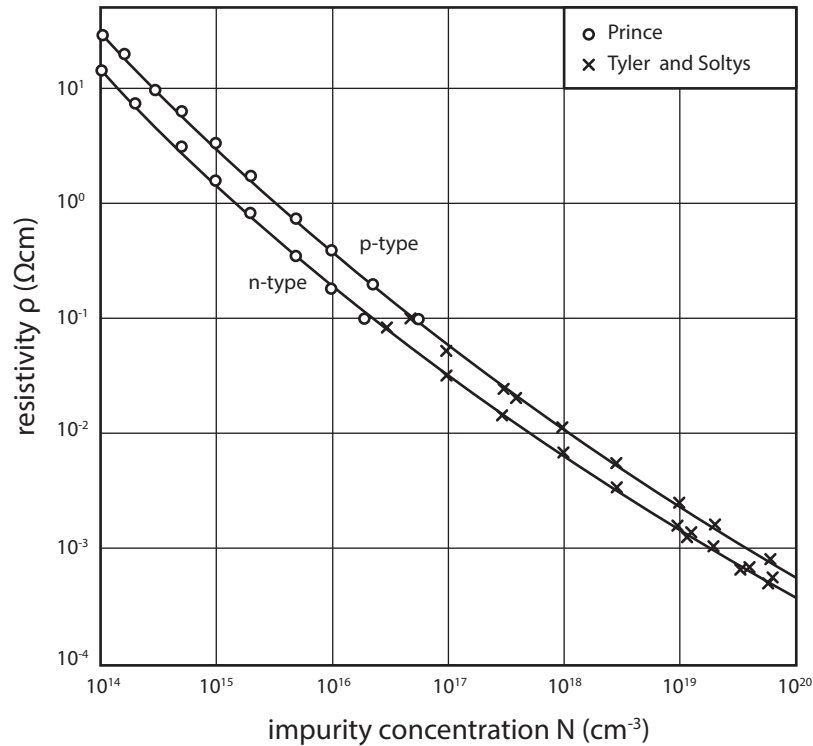


Figure 2.5: Resistivity of Ge as a function of impurity concentration for n- and p-type doping at 300 K. Image adapted from [64] with data from [65] and [66].

2.3.3 Charge Carrier Transport

Practically all important semiconductor devices are based on the transport of charge carriers, including transistors, diodes, photodetectors and lasers. The motion of carriers in semiconductors is driven by a gradient in the Fermi level. Two different mechanisms can be distinguished:

- drift, as a consequence of an external electric field \mathcal{E}
- diffusion, as a consequence of a concentration gradient ∇n or ∇p

For an electron moving in vacuum (i.e. ballistic transport) the influence of an electric field can be described by

$$\mathbf{F} = m^* \frac{d\mathbf{v}}{dt} = -e\mathcal{E} \quad (2.12)$$

where \mathbf{F} is the force acting on the electron, m^* the effective mass, \mathbf{v} the velocity, e the elementary charge and \mathcal{E} the electric field. In real semiconductors however, impurities, phonons and defects (including also surface) will cause scattering, which limits the transport similar to a frictional force. Two regimes can be distinguished. At low temperatures, impurity scattering is dominant while at higher temperatures phonon scattering (i.e. the scattering on lattice vibrations) limits the transport. For field effect transistors (FET) under normal operation, the surface roughness scattering mechanism is limiting, because the current is mainly flowing at the interface to the gate dielectric. The probability of a scattering event is proportional to the carrier velocity and can be introduced via the additional term $\dot{\mathbf{v}} = -\mathbf{v}/\tau$ with τ the average relaxation time of a scattering event. The maximum velocity that can be reached in a static electric field is given by the steady-state velocity ($\dot{\mathbf{v}} = 0$)

$$\mathbf{v} = -\frac{e\tau}{m^*}\mathcal{E} = -\mu\mathcal{E} \quad (2.13)$$

with the mobility

$$\mu = \frac{e\tau}{m^*}. \quad (2.14)$$

The current density \mathbf{j} then calculates to

$$\mathbf{j} = -en\mathbf{v} = \frac{ne^2\tau}{m^*}\mathcal{E} = \sigma\mathcal{E} \quad (2.15)$$

which satisfies Ohm's law. Thereby, n is the carrier density of electrons and σ is the specific conductivity

$$\sigma = \frac{ne^2\tau}{m^*} = ne\mu \quad (2.16)$$

which is the inverse of the resistivity. In general, both electrons and holes are present, yielding

$$\sigma = e(n\mu_n + p\mu_p) \quad (2.17)$$

where μ_n and μ_p are the mobilities of electrons and holes, respectively. The conductivity of semiconductors is therefore on the one hand dependent on the carrier densities and on the other hand determined by the mobilities of both charge carrier species. The mobility is determined by the effective mass and scattering frequency, while the carrier densities are dependent on doping, temperature and band gap of the material.

The diffusion of carriers is described by Fick's law which microscopically corresponds to a random walk of charge carriers. It is driven by a gradient in the concentrations of n or p and results in electron and hole current from higher to lower concentrations according to

$$\mathbf{j}_n = eD_n\nabla n \quad (2.18)$$

$$\mathbf{j}_p = -eD_p\nabla p \quad (2.19)$$

with the diffusion coefficients D_n and D_p , given by

$$D_n = \mu_n \frac{k_B T}{e} \quad (2.20)$$

$$D_p = \mu_p \frac{k_B T}{e} \quad (2.21)$$

according to the Einstein relation. Thus in the presence of an electric field the total electron and hole currents are

$$\mathbf{j}_n = e\mu_n n\mathcal{E} + \mu_n k_B T \nabla n \quad (2.22)$$

$$\mathbf{j}_p = e\mu_p p\mathcal{E} - \mu_p k_B T \nabla p \quad (2.23)$$

which holds for homogeneous band structures, i.e. the band gap is constant over the whole semiconductor.

2.3.4 Recombination in Semiconductors

The description in section 2.3.2 is valid for semiconductors in equilibrium. However, various mechanisms, such as carrier injection through the contacts or the absorption of light, can generate excess minority charges in the conduction and valence band. After turning off this excitation, the relaxation of charge carriers into energetically lower states brings the semiconductor back into its equilibrium state. This process is called recombination. Various mechanisms are distinguished, including (i) band-to-band, (ii) Auger and (iii) Shockley-Read-Hall (SRH) recombination.

(i) Band-to-band recombination is the direct relaxation of an electron in the conduction band to an empty state (hole) in the valence band. The released energy is converted into a photon with the corresponding wavelength $\lambda \leq hc/E_g$. In indirect semiconductors this process is much less probable, because an additional phonon is needed to account for the change in momentum of the electron. In Ge however, there is also the possibility for direct transition at the Γ -point, because of the low energy differences between the direct and indirect conduction band valleys. By increasing the electron population in the Γ -valley, which can be accomplished for example by applying tensile strain, direct recombination with high efficiency can be achieved [67].

(ii) Auger recombination is a similar process, but instead of emitting a photon, the released energy is transferred to an additional electron or hole. Thus, Auger recombination is a three particle process and becomes likely only for high carrier densities, either through doping or by generating a high amount of excess carriers.

(iii) However, in Ge NWs the dominant recombination process is the so-called SRH mechanism. Impurities and surface defects result in energy levels in-between the band gap, which serve as trapping centers for electrons and holes. Figure 2.6 shows

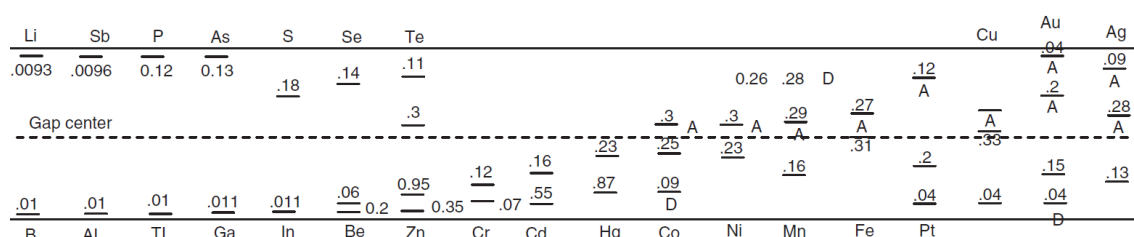


Figure 2.6: Energetic position of common impurities in the band gap of Ge in eV. Levels below the gap center are measured from the top of the valence band and act as acceptors unless indicated by D for donor. Levels above the gap center are measured from the bottom of the conduction band and act as donors unless indicated by A for acceptor. Image adopted from [68].

the energy levels of different impurities in Ge. In NWs, due to their high surface to volume ratio, surface defects, which vary highly in energy and lifetime, are the main source of traps within the band gap. Transitions between conduction and valence band may occur by using these trap levels as intermediate steps. The closer they are to mid gap energy, the more efficient they act as recombination centers [63]. Figure 2.7 illustrates the possible band-to-impurity transfer processes at an impurity with one energy level:

- (a) Electron capture: An electron from the conduction band is captured by an unoccupied trap.
- (b) Electron emission: An electron from an occupied trap moves to the conduction band.
- (c) Hole capture: An electron from an occupied trap moves to the valence band.
- (d) Hole emission: An electron from the valence band is captured by an unoccupied trap.

Overall, in the case of trap assisted recombination, the electron may move from conduction band over a trap level (a) to the valence band (c). Because the trap states can absorb differences in momentum between the carriers, this process is of particular importance in indirect semiconductors, where a direct transition requires an additional phonon. In real semiconductors, all recombination processes take place simultaneously, whereat the mechanism with the shortest carrier lifetime is dominating. Typical minority carrier lifetimes in intrinsic Ge are in the range of 10^{-3} s [69].

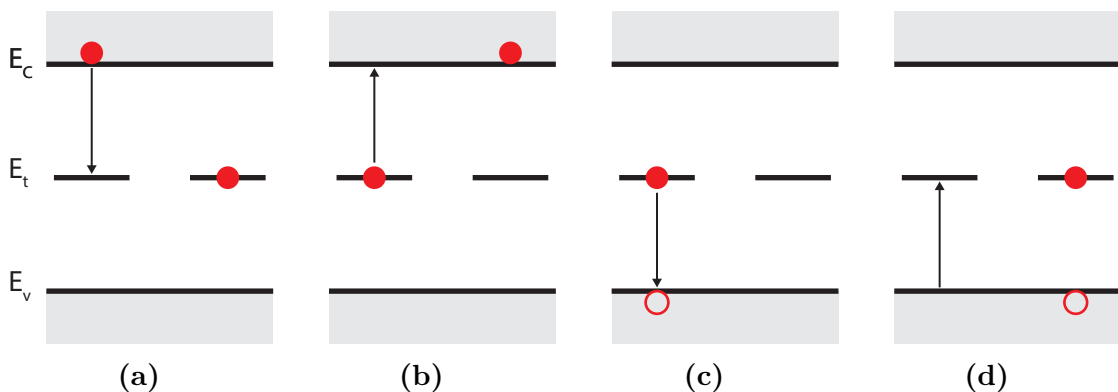


Figure 2.7: Schematic of possible band-to-impurity transfer processes at an impurity with one level. (a) Electron capture from conduction band. (b) Electron emission into conduction band. (c) Hole capture from valence band. (d) Hole emission into valence band.

2.3.5 Light Absorption in Semiconductors

When light is incident on a semiconductor it can either be reflected, transmitted or absorbed. In the case of absorption, a photon excites an electron from the valence band into the conduction band, which causes an increase in the number of minority carriers and therefore in the conductivity according to (2.17). This can either happen directly or via a trap level similar to the SRH-recombination described in the previous section.

For the direct transition, the photon energy has to exceed the band gap energy ($\hbar\omega \geq E_g$) and the momentum has to be preserved. Since photons carry very little momentum, such transitions appear almost vertical in the $E(k)$ diagram as can be seen in figure 2.8. Thus, in indirect semiconductors an additional phonon is required for light absorption, which results in a very low efficiency compared to direct semiconductors. Due to the small energy differences in the direct and indirect band gap, Ge exhibits both absorption mechanisms. For an indirect transition, the photon can also be of less energy than the band gap and the momentum can be absorbed by the trap. This mechanism is strongly dependent on the trap density of the semiconductor.

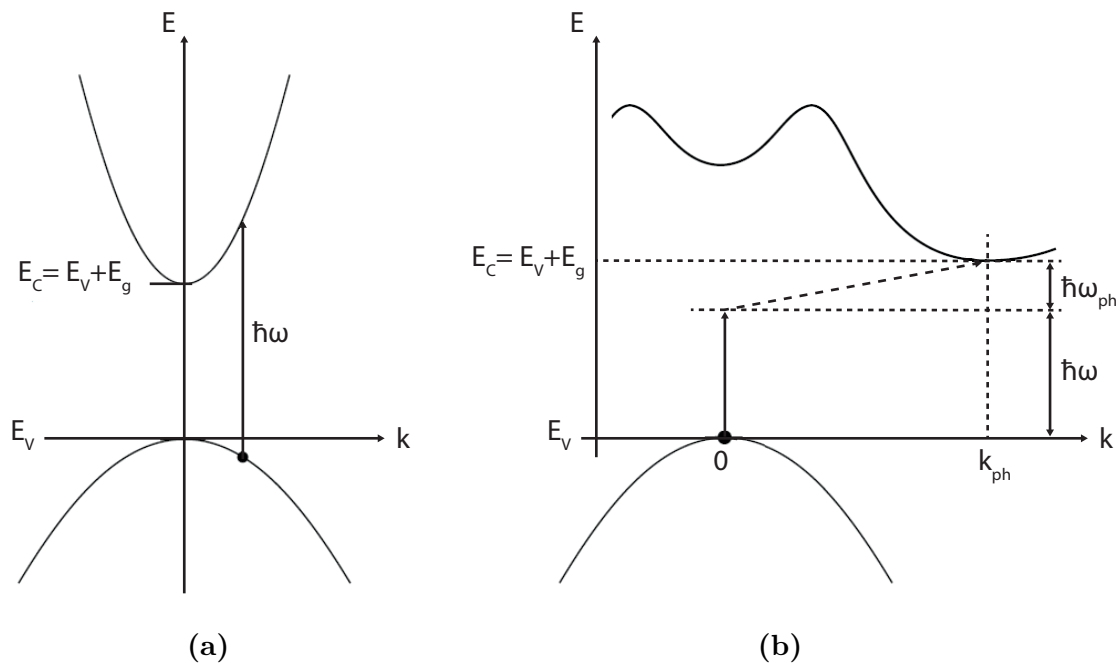


Figure 2.8: (a) Direct and (b) indirect optical transitions between valence and conduction band with photon energy $\hbar\omega$. The indirect transition involves a phonon with energy $\hbar\omega_{ph}$ and wavevector k_{ph} . After [63].

In general, the absorption rate of a material is proportional to its thickness and the light intensity of incident light. This leads to an exponential decay along the depth of the material according to the Beer–Lambert law

$$I(x) = I_0 e^{-\alpha x} \quad (2.24)$$

where I_0 is the initial light intensity at the surface ($x = 0$), $I(x)$ is the intensity of light after traveling the distance x through the material and α is the absorption coefficient at a certain wavelength. As depicted in 2.9, the absorption coefficient α is strongly dependent on the wavelength (i.e. energy) of the incident photons. The indirect band gap of 0.66 eV defines the first absorption edge of Ge. For photons with less energy, Ge is transparent. Photons with slightly higher energies are absorbed with low efficiency due to the requirement of an additional phonon. At the direct band gap of 0.8 eV a second absorption edge appears, above which the high efficient direct absorption is enabled. The shift of the absorption edges for 77 K is a consequence of the temperature dependence of the band gap [55].

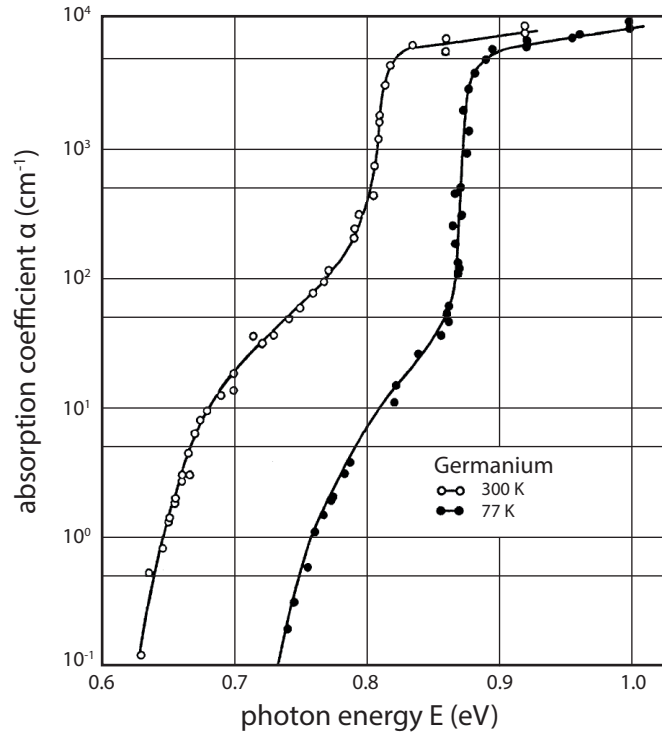


Figure 2.9: Optical absorption coefficient of Ge as a function of photon energy at 77 K and 300 K. The two absorption edges for the direct and indirect transition can be clearly seen at the according band gap energies of 0.66 eV and 0.8 eV at 300 K (compare figure 2.3b). For lower temperatures, the band gap energies increase which results in a shift of the absorption edges. After [55].

2.3.6 Negative Differential Resistance

Negative differential resistance (NDR) is a nonlinear transport phenomenon, where the current voltage relation becomes non-monotonic, and therefore at least one region in the $I - V$ curve arises which has negative slope. When calculating the differential resistance

$$r_{diff} = \frac{dV}{dI} \quad (2.25)$$

with V the voltage and I the current, it becomes negative in that region. NDR can originate from several processes, including resonant tunneling [70], self heating [71], charge trapping [72] and the transferred electron effect [57, 73], which is well known for GaAs as the Gunn effect [74].

In Ge, due to its band configuration, the transferred electron effect is of special importance. When the electric field is high enough, which is the case at a certain bias voltage, electrons gain enough energy to scatter efficiently from the L -point minimum to the X -point minimum as schematically shown in figure 2.10. There they exhibit a lower mobility and thus according to (2.17) also a lower conductivity. Since this effect requires the transport to be in the conduction band, it can only be observed in n-type Ge.

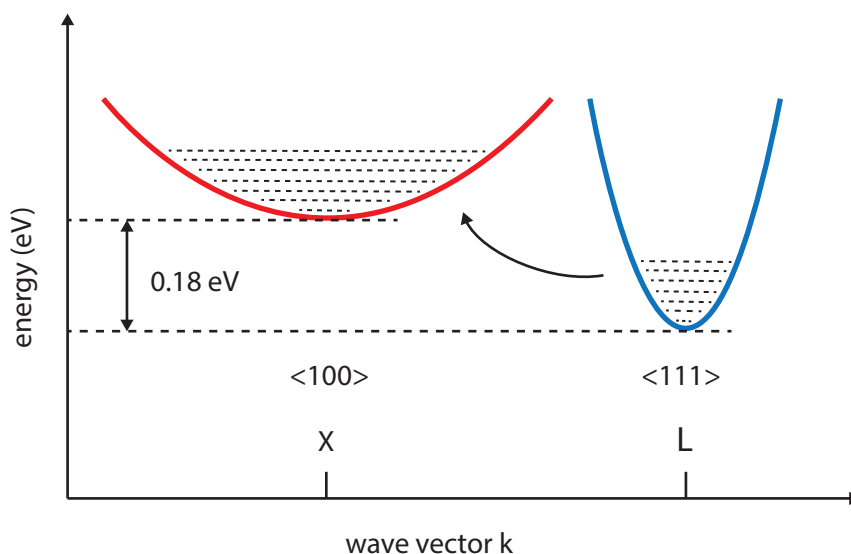


Figure 2.10: Schematic illustration of the transferred electron effect in Ge. Electrons from the L -point minimum are scattered to the X -point minimum, which has higher energy and lower mobility. After [73].

2.4 Surface Trapping in Germanium

During the early years of semiconductor electronics, Ge has been the workhorse for the development of diodes and transistors and was therefore studied extensively. Due to the upcoming field effect devices, especially the surface properties were of great importance and have been addressed by several researchers already in the 1950s [61, 75, 76]. The low quality of Ge oxide resulting in insufficient passivation of the surface led then to the downturn of Ge and the success of Si. While this behavior is a show-stopper for Ge based MOSFETs it turns out to be very useful for the design of photodetectors as will be discussed in section 2.5.

As already stated in section 2.3.4, defects and impurities in the crystal lattice are creating energetic states located in the band gap region. Once a carrier spatially samples such a defect site, the probability for trapping is very high, which is one of the main reasons for the extremely high purity requirements for semiconductors. Defect densities below 10^{15} cm^{-3} are already accomplished in device-grade material, eliminating the influence of bulk defects for most applications. Surfaces however, are a different challenge in terms of the formation of trapping states. Every surface, by its nature, defines a break in the lattice symmetry leaving unterminated atoms behind, if not passivated properly. These so-called dangling bonds are energetically positioned in the band gap and act there as trapping centers for charge carriers as well as reactive sites for various adsorbates. Typical defect densities are in the range of 10^{12} to 10^{13} cm^{-2} , corresponding to roughly 0.1 to 1% of the surface atoms [77]. For Ge, Kingston [61] even found a defect density of 10^{15} cm^{-2} , which would equal one state per lattice site for monolayer adsorption. By reducing the surface to volume ratio, as it is naturally the case when reducing the dimensions in nanoscale devices, the surface effects even gain greater influence on the behavior. Thus, in Ge NWs the surface plays a critical role and special care must be taken when dealing with such devices.

2.4.1 Trapping Mechanism

Trapping is a similar mechanism as SRH recombination (section 2.3.4), but instead of recombining with charge carriers of the opposite band, the carriers are emitted back to their previous states after a certain period of time. In the simplified schematic of figure 2.7 this means in the case of an electron a transition from the conduction band into the trap (a) and vice versa (b). While remaining in the trap, the carrier is immobile and can not contribute to the transport anymore resulting also in

an unequal number of excess holes and electrons, which violates the equilibrium condition of (2.8). Traps can either be neutral when empty and negatively charged when full (electron trap) or neutral when full and positively charged when empty (hole trap). Like for every other energy state, the population of a trap f_t is given by the Fermi distribution:

$$f_t = \frac{1}{1 + \exp\left(\frac{E_t - E_F}{k_B T}\right)} \quad (2.26)$$

where E_t is the energy level of the trap. The capture rate for electrons r_c is proportional to the density of unoccupied traps $N_t(1 - f_t)$ and the electron concentration n , which gives

$$r_c = v_{th} \sigma_n n N_t (1 - f_t) \quad (2.27)$$

where v_{th} is the thermal velocity, σ_n is the capture cross section and N_t is the trap concentration. Filled traps emit the electrons again with the emission rate g_c according to

$$g_c = e_n N_t f_t \quad (2.28)$$

with e_n being the emission probability, which can be written as

$$e_n = v_{th} \sigma_n N_C \exp\left(\frac{E_t - E_C}{k_B T}\right) \quad (2.29)$$

where N_C is the effective density of states in the conduction band and E_C is the bottom edge of the conduction band. Capture and emission rates for holes can be derived in a similar way. A quantity arising from this formalism is the so-called carrier lifetime

$$\tau_{n,0} = \frac{1}{v_{th} \sigma_n N_t}. \quad (2.30)$$

It defines the average time it takes an excess minority carrier to be captured by a trap and has to be distinguished from the trap time constant or trap lifetime

$$\tau_{t,0} = \frac{1}{v_{th} \sigma_n n} \quad (2.31)$$

which is the mean time before a trap captures a carrier. This model is valid for traps located in the bulk or directly at the interface of a semiconductor.

2.4.2 Oxide Traps

Oxide traps, located far away from the interface, can not be reached directly, but only via quantum mechanical tunneling through the oxide. Heiman and Warfield [78] found that the time constant for an oxide trap at the distance x from the interface can be expressed as

$$\tau_t(x) = \tau_{t,0} e^{2\kappa_0 x} \quad (2.32)$$

with κ_0 being the decay constant associated with tunneling. Thus, oxide traps can exhibit very large time constants in comparison to interface or bulk traps.

From figure 2.11 it can be understood why oxide traps vary highly in lifetime and energy, which is one of the main differences to the well-defined traps in bulk. At equilibrium, it can be assumed that trap levels below the Fermi energy get filled and above remain empty. Figure 2.11a illustrates how this causes the dependency of trap filling from the electric field in the oxide. When assuming a single trap level in the oxide above the Fermi energy it will remain empty at the surface. However, when applying an electrical field, the bands of the oxide will be bent and trapping states far away from the surface will be pushed below the Fermi energy. Those states are getting filled via tunneling until a certain depth x_M , where tunneling becomes unlikely. When measuring the distribution of surface states, a high spread in energy occurs although only one trapping state energy exists. Real oxides typically exhibit more than one defect state energy making the distribution even broader. The second

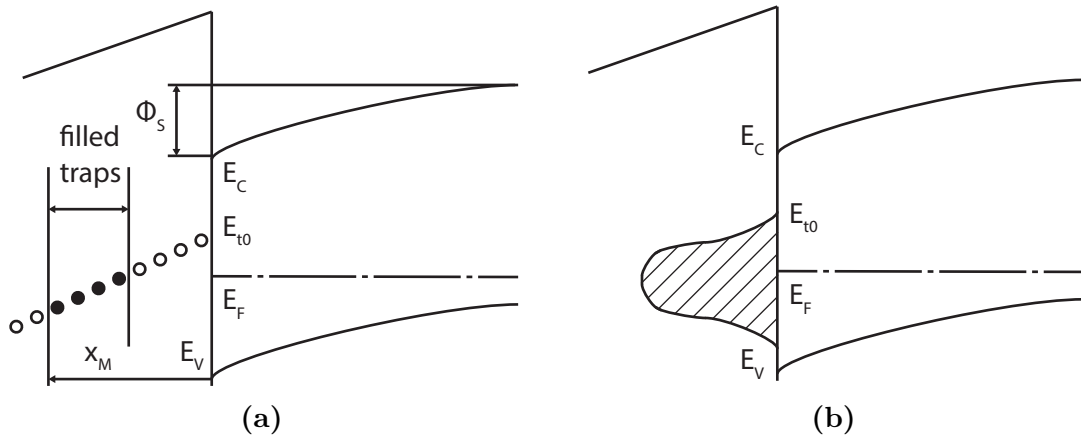


Figure 2.11: Energy band diagram of an oxide semiconductor interface with a single trap level at E_{t0} under applied field. (a) shows the filling of traps under the Fermi energy and up to a certain depth x_M in the oxide resulting in an effective measured energetically spread of trap levels as depicted in (b). Image adopted from [78].

effect arising in oxide traps is the variation of lifetimes, which occurs due to the different distances of the traps to the surface according to (2.32). Thus, under varying fields, the lifetimes and energies of the measured trap levels will change accordingly.

2.4.3 Germanium Surface

On ideally terminated Ge surfaces, one quarter of the valence electrons of the surface atoms exhibit broken bonds [79]. In reality, this number is reduced by adatoms and surface reconstruction minimizing the energy. Unlike Si, Ge does not have a high quality native oxide which naturally passivates dangling bonds on the semiconductor oxide interface, thus leaving a high number of defects behind [80, 81]. The surface properties of Ge are therefore mainly determined by the quality of the oxide on the interface.

When exposed to air, Ge forms a native oxide with ill-defined composition dependent on temperature and other growth-conditions [82]. The formation of 4 different oxides at the Ge surface can be observed as listed in table 2.1. Beside the well-known germanium dioxide (GeO_2) and germanium monoxide (GeO), two other oxide species exist, namely Ge_2O_3 and Ge_2O . The electrical properties of the interface is strongly dependent on the composition of those suboxides. Due to the higher quality of the GeO_2/Ge interface, the formation of germanium dioxide is desirable in terms of reducing surface trapping [83]. However, non of the oxides remains stable under ambient conditions, which results in a permanent change of composition when exposed to high temperatures or water. GeO_x will be used from now on to denote germanium oxide with undefined composition.

Table 2.1: *Composition of thermally grown germanium oxide on a Ge(100) surface under atomic oxygen exposure at different oxidation temperatures [84].*

T_{OX} ($^{\circ}\text{C}$)	GeO_2 (%)	GeO (%)	Ge_2O_3 (%)	Ge_2O (%)
RT	18.8	16.5	38.5	26.2
200	45.7	11.6	33.1	9.6
300	89.6	5.0	0.0	5.4
400	50.2	7.6	33.5	8.7

As already stated, there are different types of surface states in oxide semiconductor interfaces, which are commonly classified into slow and fast states [61]. While the

fast states are located directly at the interface, the slow states reside in the native oxide layer and can be reached only by quantum mechanical tunneling, as indicated in figure 2.12a. In 2.12b, the typical concentrations and lifetimes of the two types of surface states at the GeO_x/Ge interface are listed. The lifetime of slow traps is highly dependent on the distance from the surface and can reach up to several minutes. Traps residing directly on the surface are significantly faster and therefore primarily responsible for recombination processes [85, 86]. They are energetically located around 0.2 eV above the valence band maximum of Ge [61]. For slow states, Hanrath and Korgel [86] found a high and uneven spread of energy levels across the entire band gap. Surface traps in Ge are known to be acceptor like, meaning that they are negatively charged when full and neutral when empty [86].

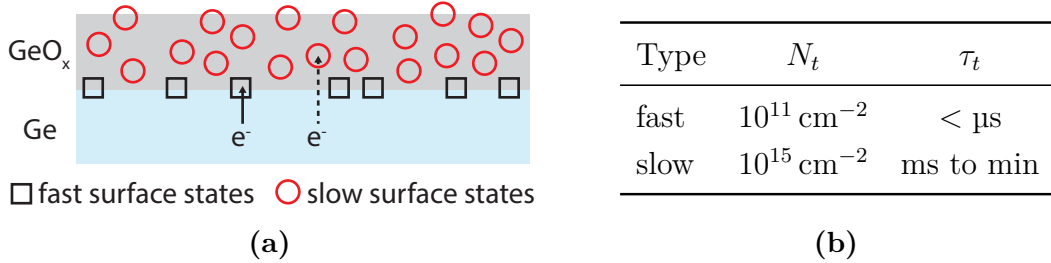


Figure 2.12: (a) Schematic of a GeO_x/Ge interface with both relatively fast surface states with typical lifetimes smaller than $1 \mu\text{s}$ and slow traps residing deeper in the oxide with lifetimes of up to several minutes. While the fast states have a moderate surface concentration of about 10^{11} cm^{-2} , the slow ones can exhibit concentrations of up to 10^{15} cm^{-2} as (b) indicates (Data taken from [61]).

2.4.4 Surface Charge Induced Band Bending

Since traps in the oxide are very slow, their impact on recombination is negligible. However, they have a significant influence on the transport in semiconductors due to the interaction of electrons or holes trapped in the oxide with charge carriers close to the surface of the material. In a simplified model, one can assume a constant surface trap level density D_t over the band gap region as schematically shown in figure 2.13a. D_t is connected to N_t and given in units of $\text{cm}^{-2} \text{ eV}^{-1}$. Since traps below the Fermi energy and above the valence band maximum are getting filled by electrons, the surface trap charge density Q_t calculates to

$$Q_t = -e \int_{E_V}^{E_F} D_t dE \quad (2.33)$$

2 Theory

with $e = 1.602 \cdot 10^{-19}$ C being the elementary charge and E_F and E_V being the Fermi energy and the valence band maximum at the surface, respectively. These charges result in an effective surface potential Φ_s according to Poisson's equation

$$\nabla^2 \Phi_s = \frac{Q_t}{\varepsilon_0 \varepsilon_{Ge}} \quad (2.34)$$

with ε_0 and ε_{Ge} being the vacuum and relative permittivity of Ge. As depicted in figure 2.13, this leads to an upward band bending to maintain charge neutrality in the semiconductor. The width w of the depletion layer in this planar approximation calculates to

$$w = \sqrt{\frac{2\varepsilon_0 \varepsilon_{Ge} \Phi_s}{e N_d}} \quad (2.35)$$

where N_d is the doping concentration [87]. For intrinsic or moderately n-type doped Ge, even p-type behavior is observed at the surface [88].

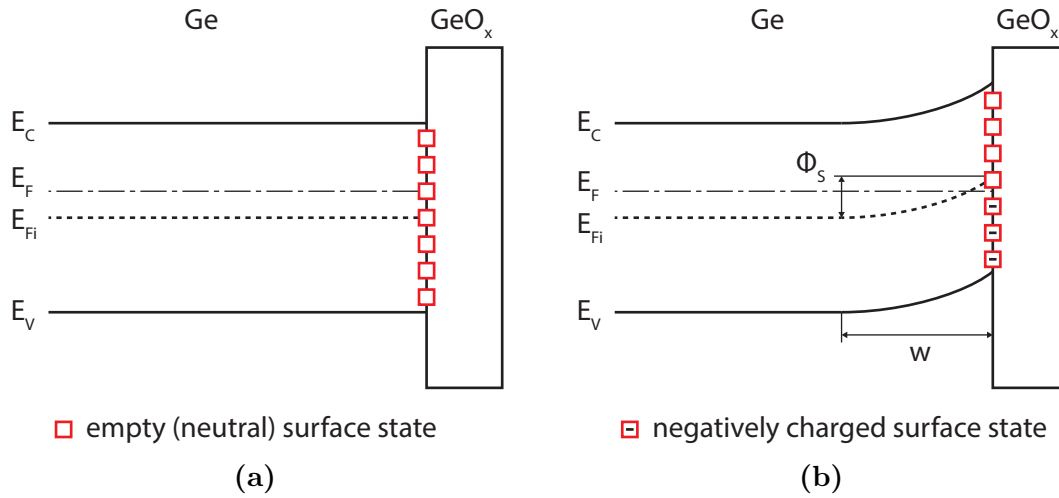


Figure 2.13: Slightly n-doped Ge with acceptor-like surface states (a) before and (b) after equilibrium is reached. States below the Fermi energy get filled by electrons resulting in a negatively charged surface, which causes the bands to bend upwards. A depletion layer with width w originates at the surface and even inversion may be observed.

In reality i.e. under ambient conditions, the surface trap density is not constant and additional charges originate at the surface due to the adsorption of various gases [89, 90]. However, the influence of such adsorbents can be eliminated by proper passivation. Furthermore, it is known that Ge has a strong Fermi level pinning up

to high doping concentrations. In Ge, the so-called charge neutrality level (CNL), where the Fermi level pins at equilibrium, is located 0.09 eV above the top of the valence band [91, 92]. However, due to the long lifetimes of traps in the presence of a native oxide layer, transient behavior of the electron transport can be observed which suggests a shift of the Fermi energy at the surface [86].

2.4.5 Trapping in Nanowires

Due to their quasi 1D geometry, NWs exhibit an extremely large surface to volume ratio making their properties strongly influenced by the surface. Hence, in order to understand electronic transport phenomena and optical effects in NWs, charges on the surface and in the oxide have to be considered carefully. In figure 2.14, the cross section and the band gap over a cut in this cross section are depicted. Negatively charged acceptor-like traps reside on the interface and in the oxide, which causes the surface potential Φ_s to be positive and the bands to bend upward. Assuming a relatively high doping of $N_d = 10^{18} \text{ cm}^{-3}$ and a surface potential of $\Phi_s = 0.1 \text{ eV}$, a depletion region originates at the surface with width $w = 13 \text{ nm}$ according to (2.35) when using a relative dielectric constant of $\epsilon_{Ge} = 16$. For thin NWs or lower doping concentrations, the radius of the neutral region r_d can even become 0, causing a shift of the energy band structure throughout the whole cross section of the wire, which causes the NW to behave p-type although not intentionally doped or even moderately n-type doped [88, 92]. This effect is called surface doping and has the potential of being used intentionally in future applications, where due to nanoscale dimensions of the channel, doping fluctuations become already critical [93].

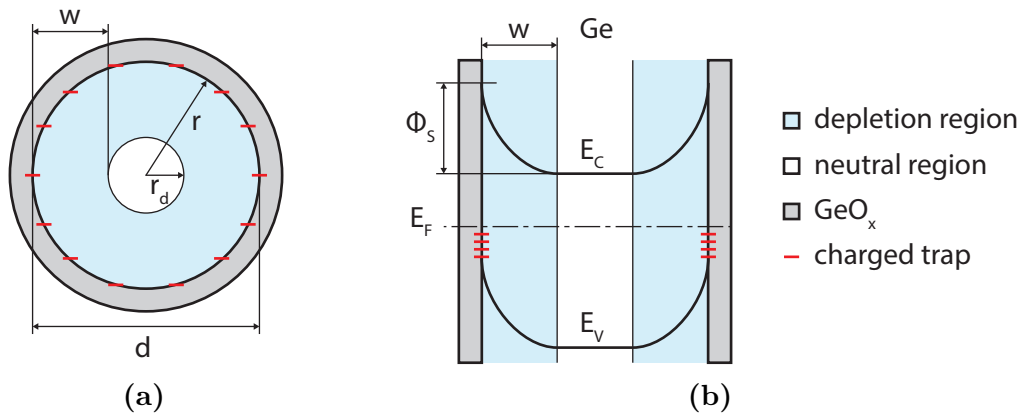


Figure 2.14: (a) Cross section and (b) band diagram of a n-doped Ge NW with diameter d and acceptor-like surface states. Band bending occurs with surface potential Φ_s and depletion width w .

2.5 Nanowire Photodetectors

Photodetectors are semiconductor devices, capable of detecting optical signals and converting them into electrical current. Two classes exist, namely bolometers, which detect light by sensing the temperature change of a material, and photon detectors, which are based on the quantum photoelectric effect. Here only the latter will be discussed, since it is the effect utilized in the course of this thesis. In general, the operation of a photodetector can be subdivided into three processes [59]:

1. Carrier generation by incident light
2. Carrier transport and/or multiplication
3. Carrier extraction to provide the output signal

Carrier generation in photon detectors is caused by the absorption of light as briefly described in section 2.3.5. Photons with energies exceeding the band gap can promote electrons to the conduction band and therefore cause an increase in free minority carriers. For multiplication and extraction different concepts exist, which reflects the variety of applications they can be used for and the different aspects of performance they aim to fulfill. The most common among them are photoconductors, photodiodes, avalanche photodiodes, phototransistors and charge coupled devices (CCD) [59].

While photodiodes can have fast response times, their maximum gain is fundamentally limited to one, making them not very sensitive to small irradiations. Photoconductors, on the other hand, are slower, but capable of achieving high gain, making them suitable for applications where high sensitivity is required such as single photon detection [16, 94, 95]. In particular NWs have shown to exhibit superior photoconductive properties due to their high surface to volume ratio and small dimensions [28, 96]. Their extraordinary sensitivity to light is recently attracting growing research interest for their potential use as optical interconnects, image sensors, optical switches and transceivers, to name but a few [28]. As material, Ge is especially interesting due to several reasons. Firstly, it has a small band gap making it capable of efficiently detecting light in the near infrared (NIR) regime, where optical telecommunication takes place [97]. Secondly, its high surface trap density and trapping lifetime is of great advantage for photodetection as will be discussed in section 2.5.2. And lastly, it is full compatible to current CMOS technology and can be even grown on Si in the form of dots [98], wires [99] or thin epitaxial layers [100]. Thus, Ge NWs are promising candidates for various photodetecting applications and their optical properties were studied intensively throughout the last years [101, 102].

2.5.1 Photoconducting Mechanism

Photoconductivity is a well-known property of semiconductors in which the electrical conductivity increases due to incident light. As depicted in figure 2.15 a photoconductor simply consists out of a piece of semiconductor with two ohmic contacts affixed to the opposite ends.

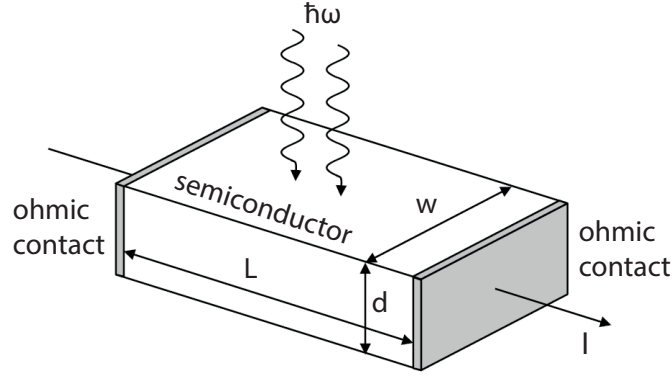


Figure 2.15: Schematic of a photoconductor, which consists of a semiconductor connected with two ohmic contacts [63].

When carriers are generated due to incident light, the conductivity increases. According to (2.17) this increase in conductivity can be expressed as

$$\Delta\sigma = e(\Delta n\mu_n + \Delta p\mu_p) \quad (2.36)$$

with Δn and Δp being the excess electron and hole densities, respectively. They calculate to

$$\Delta n, \Delta p = \eta \frac{P_{opt}}{h\nu} \frac{1}{V} \tau_{n,p} \quad (2.37)$$

where η is the quantum efficiency, i.e. the average number of carriers generated per absorbed photon, P_{opt} is the absorbed optical power, $h\nu$ is the photon energy, $V = wdL$ is the volume and $\tau_{n,p}$ denotes carrier lifetimes for electrons and holes. The corresponding photocurrent between the electrodes can then be written as

$$I_{ph} = \Delta\sigma \mathcal{E} wd = e \left(\eta \frac{P_{opt}}{h\nu} \right) \left((\mu_n \tau_n + \mu_p \tau_p) \frac{\mathcal{E}}{L} \right) \quad (2.38)$$

where $\mathcal{E} = V/L$ is the electrical field and V the voltage along the photoconductor.

With the primary photocurrent defined as

$$I_p = e \left(\eta \frac{P_{opt}}{h\nu} \right) \quad (2.39)$$

a photoconductive gain g is obtained

$$g = \frac{I_{ph}}{I_p} = (\mu_n \tau_n + \mu_p \tau_p) \frac{\mathcal{E}}{L} = \frac{\tau_n}{t_n} + \frac{\tau_p}{t_p} \quad (2.40)$$

where $t_{n,p} = L/v_{n,p}$ is the transit time through the photoconductor for electrons and holes, respectively. Besides gain, several other important parameters exist, which are summarized in table 2.2. They are used to compare performance of different types of photodetectors for different applications.

Table 2.2: *Figures of merit for photodetectors [16].*

Quantity	Symbol	Unit	Definition
Dark current	I_d	A	Current flowing in the absence of illumination.
Quantum Efficiency	η	%	In a photodiode, the ratio of photocurrent to photon fluence incident on the device.
Internal gain	g	-	In a photoconductor, the ratio of photocurrent (in electrons per second) to photon absorbed.
Responsivity	R	A W^{-1}	Photocurrent flowing in a detector divided by incident optical power.
Noise current	I_{noise}	$\text{A}/\sqrt{\text{Hz}}$	The random root mean square fluctuation in current when bandwidth is limited to 1 Hz.
Noise-equivalent power	NEP	$\text{W}/\sqrt{\text{Hz}}$	The minimum detectable power, that is, the optical power at which the signal to noise ratio (SNR) becomes 1, when bandwidth is limited to 1 Hz.
Normalized detectivity	D^*	$\text{cm}\sqrt{\text{Hz}}/\text{W}$ (Jones)	A measure of sensitivity that enables comparison even when detector area A and bandwidth B are different. $D^* = \sqrt{AB}/NEP$

2.5.2 Photoconductive Gain in Nanowires

The mechanisms leading to high gain in photoconducting NWs [28, 96, 101–105] and other low dimensional structures [94, 106–108] have been addressed recently by several researchers. In general, two effects can contribute to a rise of photoconductivity in nanomaterials: the photovoltaic (PV) and the photoconductive (PC) mechanism [108]. Usually they take place simultaneously, making it hard to distinguish the individual contributions.

The photoconductive effect arises from the basic working principle of a photoconductor, as described already in the previous section. If the lifetime of a carrier is longer than its transit time through the channel, it is able to make several transits before it will recombine with a carrier of opposite type. For every generated electron-hole pair, multiple charge carriers are extracted at the contacts resulting in photoconductive gain. This is mathematically expressed in (2.40) which comes down to the relation: $g = \tau/t$. Thus, to achieve high gain, both high carrier lifetime and low transit time have to be accomplished. Ge NWs are optimally suited for both, as will be argued in the following paragraphs.

The carrier transit time is given by $t = L/(\mu\mathcal{E})$. Thus, it can be reduced by shortening the channel length or increasing carrier mobility and electrical field along the wire. Ge exhibits the largest hole mobility of all known semiconductors and by growing high quality, defect free single crystal NWs, scattering, and thus transit time, can be further minimized [109]. The channel length can be efficiently reduced by exploiting a thermal induced exchange reaction between Al and Ge as was demonstrated by Kral et al. [25]. By increasing the voltage between the two contacts and therefore the electrical field along the NW, the photocurrent can be further maximized.

Because of the large surface trap density of Ge (section 2.4.3) combined with the high surface to volume ratio of NWs, an extremely high trap to volume ratio can be achieved. Photogenerated electrons may subsequently be trapped by these surface states with high carrier lifetimes and can therefore not recombine with holes in the valence band [94]. Thus, the carrier lifetimes of both electrons and holes are drastically increased, which is usually counterintuitive in semiconductors exhibiting high trap densities. Because electrons are trapped, they can not contribute to the carrier transport, however holes can flow through the channel resulting in an effective photocurrent. A second mechanism arising from the surface traps is related to band bending (section 2.4.4) and has been reported to prolong carrier lifetimes as well [28, 105]. Due to surface traps and the pinning of the Fermi level at the surface, band bending takes place, which is equivalent to high electric fields across the NW. Lee et al. [102] simulated the field distribution in Ge NWs associated with band

bending (figure 2.16) and concluded that for thinner NWs, when the depletion regions approach each other, this effect is even increased and higher fields occur. These fields provide spatial separation of holes in the valence band and electrons in the conduction band making recombination unlikely. This again, drastically increases carrier lifetime and therefore photoconductive gain.

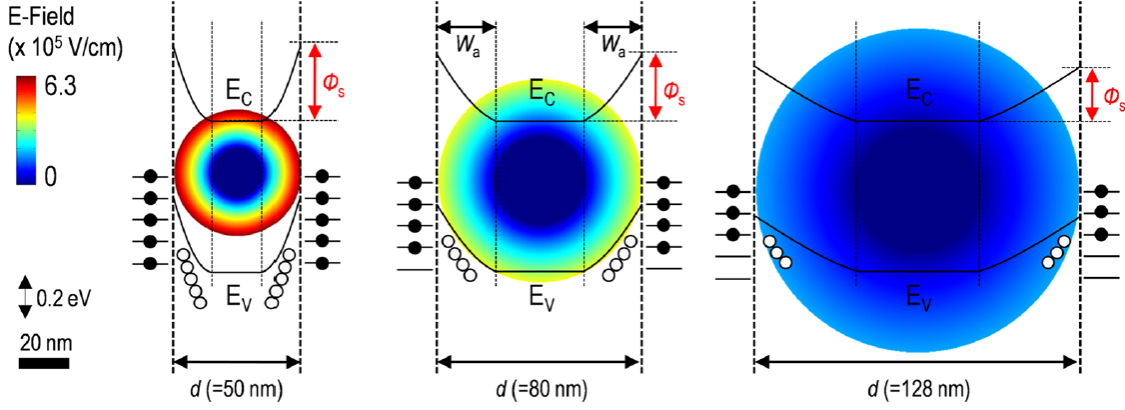


Figure 2.16: Simulated two-dimensional electrostatic field distribution in Ge NWs for different diameters. The resulting band diagrams for the cross section are overlaid in black, indicating steeper edges for thinner NWs [102].

The photocurrent caused by the PC effect can be expressed by substituting \mathcal{E} by V/L in (2.38):

$$I_{ph,PC} = e \left(\eta \frac{P_{opt}}{h\nu} \right) \left(\frac{V(\mu_n\tau_n + \mu_p\tau_p)}{L^2} \right) \quad (2.41)$$

The second mechanism is the photovoltaic effect. It has its origin in the efficient trapping of photogenerated carriers at the surface where they act as a local gate, which is why the PV effect is sometimes referred to as “photogating” [108]. This local gate can be mathematically described by a shift in threshold voltage from V_t to $V_t - \Delta V_{th}$ under optical illumination. The resulting photocurrent is then directly related to the transconductance g_m according to the relation

$$I_{ph,PV} = g_m \Delta V_{th} \propto \frac{k_B T}{e} \ln \left(1 + \frac{\eta e P_{opt}}{I_d h\nu} \right) \quad (2.42)$$

where I_d is the dark current for electrons [110, 111]. In contrast to the PC effect, the PV effect exhibits a non-linear dependence of the photocurrent to the optical power

of incident light, resulting in higher gain at lower illumination densities. For the PC mechanism this also occurs due to the fact that only a limited amount of traps is available, which causes the trapping probability to decrease under high illumination due to saturation. In literature, this behavior is often modeled by an inverse power law where the gain exponentially decreases with increasing light power, as

$$g \propto P_{opt}^{-k} \quad (2.43)$$

with the fitting parameter k usually in the range between 0.5 and 1 [112, 113]. Under low illumination, photoconductors can therefore exhibit an extremely high gain, as the comparison in table 2.3 shows. NWs, due to their large surface area, are especially suitable for photodetection.

Table 2.3: *Typical values of response time and gain of photodetectors [28].*

Detector	Response time (s)	Gain
Photoemissive		
Diode	10^{-11}	1
Photomultiplier	$10^{-10} - 10^{-8}$	10^6
Photovoltaic		
p-n junction	10^{-11}	1
p-i-n junction	$10^{-10} - 10^{-8}$	1
Schottky junction	10^{-11}	1
Phototransistor	$10^{-8} - 10^{-7}$	10^2
Avalanche photodiode	$10^{-10} - 10^{-6}$	$10^2 - 10^6$
Photoconducting		
Bulk	$10^{-8} - 10^{-3}$	$1 - 10^6$
Nanowire	$10^{-11} - 10^2$	$1 - 10^{10}$

2.5.3 Light Absorption in Nanowires

When dealing with light absorption in nanostructures featuring sizes well below optical wavelengths, additional effects must be taken into account. Resonances take place at certain wavelengths which are strongly dependent on size and shape of the nanomaterial. In NWs, leaky mode resonances (LMR) originate due to their elongated shape and small diameter [16, 115]. By solving Maxwell's equations for an

infinitely long dielectric cylinder of radius a with respective boundary conditions, it follows that the excitation of those leaky modes occurs exactly then when the following condition is fulfilled [114]:

$$\left(\frac{1}{\kappa^2} - \frac{1}{\gamma}\right)^2 \left(\frac{\beta m}{a}\right)^2 = k_0^2 \left(n^2 \frac{J'_m(\kappa a)}{\kappa J_m(\kappa a)} - n_0^2 \frac{H'_m(\gamma a)}{\gamma H_m(\gamma a)} \right) \times \left(\frac{J'_m(\kappa a)}{\kappa J_m(\kappa a)} - \frac{H'_m(\gamma a)}{\gamma H_m(\gamma a)} \right) \quad (2.44)$$

where κ and γ are transverse wave vectors inside and outside of the cylinder, n and n_0 are the refractive index inside and outside the NW, β and k_0 are the wave vectors along the cylindrical axis and in free space, J_m and H_m are the m^{th} order Bessel and Hankel functions of the first kind and the prime denotes differentiation with respect to related arguments. (2.44) can be split into conditions for TM modes and TE modes with the electric field parallel and normal to the NW axis, respectively. Depending

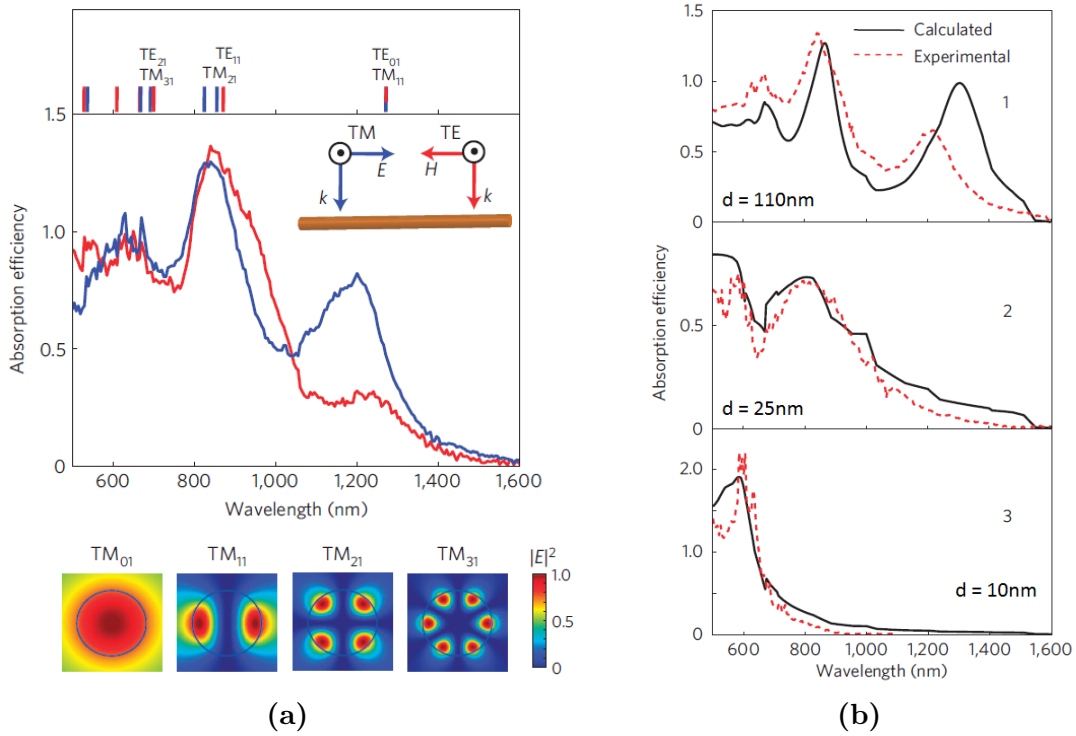


Figure 2.17: (a) Absorption efficiency spectra of a 110 nm radius Ge NW illuminated by linearly polarized TM (blue) or TE (red) light along with the wavelength of the leaky modes indicated on the top. (b) Experimental (red dotted) and calculated (black) absorption efficiency spectra for NW radii of (1) 110 nm, (2) 25 nm and (3) 10 nm showing the blue shift of the LMRs for smaller diameters [114].

on the diameter, a NW can support only a limited number of TM and TE leaky modes. As can be seen in 2.17a, absorption is increased at certain wavelengths, while it is decreased at others compared to bulk material, dependent on the resonances at that point. For smaller diameters, this effect is even more pronounced as shown in figure 2.17b causing very low absorption efficiency in the near infrared regime. Due to the different modes also polarization dependencies can be observed, which can be very high for small diameters [116]. Making use of this effect, it is possible to obtain high absorption efficiencies by tuning the NW geometry for a specific wavelength.

Experimental

This chapter deals with the experimental methods employed for the fabrication and characterization of Ge NW photodetectors. In the first section an overview of the device integration process is given, including the fabrication of the measurement module and the contact formation via electron beam lithography and Al sputtering. The setup for electrical measurements, which was used to characterize the trapping behavior, is described subsequently. Finally, the optical measurement setup, which was developed in the course of this thesis and the associated data evaluation steps are addressed in the last section of this chapter.

3.1 Device Integration

In order to carry out reliable electrical and optical measurements on individual NWs, they have to be contacted to the “outer world”. To do so, the VLS grown Ge NWs are transferred from the growth substrate to a specifically designed measurement module, which has to fulfill several requirements:

1. Formation of reliable electrical contacts on both sides of the NW.
2. Optical accessibility of the NW to carry out optical measurements.
3. Availability of a gate in order to control electrical transport.
4. Variation of device channel lengths in a wide range.

This is achieved by a sophisticated integration scheme explored by S. Kral [117], which allows for Al-Ge-Al heterostructure NWs with small channel lengths and abrupt high quality interfaces. The individual processing steps required are schematically shown in figure 3.1 and laid out in the following paragraphs. More details including processing parameters are given in appendix A.

(a) As substrate material, a highly p-type doped $\langle 100 \rangle$ -oriented Si wafer with 100 nm thermally grown SiO_2 on top is used. After cleaving a 15×15 mm piece from the wafer the substrate is cleaned in an ultrasonic process with acetone and isopropanol to remove any organic residues.

(b) In order to pattern the macroscopic contacts, common photolithography using image reversal resist and UV light is utilized. In the first step, back-gate contacts are formed via etching the SiO_2 with buffered hydrofluoric acid (BHF) on distinct areas. In a second lithography step, the contacts for drain and source are patterned and image reversal bake is applied to achieve edges with retrograde profiles.

(c) Subsequently, Ti/Au contacts are deposited via magnetron sputtering and a following lift-off process. The cross section in figure 3.1c shows the basic measurement module featuring macroscopic contacts, which are either isolated or connected to the underlying high doped Si substrate, which later acts as a back gate. The isolated contacts are used to connect individual NWs to the outer measurement setup, which is shown in the following steps. On each measurement module, 114 of those contacts exist, allowing the integration of 57 individual NWs. They are organized in 19 hexagonal structures with 6 contacts each (compare figure 3.2b).

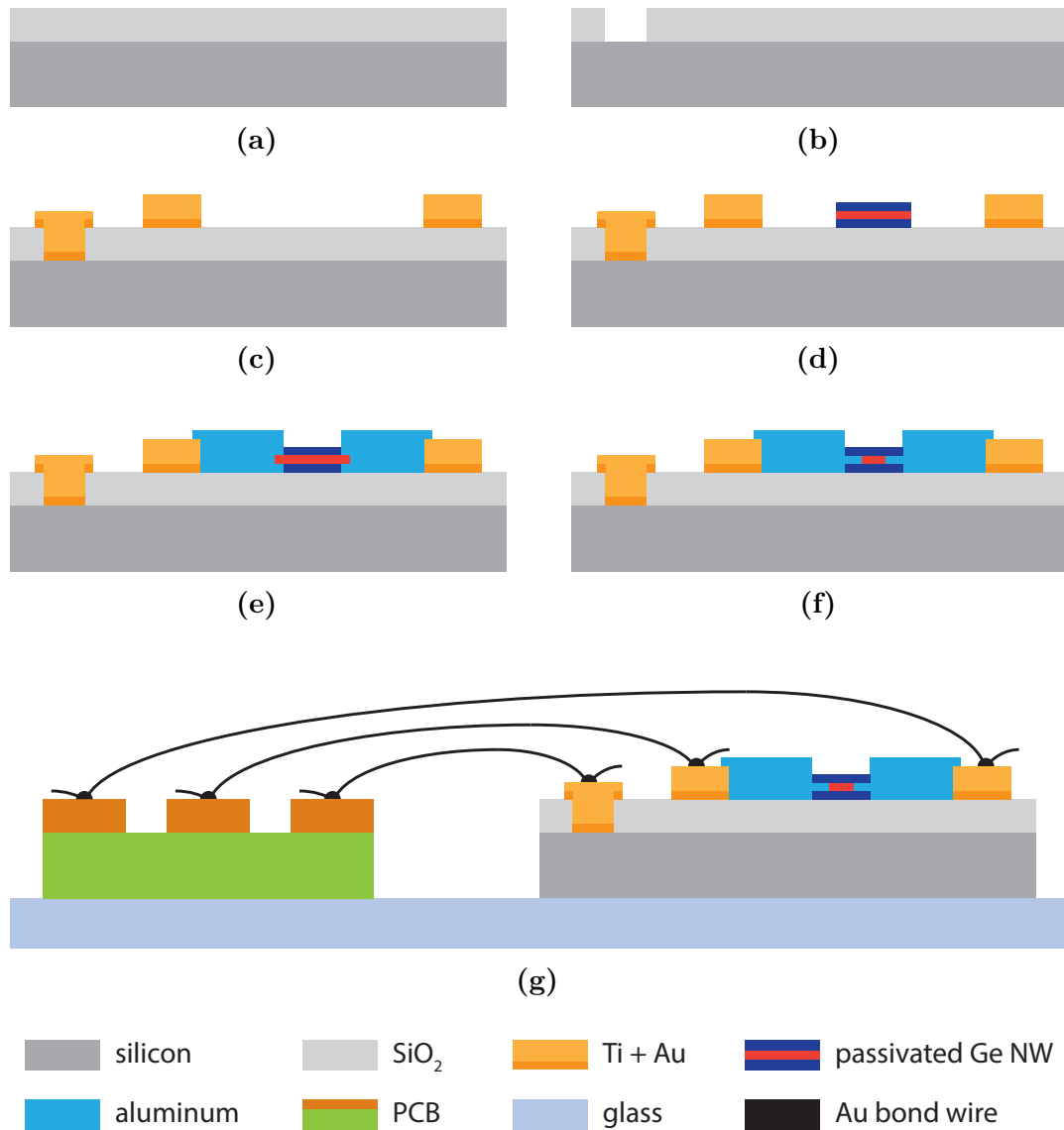


Figure 3.1: Sketch of the device processing steps for the integration of Ge NWs into the measurement module. (a) Bare Si substrate with 100 nm thick thermally grown oxide on top. (b) Vias for back-gate contacts are etched into the oxide with BHF. (c) A second photolithography step and sputter deposition of Ti/Au followed by a lift-off process allows the formation of macroscopic contacts. (d) Random dispersion of Al₂O₃ passivated NWs on the surface. (e) Contact formation via EBL and Al sputtering. (f) RTA induces an exchange process of Al and Ge in the NW and small Ge segments with sharp interfaces are formed. (g) Gluing the sample onto a glass microscope slide allows the contact formation to a PCB via wire bonding. The back-gate contact is shared by all NWs on the substrate.

3 Experimental

(d) The starting point for the photoactive elements are intrinsic $\langle 111 \rangle$ -oriented Ge NWs, as they were grown via the VLS mechanism on a Si substrate. In a first step, they are passivated with 20 nm Al_2O_3 in an ALD process. This is necessary in order to prevent the sensitive Ge/GeO_x interface from ambient atmosphere so that adsorbates like H_2O are efficiently kept off the surface, which would otherwise irreproducibly change the surface conditions and directly influence electron transport through the NW. Using ALD enables uniform all-around deposition on nanostructures with high aspect ratios and is therefore perfectly suited for the passivation of NWs [118]. It is carried out on a Cambridge NanoTech Savannah 100 using the process gases Trimethylaluminum ($\text{C}_3\text{H}_9\text{Al}$) and water (H_2O). In order to deposit NWs on the measurement module, the growth substrate is submerged into isopropanol and treated in an ultrasonic bath. Under proper conditions, NWs break from the substrate and can then be dispersed on the module by simply drop casting the resulting solution via a micropipette. This process can be repeated until the density of NWs on the measurement module is sufficiently high.

(e) After randomly dispersing NWs on the measurement module, certain NWs with desired diameter and length are chosen to be contacted to the Au pads. The patterning of the microscopic contacts is achieved by using a Raith e-LiNE electron beam lithography (EBL) system. After manually defining the contact paths, they are written with high resolution into a positive spin coated resist (PMMA) by the means of an electron beam. By dipping the sample into a developer solution, the resist is removed on exposed areas. In order to remove the Al_2O_3 and GeO_x layers at the contact areas of the NW, it is subsequently dipped into BHF and hydroiodic acid (HI). This is followed by sputter deposition of a 100 nm thick Al layer and removing the excess metal via a lift-off process.

(f) To define channel lengths without any lithographic restrictions, a diffusion mechanism is exploited, in which a thermal induced exchange reaction between the Ge NW and the Al pads reduces the size of the Ge segment [25, 117]. This process is enabled by annealing the sample in an RTA step at approximately 350 °C. By designing different contact gaps and varying the annealing time, a wide range of channel lengths can be fabricated down to 10 nm [26]. The average diffusion rates of Al into the Ge NWs were experimentally determined by M. Sistani and are in the range between 2.5 and 4 nm s⁻¹ at 350 °C [26]. By optimizing the process, Ge NWs with desired channel lengths can be fabricated, which are contacted in a very defined way by single-crystalline Al.

(g) Conducting electrical and optical measurements require mounting the measurement module on a glass microscope slide. To achieve a reliable connection, silver conductive paint is used as an adhesive. After that, the gold pads are wire bonded to

the conductive paths of a printed circuit board (PCB), which is glued on the same glass slide using epoxy resin. The larger contacts on the PCB allow for soldering of socket strips, which can further be contacted to various electrical measuring instruments.

A fully featured device fabricated in the course of this thesis is depicted in figure 3.2. It illustrates how individual Ge NWs are subsequently contacted to larger structures until they can be connected to measurement instruments via standard cables. A Ge segment featuring a channel length of only 85 nm and abrupt interfaces can be seen clearly in the SEM image. The macroscopic Au contacts on the measurement module are organized in hexagonal structures and are used for wire bonding to a PCB.

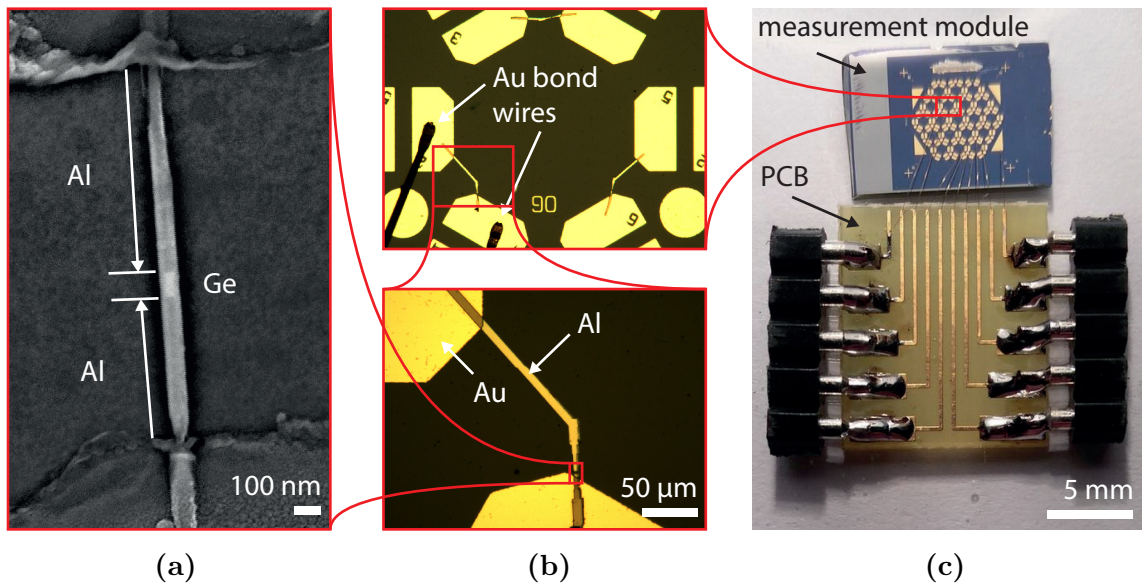


Figure 3.2: (a) SEM image and (b) optical images of a Ge NW contacted to macroscopic contact pads via sputtered Al leads. (c) Fully featured device after gluing and wire bonding to a PCB.

3.2 Electrical Characterization

A schematic illustration of the measurement setup for electrical characterization is given in figure 3.3. In order to measure the electrical properties of the NW devices, low-noise source measure units (SMU) are connected to the PCB via coaxial cables. Drain-source voltage (V_{DS}) is applied using a Keithley 6430 Sub-Femtoamp

Remote SourceMeter, while the gate is connected to a Keithley 2635A SourceMeter. By remote controlling V_{DS} using a LabView program, the current through the channel (I_D) is monitored either as a function of time or bias voltage. For the majority of measurements the gate voltage (V_G) is manually switched in the range between -15 and 15 V and the leakage current (I_G) is inspected to be in the range of only several picoamperes. To avoid influences from ambient light and radiation, the sample is placed into a lightproof metal box.

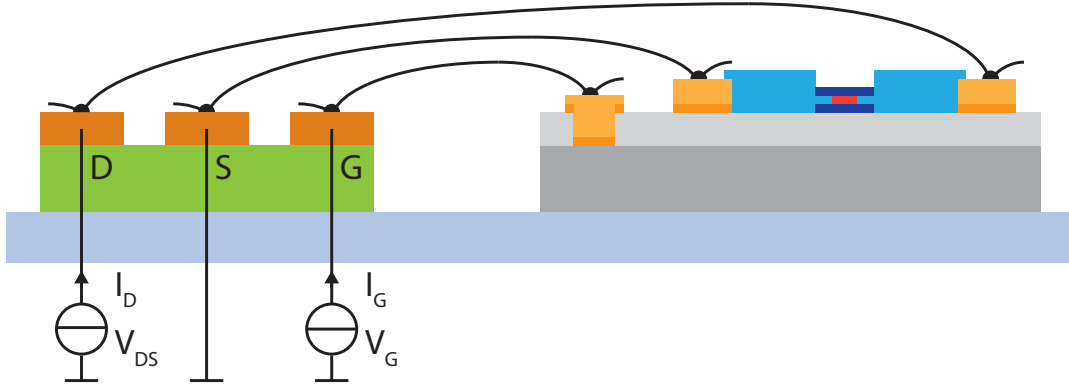


Figure 3.3: Schematic illustration of the measurement setup for electrical characterization of individual Ge NWs. A drain-source voltage (V_{DS}) is applied along the NW and the drain-current (I_D) is monitored. An additional back-gate voltage (V_G) is applied in some measurements via a second SMU. The resulting gate leakage current (I_G) is inspected to be in the range of only several picoamperes.

3.2.1 I/V Characteristics

In order to gain information of the resistivity and contact properties of the NW devices, current-voltage (I/V) sweeps are performed. Due to the Schottky contacts on both sides of the NW, typically a non-linear dependency is observed, which corresponds to two diodes connected in opposite direction. Nevertheless, by linear fitting of the curve, a resistance can be estimated according to $R = \Delta V / \Delta I$, which corresponds to a resistivity

$$\rho = \frac{RA}{L} \quad (3.1)$$

where A is the cross section and L is the channel length of the NW. Since only two-point measurements are performed, the data contains an additional series resistances originating from the contacts as well as the measurement leads.

Depending on channel length, the I/V characteristics of investigated devices are measured in the range of -1 to 1 V in steps of 1 mV or 10 mV. While sweeping V_{DS} , I_D is monitored and a compliance current is set to 1 μ A to prevent thermal failure of the NW. The back-gate voltage is set to 0 V for most I/V measurements presented in this thesis.

3.2.2 Transfer Characteristics

As can be seen in figure 3.3, the investigated NW devices essentially resemble back-gated FETs. Thus, the carrier concentration and therefore the electrical transport through the channel can be electrostatically modulated by applying gate voltage. Since recording transfer characteristics requires to sweep V_G while measuring I_D , a different setup is used, in which the devices are directly connected in a needle probe station. An HP 4156B Semiconductor Analyzer with four independent SMUs is employed, which automatically measures transfer characteristics in a given range and transmits the generated data via GPIB port to a connected PC.

In the conducted measurements, V_{DS} is fixed at a certain voltage, while V_G is linearly ramped between -15 and 15 V in both directions. Delay times are set to 0 s and voltage steps are chosen to be 500 mV in order to carry out the measurement as quick as possible. Pronounced hysteresis effects are observed, which manifest the existence of surface traps.

3.2.3 Transient Characteristics

To investigate the influence of surface traps on the electron transport through the NW, transient measurements are carried out, whereby I_D is recorded as a function of time. As will be discussed in chapter 4, traps can be depleted or filled by changing the externally applied gate voltage. Since time constants are in the range of up to several minutes, the influence of trapping can be explored by monitoring the change of I_D over time.

To measure transient curves on investigated structures, V_{DS} is fixed at a certain voltage. While subsequently changing V_G between -15 and 15 V, I_D is monitored in steps of approximately 1 s. Reproducible changes of I_D over several orders of magnitude can be observed at a fixed gate voltage, which indicates a very high electrostatic influence of surface traps.

3.2.4 Characterization at Cryogenic Temperatures

Additional transient measurements are conducted at low temperatures by using a liquid nitrogen cryostat setup. Therefore, the sample is glued onto a thin piece of glass for electrical isolation and then together with a PCB onto a copper plate. The feedthroughs of the cryostat are used to connect the sample to an HP 4156B Semiconductor Analyzer on which the measurements are conducted. Subsequently, the chamber is evacuated by using a turbomolecular pump and liquid nitrogen is filled in through a funnel at the top. This setup allows for characterization down to temperatures of approximately 80 K.

3.2.5 Negative Differential Resistance

Since the Ge NWs studied in the course of this thesis exhibit p-type behavior, usually NDR is not obtained. However, due to the strong gating effect of surface traps, the NWs can be pushed into a regime where transport becomes dominated by electrons. As stated in section 2.3.6, n-type Ge can exhibit NDR due to the particular band configuration of the conduction bands. In this thesis, NDR measurements are used as a further prove of the proposed model for the observed transient effects.

In order to invert the channel, the negative traps are depleted by applying -15 V back-gate voltage for several minutes until the current through the NW stabilizes. By manually switching V_G quickly to 15 V, the traps remain discharged because of their long filling time constants and the channel effectively senses a high positive gate. By doing I/V measurements directly after switching the gate, NDR can be observed, which gets weaker over time as the traps start to refill with electrons again.

3.3 Optical Characterization

To explore photodetecting properties of the fabricated Ge NW devices, a discrete optical measurements setup was designed and installed. As shown in 3.4, a laser beam generated in a NKT SuperK Extreme white light laser source is fed into a NKT SuperK Select acousto-optical tunable filter (AOTF) via an optical fiber. The two AOTFs act as monochromators with separated channels for visible, infrared and near-infrared light. Dependent on the selected wavelength, they exhibit an output linewidth of approximately 10 to 20 nm. From there, monochromatic light is further

guided through a polarization maintaining FD7 PM fiber to a collimator, where a parallel beam is created with linear polarization oriented in the horizontal plane. Depending on the desired output power and wavelength, various optical filters are utilized before the beam is focused via an optical lens onto the sample.

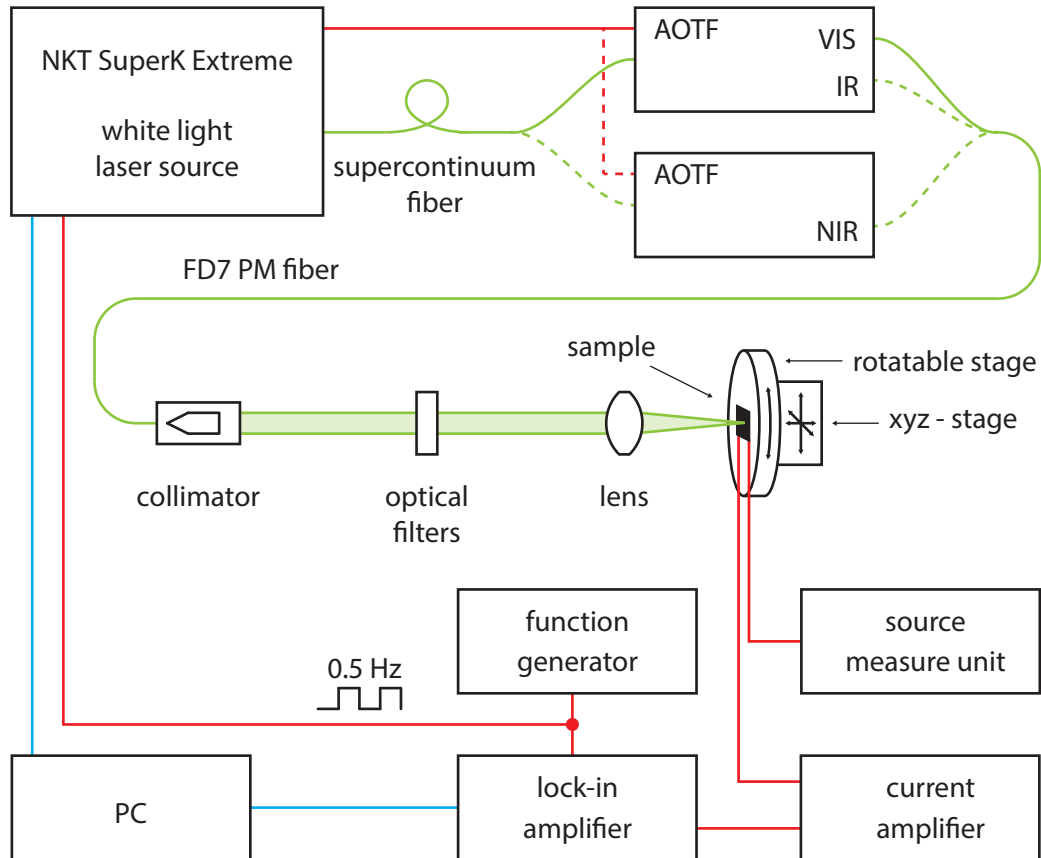


Figure 3.4: Sketch of the optical measurement setup, which is mounted on top of a pneumatically damped optical table. Green, red and blue lines represent optical fibers, electrical interconnects and GPIB cables, respectively.

The sample is mounted onto a rotatable stage, which is used to adjust NW orientation with respect to the polarization of the incident laser beam. Therefore their orientation on the sample is measured beforehand under an optical microscope. Measurements are carried out such that the electrical field of incident light is parallel to the NW axis. An xyz-stage in combination with a magnifying camera is used to align the laser spot onto the NW. As soon as photoresponse can be measured, the signal is maximized by using the micrometer screws of the stage. This procedure ensures that the laser spot is perfectly aligned on the sample, which is a prerequisite for

3 Experimental

calculating the proper absorbed light power. Figure 3.5 schematically depicts the setup from the viewpoint of the device. Polarized light with defined wavelength is incident on the NW. Various mechanisms lead to the generation of photocurrent (I_{ph}), which can be measured by taking the difference of the signal with and without laser illumination.

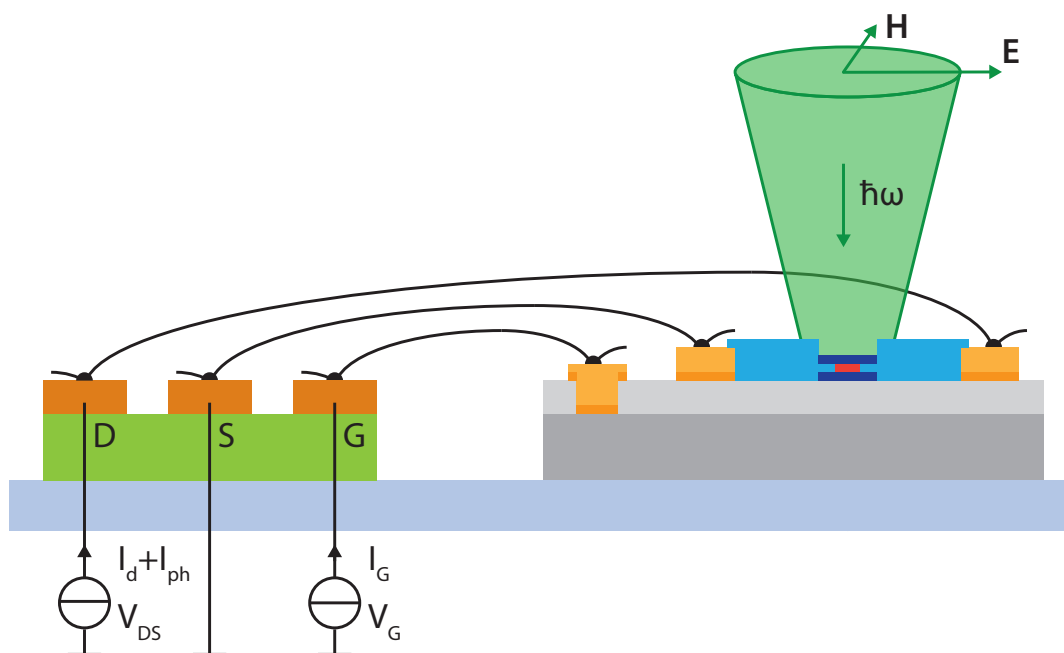


Figure 3.5: Schematic illustration of the measurement setup for optical characterization of individual Ge NWs. Light is incident on the NW with defined wavelength and polarization oriented in longitudinal direction. A constant drain-source voltage (V_{DS}) is applied, while periodically switching the laser excitation on and off. Difference in drain current correlates to the photocurrent (I_{ph}) and can be measured efficiently by employing a lock-in amplifier.

3.3.1 I/V Characteristics under Illumination

In order to study effects of light absorption on the carrier transport through the devices, measurements are conducted in which I/V curves are recorded under laser illumination. Using a Keithley 6430 Sub-Femtoamp Remote SourceMeter, bias voltage is swept between -1 and 1 V in steps of 1 mV or 10 mV depending on channel length. Simultaneously, a laser beam is directed onto the device with a power of 10 μ W. The wavelength is set to 532 nm in order to gain comparable results to a second setup featuring a Nd:YAG-Laser. An additional Thorlabs NB530-10 bandpass filter is employed to block any background radiation originating from the white

light laser source. By calculating the difference of the I/V curves with and without illumination the photocurrent can be evaluated as a function of bias voltage. A picture of the measurement setup is depicted in figure 3.6.

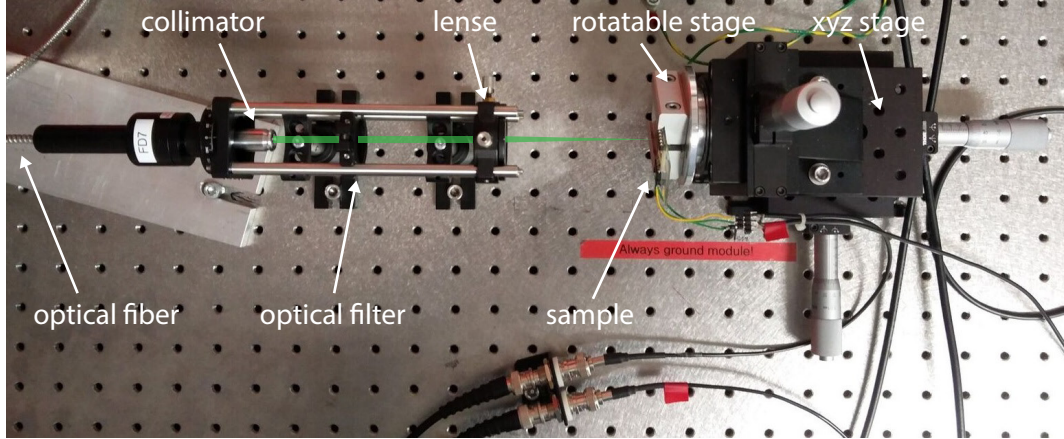


Figure 3.6: Photograph of the measurement setup for conducting various optical measurements. A graphically added green line demonstrates the path of the laser beam.

3.3.2 Laser Beam Power Dependent Measurements

The dependency of the photocurrent on the laser beam power is investigated on the same setup as the I/V characteristics. However, in order to measure the drain current, a Keithley 428 Current Amplifier is utilized, which is connected to an EG&G 7265 Lock-In Amplifier via coaxial cables. By generating a rectangular signal with a nbn FG300 Synthesized Function Generator, the laser is pulsed at a frequency of 0.5 Hz. The lock-in amplifier is set to detect only changes of the drain current which occur at the exact same frequency and is therefore perfectly suited to measure the generated photocurrent. The whole measurement can be controlled on a PC, which is connected to the lock-in amplifier and the white light laser source via GPIB.

In order to conduct comparable measurements with devices of unequal channel lengths, the electrical field along the NWs is kept constant at $E_{DS} = 10^4 \text{ V cm}^{-1}$. This value, which is approximately one order of magnitude smaller than the breakdown field of Ge [69], was shown to be the optimum in terms of maximizing photocurrents while simultaneously keeping dark currents low. The gain of the Keithley 428 current amplifier is set to 10^6 V A^{-1} and a current suppression is activated, which roughly cancels out the dark current. To vary the laser power over a range of 4 magnitudes, optical filters are employed as listed in table 3.1.

Table 3.1: *Applied optical filters of the brand Thorlabs to achieve the respective output laser power on the sample.*

Laser power on sample P_L	Original laser power $P_{L,0}$	Used filters
100 μ W	100 μ W	–
32 μ W	100 μ W	NE05B
10 μ W	100 μ W	NE10B
3.2 μ W	100 μ W	NE10B, NE05B
1 μ W	100 μ W	NE20B
320 nW	100 μ W	NE20B, NE05B
100 nW	1 μ W	NE10B
32 nW	1 μ W	NE10B, NE05B
10 nW	1 μ W	NE20B

3.3.3 Modulation Frequency Dependent Measurements

For getting an insight on how trapping times influence the photocurrent, measurements are conducted at different laser puls modulation frequencies up to 100 kHz. Therefore, the laser power is set to 1 μ W at a wavelength of 532 nm. The bias voltage is held constant and the variation of the photocurrent is measured by using a lock-in amplifier. Care must be taken on the amplification factor, which is dependent on frequency as well (see section 3.3.5). Using these measurements, a deeper insight in the dynamic behavior of the trapping process can be gained.

3.3.4 Wavelength Dependent Measurements

The study of trapping energies is carried out by sweeping the wavelength of the incident light. To do so, the bias voltage is held constant again and the wavelength is varied from 500 nm to 1100 nm in steps of 50 nm by using the provided software. The photocurrent, which is measured by using a lock-in amplifier at a modulation frequency of 0.5 Hz, is kept constant by manually sweeping the laser power. This procedure ensures that possible saturation effects are equally pronounced at each wavelength and are therefore not distorting the results. The laser power is subsequently measured by the means of a calibrated photodiode and used to determine the photoconductive gain.

3.3.5 Lock-In Amplifier Measurement Technique

A lock-in amplifier enables the reliable detection of signals with known frequency out of a noisy environment. For this purpose, the input signal is multiplied by a reference signal, which defines the desired measurement frequency, and integrated over a specified time. This operation can be mathematically described by the cross-correlation, which yields

$$V_{out}(t) = \frac{1}{T} \int_{t-T}^t \sin(2\pi f_{ref}s + \varphi) V_{in}(s) ds \quad (3.2)$$

for the output signal of the lock-in amplifier, where T is the integration time and φ is the phase. Considering a rectangular in-phase input signal, which is generated in an ideal photodetector by periodically switching the excitation laser on and off, the output signal calculates to

$$V_{out} = \frac{2}{T_{ref}} \int_0^{T_{ref}/2} \sin(2\pi f_{ref}s) \frac{V_{in,pp}}{2} ds = \frac{1}{\pi} V_{in,pp} \approx 0.318 V_{in,pp} \quad (3.3)$$

where $T_{ref} = 2\pi/f_{ref}$ is the period duration of the signals and $V_{in,pp}$ is the peak-to-peak voltage of the input signal. However, due to internal conversion factors, deviations from this theory can be obtained. To measure the amplification characteristic of the utilized lock-in amplifier of the type EG&G 7265, a defined rectangular input signal generated by a function generator, is utilized. As depicted in figure 3.7a,

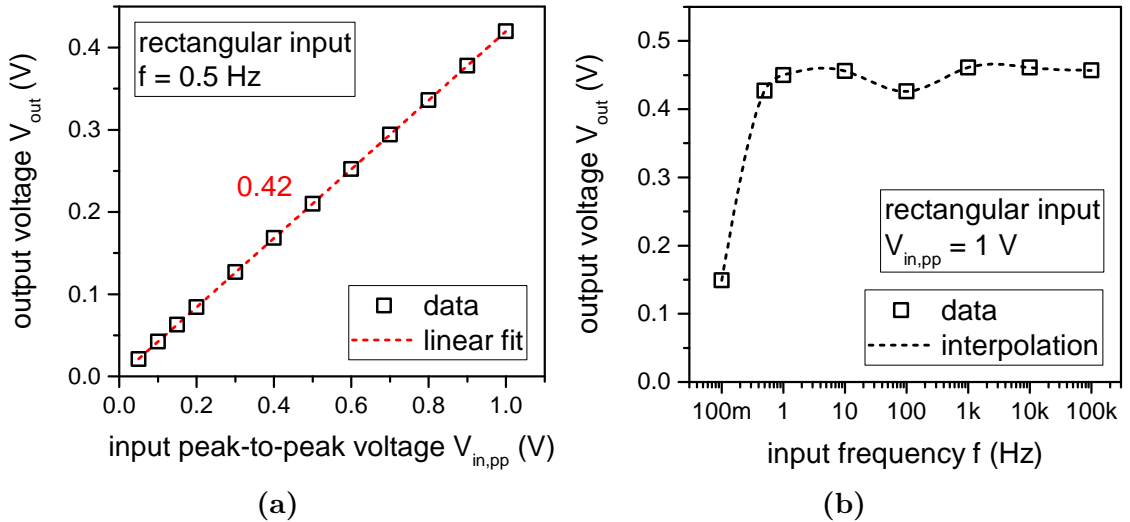


Figure 3.7: Amplification characteristic of a EG&G 7265 Lock-In Amplifier in dependency of (a) input peak-to-peak voltage and (b) input frequency.

the obtained characteristic is linear over the measured range, but with a slightly higher amplification factor of 0.42. Furthermore, a dependence on input frequency could be observed as can be seen in figure 3.7b.

In order to measure photocurrent, the drain current of the NW is amplified by a current amplifier and the output voltage is fed into the lock-in amplifier. The photocurrent, which corresponds to the peak-to-peak value of the input signal, can then be directly obtained from the lock-in amplifier by calculating

$$I_{ph} = \frac{V_{out}}{g_{lockin} g_{curr}} \quad (3.4)$$

where $g_{lockin} = 0.42$ is the gain of the lock-in amplifier and g_{curr} is the gain of the current amplifier in V/A. A lock-in amplifier enables therefore the direct measurement of photocurrents at very high noise levels.

3.3.6 Determination of the Laser Beam Profile

In order to calculate the incident optical power on the NWs, the beam profile on the sample has to be known. Therefore, a Thorlabs S121C standard photodiode power sensor, which is connected to a Thorlabs PM100D optical power console, is placed onto the rotatable stage instead of the sample. The laser is set to a wavelength of 532 nm at a power of 100 μ W. Subsequently, a Thorlabs PS5 precision pinhole with 5 μ m diameter is mounted onto the photodiode. By moving the stage in steps of 10 μ m in either vertical or lateral direction, while keeping the other direction at the position with maximum power, a normalized beam profile can be generated as depicted in figure 3.8. The obtained data can be fitted quite well by the means of a Gaussian distribution given by

$$f(x) = \frac{1}{\sigma\sqrt{2\pi}} \exp\left(-\frac{(x-\mu)^2}{2\sigma^2}\right) \quad (3.5)$$

where σ is the standard deviation and μ is the mean value, which is chosen to be 0 in this case. The full width at half maximum (FWHM) diameter of the laser spot on the sample calculates to

$$FWHM = 2\sqrt{2 \ln 2} \sigma \quad (3.6)$$

which gives 87.5 μ m for this measurement setup.

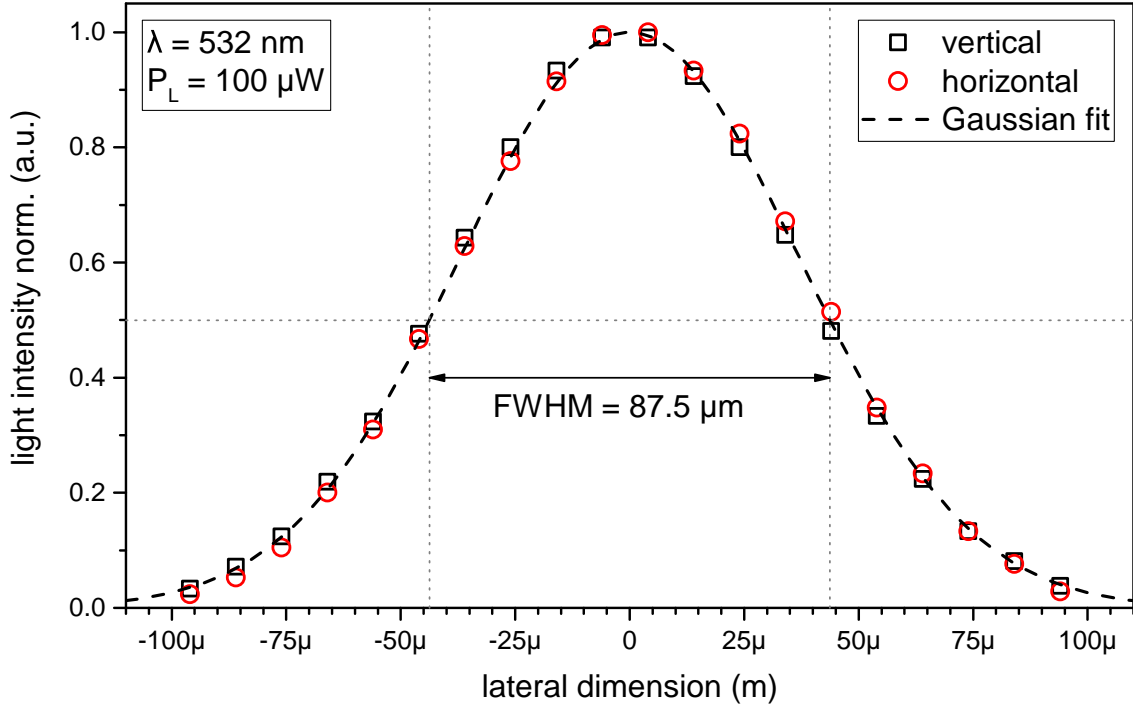


Figure 3.8: Beam profile of a 532 nm laser incident on the sample in vertical and horizontal direction. A Gaussian distribution with a FWHM of 87.5 μm gives a very good fit for the experimental data.

3.3.7 Calculation of the Photoconductive Gain

According to (2.39) and (2.40), the overall photoconductive gain can be expressed as

$$g = \frac{I_{ph}/e}{P_{opt}/(h\nu)} = \frac{\text{detected electrons per second}}{\text{absorbed photons per second}} \quad (3.7)$$

where e is the elementary charge and $h\nu$ is the photon energy. The photocurrent I_{ph} can be measured by using a lock-in amplifier as described in section 3.3.5. However, to calculate the absorbed optical power P_{opt} several considerations are necessary, which are elaborated on below.

In order to determine the optical power incident on the NW, the overlap \mathcal{O} of the active NW area with the Gaussian shaped laser beam has to be calculated. When assuming perfect alignment, this can be achieved by numerically integrating the center of the two-dimensional distribution function over the rectangular NW area,

3 Experimental

which gives

$$\mathcal{O} = \int_{-L/2}^{L/2} \int_{-d/2}^{d/2} \frac{1}{2\pi\sigma^2} \exp\left(-\frac{x^2 + y^2}{2\sigma^2}\right) dx dy. \quad (3.8)$$

For a channel length of $L = 1 \mu\text{m}$, a diameter of $d = 30 \text{ nm}$ and a laser spot size of $FWHM = 87.5 \mu\text{m}$, the overlap calculates to $3.45 \cdot 10^{-6}$. This means that only 345 out of 100 million photons hit the NW when it is placed exactly in the center of the laser spot.

The fraction of photons absorbed can be estimated by using the Beer-Lambert law (2.24). Assuming a circular cross section of the wire, a non-uniform material thickness is observed with respect to the direction of incident light. By integrating (2.24) over the diameter of the NW using according thickness ($2\sqrt{(d/2)^2 - y^2}$), the corresponding transmittance \mathcal{T} can be obtained as

$$\mathcal{T} = \int_{-d/2}^{d/2} \frac{1}{d} \exp\left(-2\alpha\sqrt{\left(\frac{d}{2}\right)^2 - y^2}\right) dy \quad (3.9)$$

where α is the absorption coefficient depicted in figure 3.9a. When reflection is neglected the fraction of absorbed light (absorbance \mathcal{A}) in the NW calculates to

$$\mathcal{A} = 1 - \mathcal{T}. \quad (3.10)$$

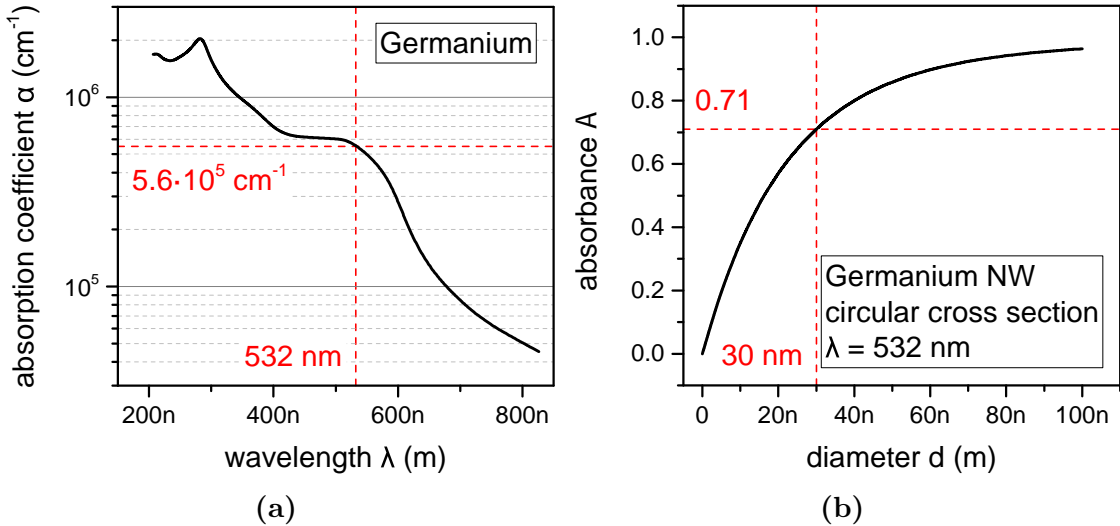


Figure 3.9: (a) Optical absorption coefficient of Ge as a function of wavelength. Data taken from [119]. (b) Absorbance in a Ge NW depending on diameter as calculated by using (3.10).

Figure 3.9b depicts the absorbance of Ge NWs as a function of diameter at a wavelength of 532 nm. At a NW diameter of 30 nm, about 71 % of the incoming light is absorbed, when resonance effects like leaky modes are neglected.

After measuring the total power of incident laser light P_L with a calibrated photodiode, the absorbed optical power can finally be calculated to

$$P_{opt} = P_L \mathcal{O} \mathcal{A} \quad (3.11)$$

which enables the determination of the photoconductive gain by using (3.7).

Results and Discussion

This chapter is dedicated to the presentation and discussion of the experimental results obtained throughout the course of this thesis. In the first part, the results of the electrical characterization, which focuses mainly on the study of surface trapping of Ge NWs, are discussed. Subsequently, results of the optical characterization are presented in order to demonstrate how these surface effects are able to enhance photo-sensitivities of Ge NWs. Various measurements are conducted in order to draw conclusions on the dynamic and wavelength dependent behavior of the detectors.

4.1 Electrical Characterization

In order to discuss optical properties and mechanisms of photoconductivity in Ge NWs, their electrical behavior must be understood precisely. Therefore, various measurements are carried out to investigate in particular the filling of surface traps and the related effects on electrical transport. Previous publications [86, 92] have already addressed surface effects of Ge NWs and are used as a frame of reference in order to discuss the following experiments.

Measurements are conducted on numerous NWs, out of which five characteristic devices are chosen to present the obtained results. They are listed together with their physical dimensions in table 4.1. All of them feature an all-around passivation with 20 nm Al_2O_3 , which was deposited in an ALD process. Different segment lengths are chosen to demonstrate the effects of spatial restrictions.

Table 4.1: *Physical dimensions of characteristic NW devices investigated within the course of this thesis.*

NW	channel length L	diameter d
1	1940 nm	53 nm
2	650 nm	30 nm
3	230 nm	32 nm
4	85 nm	35 nm
5	45 nm	35 nm

4.1.1 I/V Characteristics

In a first experiment, I/V characteristics are measured in order gain information of resistivity and contact properties. The obtained results are plotted in figure 4.1 for NW devices with various channel lengths. Non-linear behavior is observed, which originates from the Schottky contacts on the Al/Ge interface [25]. With decreasing channel lengths, the curves tend to get more linear as can be clearly seen for the 45 and 85 nm devices. This is an indication that part of the charge carriers start to travel ballistically through the channel without scattering, which is plausible, considering a mean free path for Ge of approximately 35 nm [26]. To extract resistances out of the measurements, a linear fit is applied near the point of origin, which is schematically

shown for the 230 nm long NW in the inset. The reciprocal of this slope corresponds to the resistance of the channel.

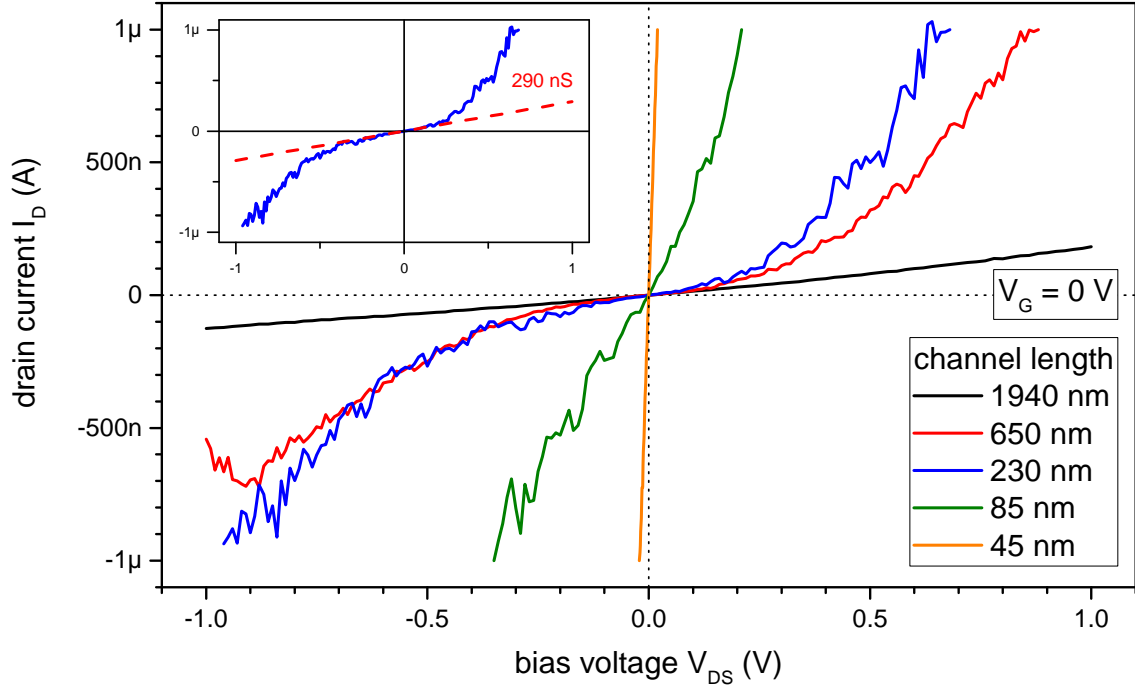


Figure 4.1: I/V characteristics for Ge NWs with various channel lengths at 0 V back-gate voltage. Data was measured for bias voltages in the range between -1 and 1 V and a current compliance was set to 1μ A. The inset schematically shows how the resistance of non-linear devices is extracted out of the data by linear fitting near the point of origin.

Figure 4.2 depicts the according resistances for all investigated devices as a function of channel length. A linear increase can be observed, which is in agreement with theory, since $RA = \rho L$ in ohmic systems (3.1). Although only two-point measurements are performed, the influence of parasitic contact resistances seems to be negligible, as the intersection of the linear fit with the y -axis is nearly at zero. This can be mainly attributed to the high resistances of intrinsic Ge in comparison to the leads consisting out of Cu, Au and Al. Also the contact resistance originating from the Schottky barriers seems to have low influence on the measurements. The resistivity is given by the slope and calculates to $\rho = 0.75\Omega\text{ cm}$, which is in accordance with previously reported resistivities of nominally undoped Ge NWs [86, 92]. This value corresponds to an impurity concentration of roughly $3 \cdot 10^{15}\text{ cm}^{-3}$ in p-type bulk Ge as can be extracted from figure 2.5. Considering the high amount of surface states in Ge NWs as reported in section 2.4 combined with their large surface to volume ratio, this relatively high value seems to be plausible. The associated position of the

Fermi level can be estimated by using (2.11) with an effective density of states in the valence band of $6.0 \cdot 10^{18} \text{ cm}^{-3}$ [69]. It is found to lie approximately 0.20 eV above the top of the valence band.

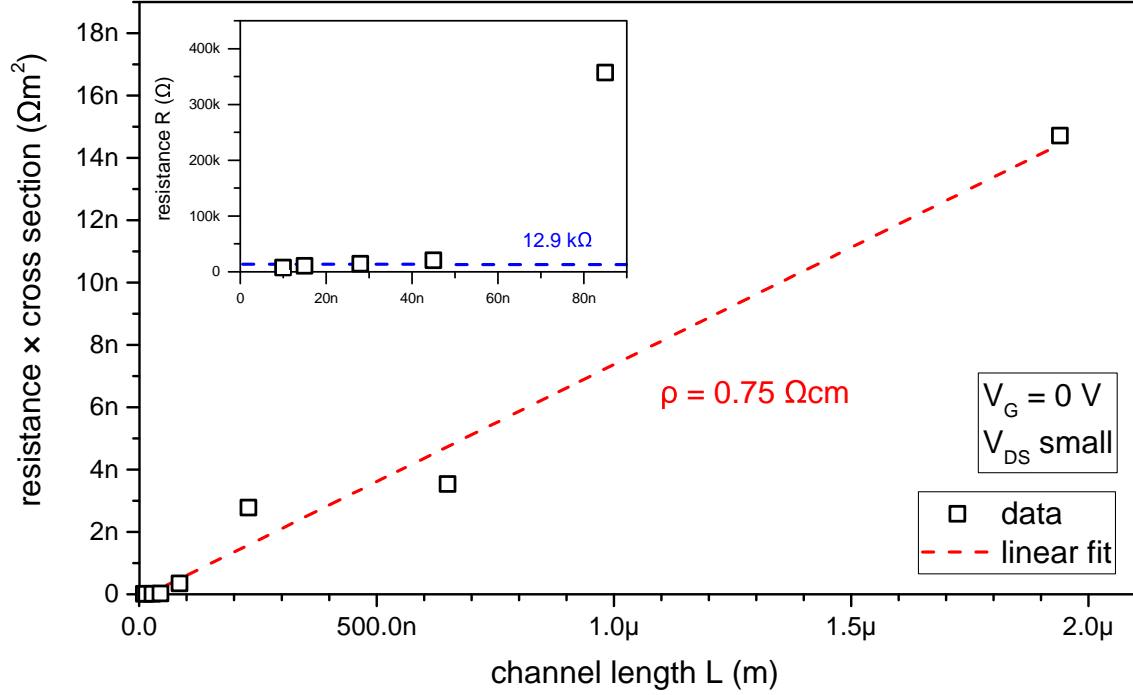


Figure 4.2: Resistance for various channel lengths as extracted from the I/V s in figure 4.1. To account for differences in diameter, the resistance is multiplied by the cross-section of the NWs. A linear increase indicates only minor influences of parasitic effects as they originate from Schottky contacts. The inset shows the resistance at very small channel lengths including three additional devices. The fundamental resistance of 12.9 k Ω , which is indicated by the blue dashed line, is the lower limit revealing ballistic transport below 45 nm.

Simulations show, that because of the small thickness of the NWs, spatial confinement takes place and only one mode for electron transport originates. Thus, the current is limited by the amount of charges that can be carried in a single mode, which is usually expressed as the conductance quantum $G_0 = 2e^2/h$ [120]. The reciprocal of this value calculates to approximately 12.9 k Ω , which is the theoretical resistance obtained in ballistic systems. In order to study this effect, the resistance of NWs with very short segment lengths is investigated on three additional devices. The inset of figure 4.2 shows that the resistance, once this fundamental limit is reached, does not decrease any further. Thus, ballistic transport seems to be the dominant mechanism for channel lengths below 45 nm, which is in accordance with theory since the mean free path is in the order of 35 nm in this structure [26].

4.1.2 Transfer Characteristics

Transfer characteristics are conducted in order to determine the modulation capability of the charge carrier concentration in the NWs. By applying gate voltage, the Fermi level of the semiconducting NW can be shifted efficiently, which in return changes the carrier concentration and therefore the conductivity in the channel. Thus, the devices work by directly changing the resistance in the channel rather than modulating the junction at the contacts, which is the basic working principle of a junctionless field effect transistor (JLFET) [121, 122].

Although nominally undoped, p-type behavior is observed for all investigated NWs, which can be seen clearly by conducting transfer characteristic measurements. Experimental data for the device with $L = 1940$ nm is plotted in figure 4.3. At 0 V gate voltage the channel is moderately p-type and the resulting current is consequently relatively low. By reducing V_G , the Fermi level gets shifted towards the valence band, which increases the hole concentration according to (2.6) and therefore also the current through the channel. On the other hand, by increasing V_G , the Fermi energy approaches the band gap center and the conductivity decreases until a certain level, where the intrinsic Fermi level is reached. From there on, inversion takes place and the current starts to increase again since electron transport is dominating in this regime. This ambipolar behavior is characteristic for JLFETs and commonly observed in semiconductor NWs [123]. The remaining asymmetry can be attributed to the contacts, which are not perfectly ohmic, but exhibit Schottky barriers with Fermi level pinning near the valence band. Despite the simple architecture, a remarkable I_{on}/I_{off} ratio of nearly 10^5 can be observed for the fabricated devices at room temperature.

In a simplified model (i.e. no barriers at the contacts and no band bending across the wire) it can be assumed that the conductivity at the lowest point of the transfer characteristic corresponds to the conductivity of the intrinsic semiconductor. In the measurements, this value is found to be $\sigma_i = 2.37$ mS cm⁻¹ in the case of the 1940 nm device as indicated in figure 4.3. This is the point where the Fermi level is equal to the intrinsic Fermi level and the number of free electrons and holes are therefore equal to the intrinsic carrier density n_i . Using (2.17) and assuming equal mobilities for electrons and holes, the equation for the intrinsic conductivity can be written as

$$\sigma_i = 2e\mu n_i \quad (4.1)$$

which allows for the calculation of the mobility in the channel. Although a few simplifications are made, a realistic value of $\mu = 317$ cm²/Vs is found, which fits to

values of Ge NWs reported in literature [92]. The lower mobility compared to bulk Ge can be mainly attributed to the high scattering at the surface, which is especially dominant in thin NWs due to their high surface to volume ratio.

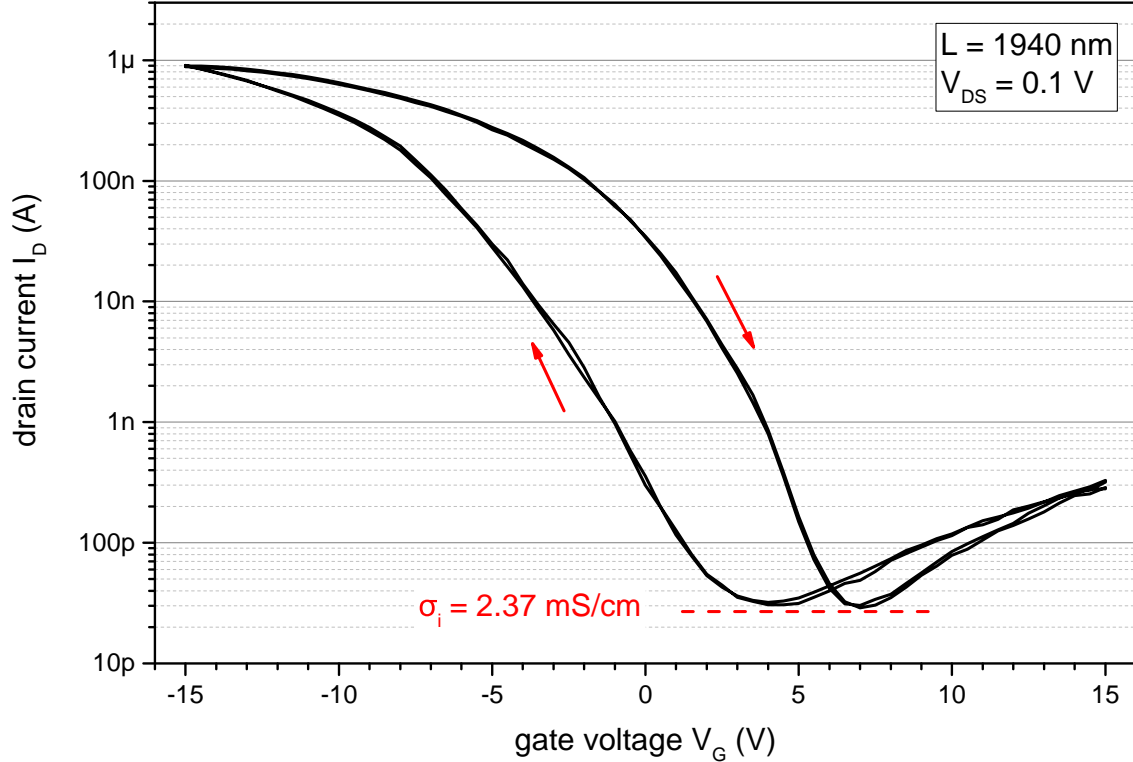


Figure 4.3: Transfer characteristic of a device with 1940 nm channel length measured two times in both directions and plotted on a semilogarithmic scale. V_{DS} is set to 0.1 V at a current compliance of $1\mu\text{A}$. Red arrows indicate the direction of measurement. Slightly ambipolar behavior is observed with a high shift towards p-type, which is in accordance with the expected effects due to surface doping. The minimal current indicates the point where the intrinsic Fermi level is reached and reveals a resistivity of 2.37 mS cm^{-1} . Further, a very high and reproducible hysteresis is observed.

Measurements further revealed a high and reproducible hysteresis of the transfer characteristics, which can be seen clearly in figure 4.3. This is attributed to the high density of surface traps as described in section 2.4. Although a proper passivation exists, GeO_x will be always present at the NW surface due to diffusion mechanisms in the annealing step of the device fabrication [124]. The purpose of the passivation is therefore mainly to keep the conditions stable and avoid influences of adsorbates rather than eliminating charge trapping due to dangling bonds on the GeO_x/Ge interface.

4.1.3 Transient Characteristics

Since the hysteresis of the transfer characteristic results from kinetic effects associated with charge trapping, a time-dependent variation of the drain current can be expected when changing the gate voltage. Therefore experiments are conducted in which I_D is monitored over time, while changing V_G abruptly between -15 and 15 V. The obtained results are plotted in figure 4.4. At $t = 0$, V_G is instantly changed from 15 to -15 V and a drain current of approximately $1 \mu\text{A}$ is observed, which is in accordance with the transfer characteristic from the previous section. Over a timespan of more than 10 minutes, I_D decreases until a steady-state value is reached. At this point another abrupt change of V_G is applied but this time from -15 to 15 V. I_D changes to 200 pA which is again in agreement with the transfer characteristic. More than 20 minutes elapse before the current reaches another steady-state value. Interestingly, a

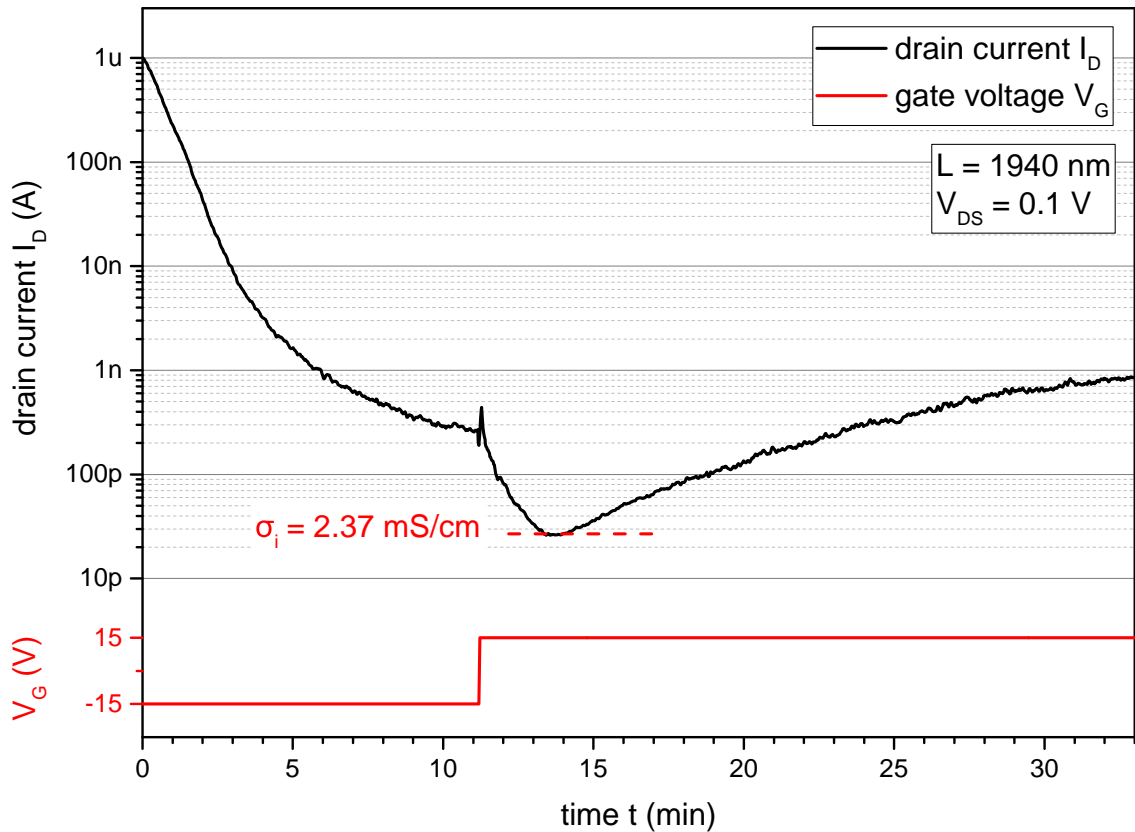


Figure 4.4: Transient behavior of a device with 1940 nm channel length for step changes in gate voltage. Before the start of the measurement, $V_G = 15 \text{ V}$ has been applied for 20 minutes. The drain current changes in the timespan of several minutes in both cases, which can be explained by the depletion and filling of slow surface states.

non-monotonic curve is observed, which has a minimum at the intrinsic conductivity determined in the previous section. This procedure is repeatable and similar results are obtained in each run.

To explain this drastic change of I_D over time, a model is proposed in which the transient behavior results from the slow redistribution of charges after changing the gate voltage. Figure 4.5 schematically illustrates the cross-sectional band structure of an intrinsic NW at different gate voltages. In equilibrium, traps below the Fermi level are filled, while those above remain empty. Since electrons are negatively charged, the channel feels an “effective” negative gate, even though zero gate voltage is applied (figure 4.5a). This results in an upward band bending and the observed p-type behavior, which is commonly reported in literature [86, 88]. Immediately after applying gate voltage, the bands shift relative to the initial surface potential. In the case of negative gate, this results in a shift of the Fermi level towards the valence band and therefore an abrupt increase of I_D (figure 4.5b). However, traps above the Fermi level are now filled and they start to discharge in order to reach equilibrium again. This process is slow, since surface states in Ge can exhibit time constants up to several minutes [61]. While traps are discharging, the “effective” gate becomes more positive, because less negative charges are now present at the surface. Therefore, the bands bend downward again and at the end a situation is reached which is very similar to the starting point, but with fewer traps filled (figure 4.5c).

On the other hand, by applying positive gate voltage, bands at the surface shift to lower energies, which results in a relative shift of the Fermi level towards the conduction band and inversion at the surface. In this regime electron transport is dominating and the magnitude of I_D can be either higher or lower than before depending on various parameters, such as the controllability of the gate or trap density on the NW. In fact, this was observed when measuring numerous NW devices on different samples. In the case of the device with $L = 1940$ nm (figure 4.4), I_D seems to stay more or less stable at the switching point which is a coincidence and can be attributed to the fact that bands are now equally bent downward as they were bent upward before (compare (c) and (d) of figure 4.5). Since now there are empty traps below the Fermi energy, they start to fill and the “effective” gate becomes more negative again. This continues until equilibrium is reached and a similar band bending as at $V_G = 0$ V is obtained but with a higher number of traps filled (figure 4.5e). During this process, the transport mechanism changes from electron to hole dominated, which causes the current to decrease at the beginning until the intrinsic point is reached.

Hanrath and Korgel [86] proposed a very similar model, but because of their weak controllability of the channel only a small change of I_D of approximately 20% was

observable. By optimizing the architecture with Al_2O_3 passivation and atomically sharp mono-crystalline Al contacts, a very high controllability could be reached and an I_D variation of more than 3 orders of magnitudes over time could be observed in the course of this thesis. Nevertheless, the underlying mechanism is exactly the same which manifests in the similar transient behavior at equal timescales.

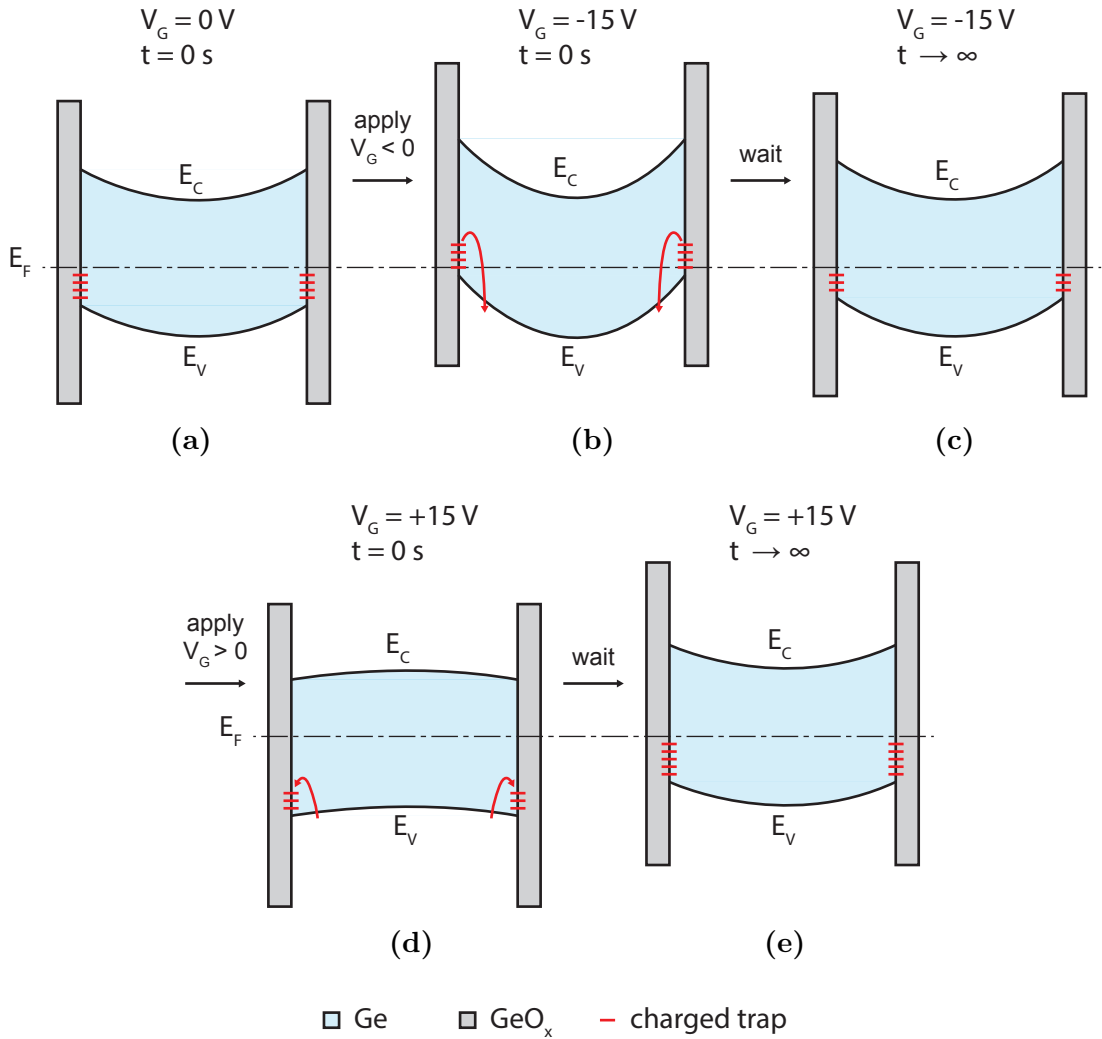


Figure 4.5: Cross-sectional band structure of a Ge NW device to discuss the proposed mechanism for the transient behavior of I_D at abrupt changes of V_G . (a) NW at $V_G = 0$ V in equilibrium. (b) After applying negative gate voltage bands bend upward, which results in discharging of the surface traps. (c) Equilibrium has been reached again but with $V_G = -15$ V and fewer traps filled. (d) Applying positive gate results in downward band bending and inversion at the surface. (e) The filling of traps causes the NW to reach equilibrium again with a higher number of traps filled.

At this point a deeper understanding of the transfer characteristic shown in figure 4.3 can be gained. Since the measurement was conducted very fast, it can be assumed that the filling of slow surface states remains nearly constant during the measurement. Using the band diagram model of figure 4.5, this corresponds therefore to a transition from (b) over (a) to (d) when measuring from -15 to 15 V. Between the latter two, a point is reached where the bands are flat and the NW is intrinsic throughout the whole cross-section. At this point the highest resistivity is obtained, which results in the minimum of I_D found in the transfer characteristics. However, if the same measurement is conducted at a much slower speed, one would expect a transition from (c) over (a) to (e) in figure 4.5, since then there is enough time for the NW to reach the equilibrium state at each measuring point. Here, almost no influence of the gate should be measurable since the filling of traps counteract the outer gate on the longterm. In fact, this could be observed in numerous measurements, which is a further prove of the proposed trapping mechanism.

To get a deeper insight in the transport mechanisms happening during the transient measurement, the trend of the Fermi level with respect to the band edges is calculated as a function of time. To do so, it is assumed that the band edges are flat throughout the whole cross-section of the NW, meaning that no cross-sectional band bending occurs as in figure 4.5. Since the investigated NWs have a very small diameter, this should be a good approximation. It is further assumed that no barriers exist at the contacts and that the mobility for electrons and holes is equal. Using these simplifications, (2.17) can be expressed as

$$\begin{aligned}\sigma &= e\mu(n + p) = e\mu n_i \left(\exp\left(\frac{E_F - E_{Fi}}{k_B T}\right) + \exp\left(-\frac{E_F - E_{Fi}}{k_B T}\right) \right) \\ &= 2e\mu n_i \cosh\left(\frac{E_F - E_{Fi}}{k_B T}\right)\end{aligned}\quad (4.2)$$

where $E_{Fi} \approx 0.33$ eV is the intrinsic Fermi level. Thus, the Fermi level can be calculated at each point, by rearranging (4.2) as in

$$E_F = E_{Fi} \pm k_B T \operatorname{arcosh}\left(\frac{\sigma}{2e\mu n_i}\right) = E_{Fi} \pm k_B T \operatorname{arcosh}\left(\frac{\sigma}{\sigma_i}\right)\quad (4.3)$$

where $\sigma_i = 2.37$ mS cm $^{-1}$ is the intrinsic conductivity determined in section 4.1.2.

Therefore, after evaluating the conductivity at each point of figure 4.4, also the Fermi energy can be calculated by using 4.3. Thereby, two results are found, which are plotted in the upper part of figure 4.6. They are representing the solutions for electron and hole dominated transport, respectively. After 11 min, a high increase in Fermi energy is expected since V_G is switched from -15 to 15 V. This and the

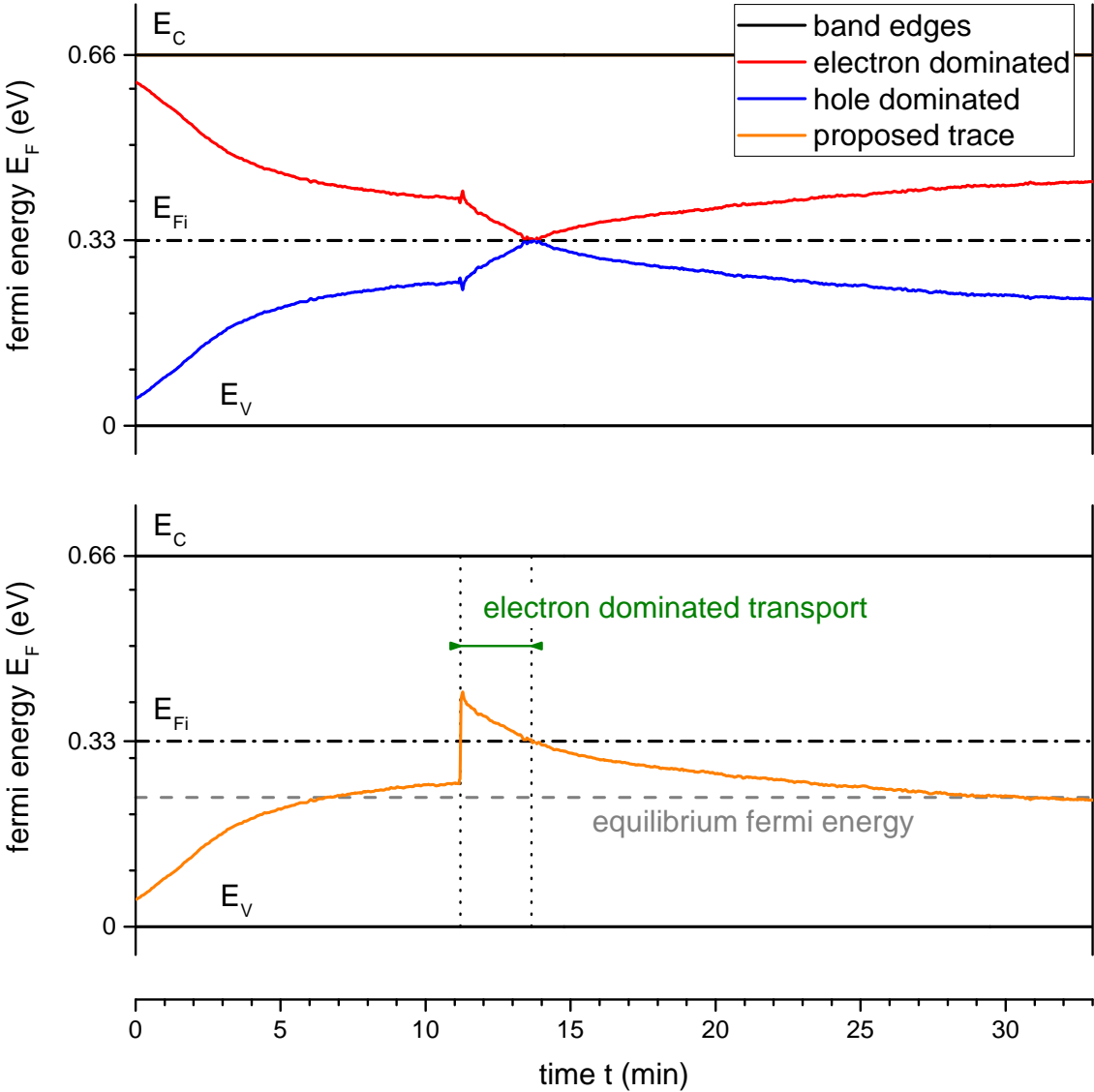


Figure 4.6: Calculated Fermi energy over time with respect to the band edges. Two solutions are found which correspond to electron and hole dominated transport, respectively. Considering previous observations and the fact that an abrupt change towards higher energies is expected at the point where the gate voltage is switched from -15 to 15 V, a trace is suggested in which the transport mechanism changes from p-type to n-type and returns after a few minutes at the point with lowest current. Thus, a short period exists where electron transport is dominating. In the longterm the devices approach an equilibrium value which is found to lie 0.23 eV above the valence band maximum.

fact that p-type behavior is observed in equilibrium, indicates that at this point the transport mechanism changes abruptly from the blue to the red curve and comes back after a few minutes when the filling of traps led to a relaxation of the current again. The point where the trace crosses the intrinsic Fermi level, corresponds to the minimum of current observed in figure 4.4. The lower plot of figure 4.6 depicts this proposed trace. The period where electron transport is dominating is clearly visible and lasts about 3 minutes. In equilibrium, the Fermi energy settles down to similar values irrespective of the gate voltage, which is in accordance with the proposed model in figure 4.5. The observed equilibrium Fermi energy happens to be slightly above 0.2 eV, which fits pretty well to the value found in section 4.1.1, where the Fermi level was estimated by comparing the resistivity of the device with those of doped bulk Ge.

4.1.4 Trapping Time Constants

Since the change in Fermi energy over time is a direct consequence of “effective” gate variations due to the slow redistribution of surface charges, trapping time constants can be estimated by fitting exponential curves into figure 4.6. Although multiexponential time dependence is expected due to the high spread in energy and

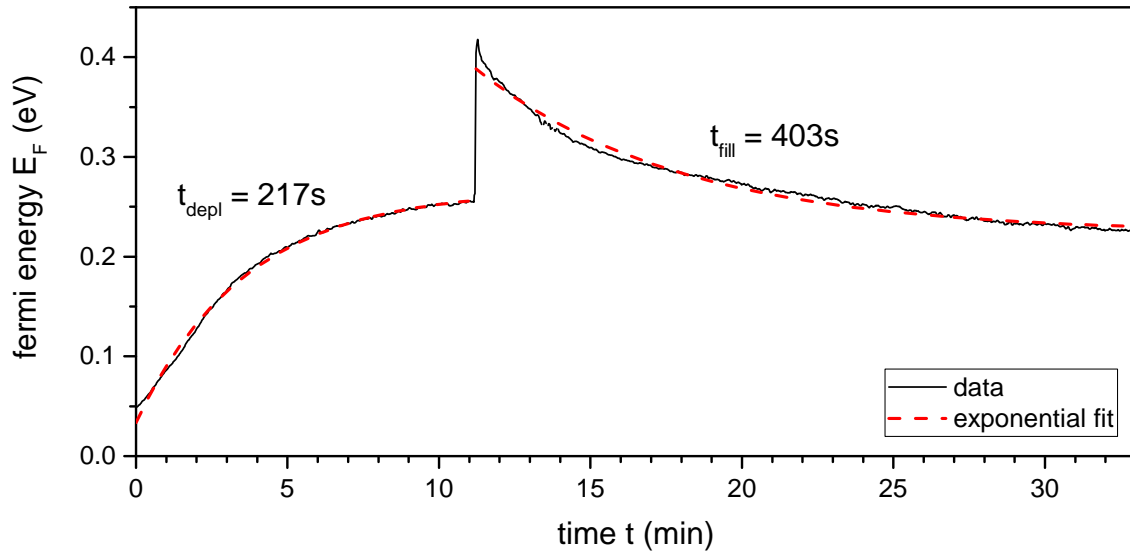


Figure 4.7: Trapping time constants as extracted from figure 4.6 by exponential fitting. The filling of traps takes significantly longer, which can be attributed to the unequal barrier heights for the trapping and detrapping process. Time constants are in the order of several minutes, which corresponds to the trapping times of slow surface states in Ge [85].

spatial distribution of traps [86], a dominant time constant can be found for both the filling and the depletion process. Figure 4.7 depicts these exponential fits along with their characteristic time constants of $t_{depl} = 217$ s and $t_{fill} = 403$ s. Interestingly, the filling of traps seems to be less efficient since the time constant is approximately twice as high. This can be attributed to the different barriers heights for charges going from the semiconductor into the oxide and vice versa. However, the observed time constants are in accordance with trapping times reported in literature [85, 86].

Until now, the effect of trapping has been discussed in terms of an additional gate which adds to the “effective” gate acting on the NW. In a macroscopic point of view it is more common to describe the additional gate by a shift of the threshold voltage V_t of the transistor [125], which is completely equivalent. Thus, instead of stating that the “effective” gate approaches its equilibrium value over time due to the surface charges, it can also be said that the gate stays exactly the same but V_t changes, such that the equilibrium value is reached after a certain time span. Looking at the transfer characteristics, V_t shifts to the left during the depletion and to the right during the filling of traps.

4.1.5 Characterization at Cryogenic Temperatures

Since the trapping and detrapping of electrons in the oxide is a kinetically limited process [86], one would expect the reaction times to increase at lower temperatures. In fact, this is what could be observed in the conducted measurements. Figure 4.8a depicts a measurement where the NW has been cooled down to 80 K at $V_G = 0$ V in equilibrium. After switching the gate voltage to -15 V, the bias current changes to approximately 900 nA where it stays constant for nearly one hour. This indicates that electrons are now efficiently trapped into the oxide, because they have too little thermal energy to tunnel through the energetic barrier. When switching to 15 V, the current changes abruptly to below 100 fA which is already at the noise level of the measurement system. Again, no change in current can be observed, indicating that the thermal energy is not high enough for the filling of traps as well. At 80 K, it therefore comes to a freeze-out of the surface states.

Moreover, at this temperature, an I_{on}/I_{off} ratio of 7 orders of magnitude can be measured. This is much higher than at 300 K, which is a consequence of the Fermi distribution getting steeper at lower temperatures (2.3). By comparing the transfer characteristics at 80 K and 300 K in figure 4.8b, one can see that the transition between on- and off-state starts at a similar gate voltage but happens much faster at lower temperatures.

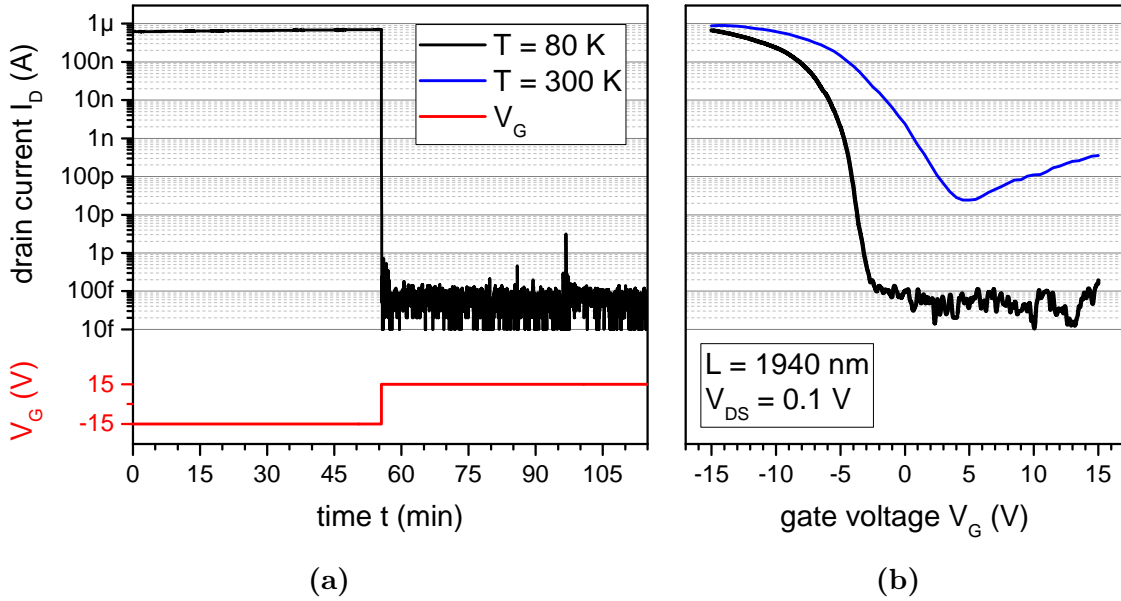


Figure 4.8: (a) Transient behavior for step changes in gate voltage measured at 80 K. The current remains stable at this temperature indicating that the depletion and filling of traps is a thermally limited process. (b) Transfer characteristics at 80 K and 300 K revealing the higher controllability and steeper transitions at lower temperatures.

In order to verify this model, a second experiment is conducted where the following two effects are exploited, which were identified in the previous measurements:

1. Applying gate voltage at room temperature leads to a redistribution of surface charges, which results in a slow shift of threshold voltage over time.
2. Surface traps are frozen out at 80 K, which stabilizes the transfer characteristics at a certain position.

Thus, by applying a certain gate voltage at room temperature and subsequently cooling down to 80 K, one would expect to obtain a stable transistor with tunable threshold voltage. Such a measurement is depicted in figure 4.9. A gate voltage of -15 V is applied at the beginning and traps start to discharge until equilibrium is reached at 900 pA. By comparing this curve with the room temperature transfer characteristic of figure 4.8b, one can see that the equilibrium current corresponds to the value at $V_G = 0$ V. In other words, this process causes a shift of the threshold voltage by 15 V to the left. Temperature is subsequently lowered to 80 K, which causes the current to decrease to approximately 100 fA. This corresponds to a vertical transition from the blue to the black curve in figure 4.8b at $V_G = 0$ V. By switching

to $V_G = 15$ V at this point an abrupt change towards electron conduction is expected, which would correspond to a gate voltage of 30 V in figure 4.8b. However, since the conductivity is reduced at low temperatures only noise can be measured in this case. Using this method, the threshold voltage can be adjusted arbitrarily by applying different gate voltages at the beginning of the measurement.

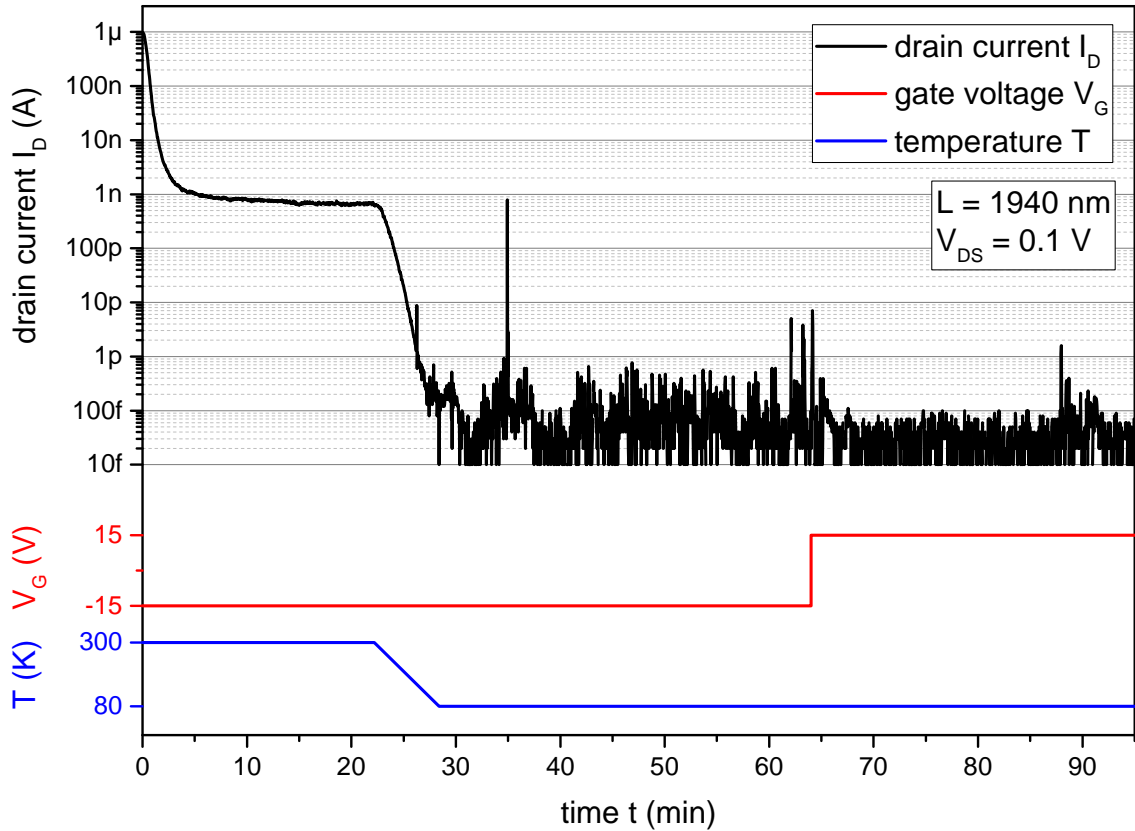


Figure 4.9: Depletion of surface traps at 300 K and $V_G = -15$ V causes a shift of V_t to lower voltages. After cooling down to 80 K, traps are frozen out and V_t is fixed at a certain voltage. Since conductivity is reduced at low temperatures, only noise can be measured in this regime of the transfer characteristics, in contrast to the measurement of figure 4.8 where currents up to $1\mu\text{A}$ were measured.

4.1.6 Negative Differential Resistance

In section 4.1.3, a model is proposed in which the dominant transport mechanism of the Ge NW device can be tuned to be n-type for several minutes by controlling the filling of surface traps. In this regime, Ge NWs under high electrical fields

should exhibit NDR according to previous publications [57]. In fact, this can be observed in various measurements on different NWs. Very nice signatures of NDR were obtained on a device with 920 nm segment length. Measurement results are depicted in figure 4.10.

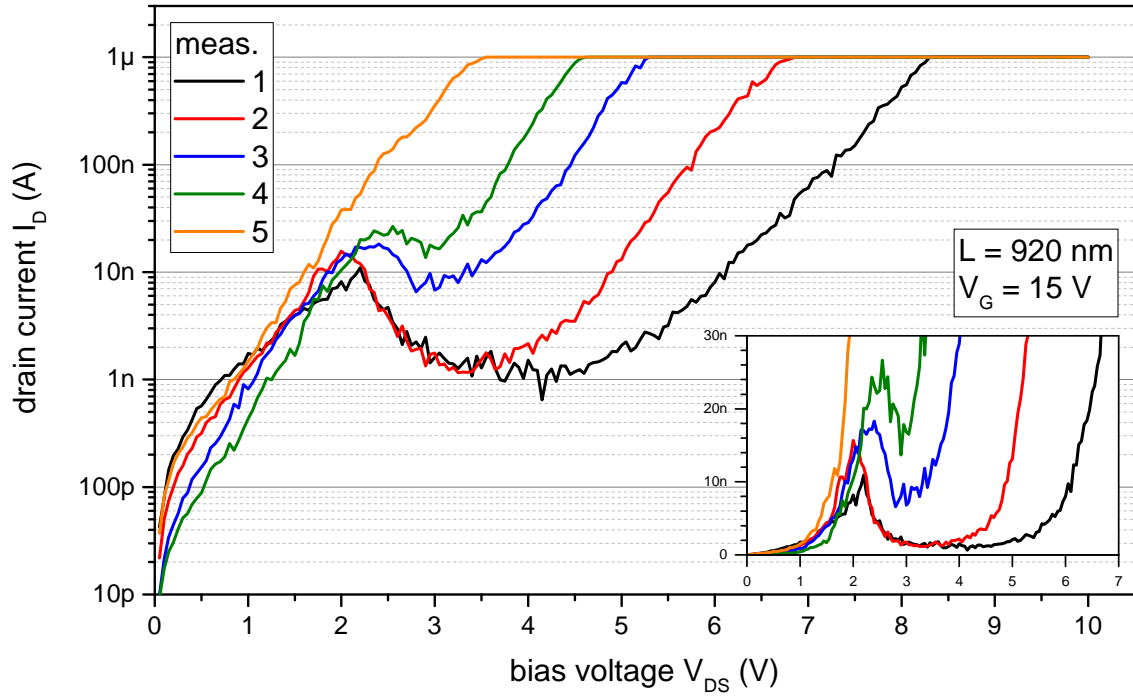


Figure 4.10: I/V curves at $V_G = 15$ V conducted on a Ge NW device with 920 nm segment length measured in intervals of 60 s. $V_G = -15$ V was applied for 20 minutes before the measurement and a current compliance is set to $1 \mu\text{A}$. Clear indications of NDR are visible during the first 4 minutes where the predominantly transport mechanism is n -type. The inset shows a linear representation of the same measurement.

Preliminary to the beginning of the measurement, traps were depleted at $V_G = -15$ V and $V_{DS} = 0.1$ V for approximately 20 minutes. After switching the gate voltage to 15 V, I/V curves are measured from 0 to 10 V bias voltage in intervals of 60 s. A clear signature of NDR is visible in the first 4 measurements which corresponds to a time interval of approximately 4 minutes. This is in accordance with the proposed timespan of electron dominated transport (figure 4.6). The effect of NDR is more pronounced at the beginning of the measurement where a high electron density results also in higher currents at low bias voltages. During the filling of traps, the Fermi level approaches the gap center and less electrons contribute to the transport in the channel. Thus, NDR gets weaker over time until it disappears approximately at the intrinsic point.

4.2 Optical Characterization

As previously discussed in section 2.5.2, surface traps can leverage the photoconducting properties of semiconductors. Low dimensional systems have the benefit of extraordinary high surface to volume ratios and are therefore particularly suited for exploring these effects, which has been demonstrated with great success in various 2D [108, 126], 1D [96, 127], 0D [128] and hybrid systems [107]. In Ge NWs however, only little progress was made during the last years, despite their additional advantage of high surface trap densities and long trapping lifetimes. This can be mainly attributed to the difficult handling concerning longtime drifts due to oxide instabilities and adsorbates. Nevertheless, consequent tuning of the structures with all-around passivation and well-defined atomically sharp contacts revealed their great potential as ultrasensitive photodetectors. In the present work, devices featuring photoconductive gains of more than 10^7 could be established, which is, to the best of my knowledge, the highest ever reported in Ge NWs. It could be further proven that this high gain remains persistent, even when channel lengths are reduced far below the diffraction limit of incident light. This opens the way to photodetectors with high spatial resolution, such as they are required for optical on-chip communication or image sensors [28].

In particular, two observations were made during the conducted electrical measurements, which have the potential to drastically increase the photoresponse of Ge NWs:

1. Surface trapping states in Ge NWs exhibit high densities and long time constants. This prolongs carrier lifetimes in the channel, which can give rise to the photoconductive effect (PC) according to (2.41).
2. Electrons trapped into the oxide act as a local gate which causes a shift of the threshold voltage. According to (2.42) this mechanism is the origin of the so-called photovoltaic (PV) effect.

The combination of both effects can lead to superior photocurrents as will be subsequently discussed in this section. Distinguishing the individual contributions however, remains difficult since they act simultaneously in all measurements. Nevertheless, an explanation will be attempted based on literature research and elaborated experiments.

The same set of devices as for the electrical characterization (table 4.1) is used in order to discuss the results of the optical measurements on the following pages.

4.2.1 I/V Characteristics under Illumination

Before looking on the dynamic response of Ge NWs under laser illumination, I/V measurements are conducted in equilibrium when light is incident on the NW. An exemplary result of the device with 650 nm channel length is depicted in figure 4.11a, measured with and without laser illumination. It can be clearly seen that the drain current drastically increases when laser illumination is turned on. Furthermore, the Schottky contacts seem so have less influence since now a linear dependency is observed. This can be attributed to the fact that light illumination causes the carrier density to increase, which in return narrows the depletion width and therefore the Schottky barriers on the contacts.

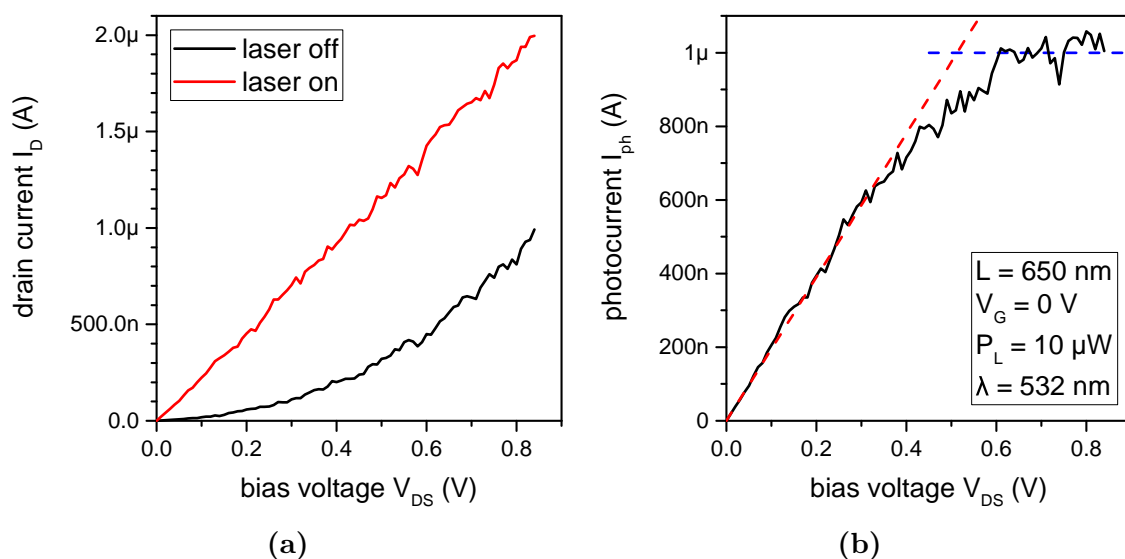


Figure 4.11: (a) I/V characteristics for a Ge NW device with 650 nm channel length with and without laser illumination. The laser power is set to 10 μ W at a wavelength of 532 nm. (b) Photocurrent extracted out of the measurement by subtraction of the two curves in (a). A linear dependence is observed until a certain saturation voltage, which is in accordance with theory of photoconductors.

By taking the difference between these two curves at each point, the photocurrent can be extracted as a function of bias voltage as shown in figure 4.11b. A linear dependency is observed until a bias voltage of about 0.5 V. This is in agreement with theory, since I_{ph} is linearly dependent on the applied electrical field in photoconductors (2.38) and has been observed already for Ge NWs in particular [101]. At a certain bias voltage, the photocurrent saturates at a value of about 1 μ A. For the investigated set of devices this is the case at an electrical field of approximately 10^4 V cm $^{-1}$.

From the I/Vs measured with and without laser illumination, one can calculate the photoinduced resistance change for devices with different channel lengths. Figure 4.12 shows the comparison of this new values along with those of figure 4.2. Again, a linear increase is observed, which is expected in photoconductors. Under illumination, the resistivity decreases from $0.75 \Omega \text{ cm}$ to $0.28 \Omega \text{ cm}$, which corresponds to an I_{on}/I_{off} ratio of about 2.7. Interestingly, this holds also for NW devices with segment lengths of 45 and 85 nm, where the standard model of photoconductors is not sufficient anymore, due to ballistic transport effects in the channel.

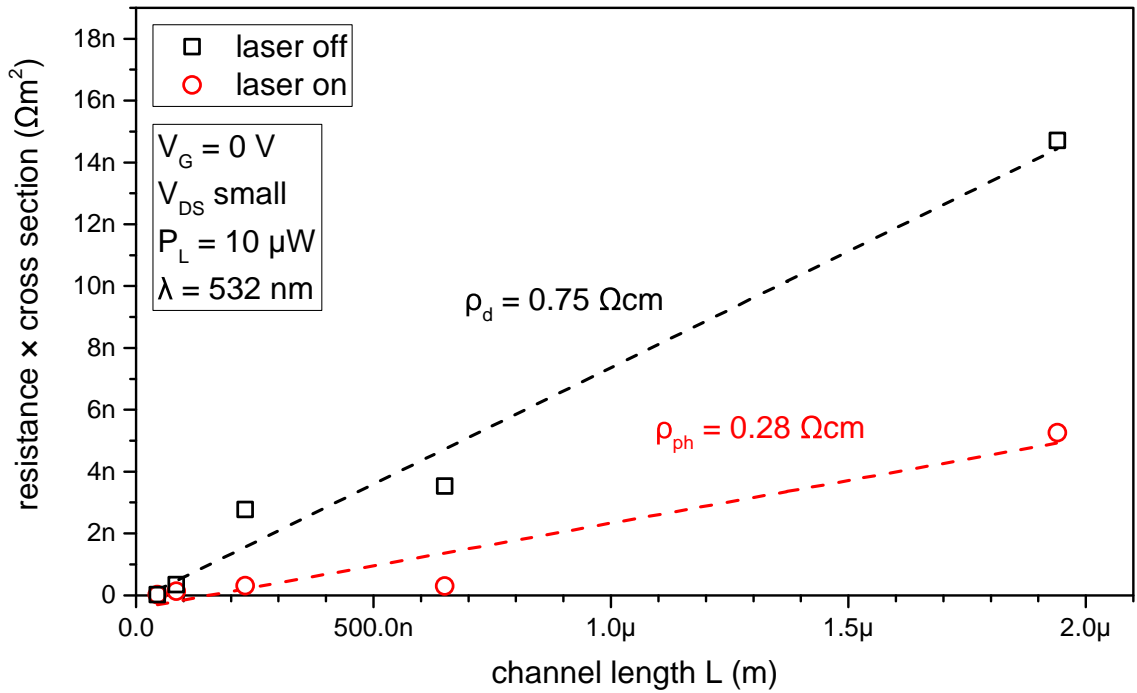


Figure 4.12: Resistance for various channel lengths under dark conditions and laser illumination as extracted from I/V curves by linear fitting near the point of origin. To account for differences in diameter, the resistance is multiplied by the cross-section of the NWs. A linear increase is observed in both cases, which is in accordance with theory. The high photoresponse is quantified by the significant decrease of the resistivity in the channel.

4.2.2 Dynamic Response of the Photocurrent

The two mechanisms leading to high photoconductivity in Ge NWs depend on the trapping of photogenerated electrons into energy states at the surface. Since those traps are generally slow with time constants up to several minutes (compare section 4.1.4), the photoresponse is expected to have a dynamic behavior as well. To

investigate this effect, a strong laser pulse is incident on a NW and the response of I_D is monitored over time. The measurement results are depicted in figure 4.13 for the device with 650 nm channel length. Two different contributions to the photocurrent can be distinguished. The component with timescales below 1 s is referred to as $I_{ph,fast}$. In contrast, $I_{ph,slow}$ happens at timescales reaching up to several minutes.

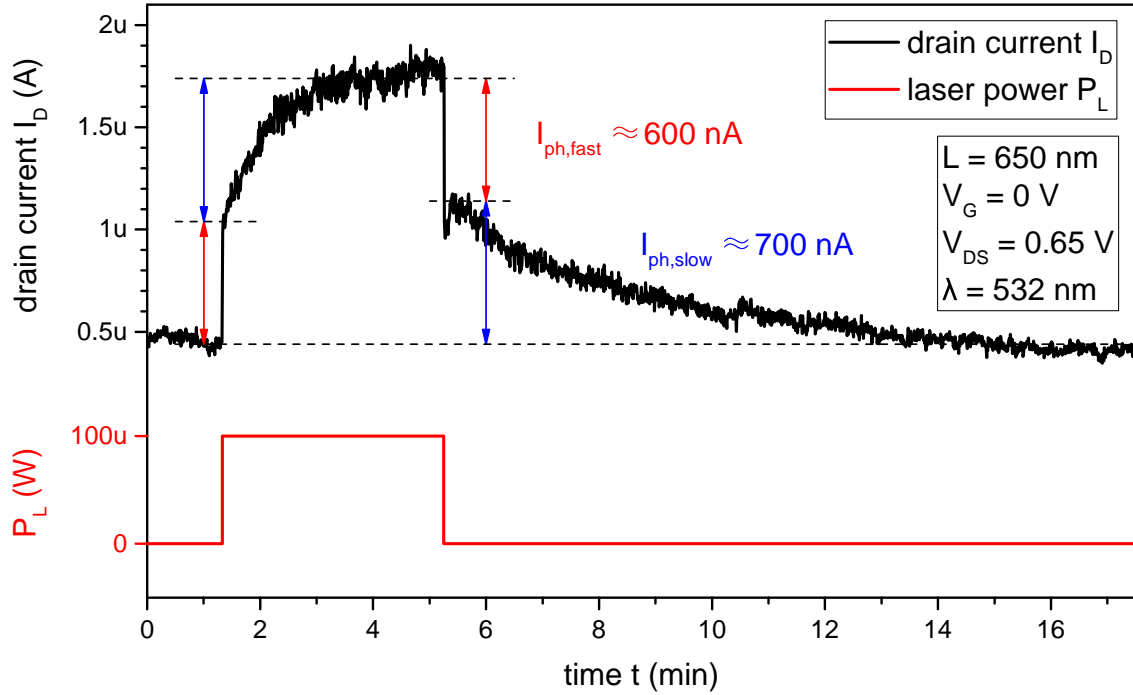


Figure 4.13: Response of I_D for a Ge NW device exposed to a laser pulse. The observed photocurrent can be split into a fast and a slow component. The latter can be explained by the trapping of photogenerated electrons into slow surface states with time constants similar to those observed in the electrical characterization.

It is believed that the slow increase of current under illumination corresponds to the filling of surface traps analogously to section 4.1.3. This assumption is supported by the similar time constants and has been reported by others as well [94, 96, 101, 108]. The illumination with photons exhibiting energies well above the band gap, generates hot electrons in the conduction band. Such electrons are high-energetic and can therefore easily occupy empty surface states in the surrounding oxide, where they act as a local gate. This in return, drastically increases the number of holes in the channel and therefore the conductivity. Macroscopically, this effect corresponds to a photogenerated shift of the threshold voltage to higher values, which is known to be the origin of the PV effect [110]. However, due to the underlying mechanism, it is often referred to as “photogating”.

Although similar time constants as in the electrical characterization are observed, one major difference can be spotted in the results. The filling of traps is now significantly faster, even though the depletion takes approximately the same time as before. This is attributed to the high-energetic electrons, which are able to fill surface traps more efficiently. Once trapped, they lose energy and discharge at equal timescales as in figure 4.4. The illumination with light is therefore a possibility to accelerate charge trapping in Ge NWs.

The origin of $I_{ph,fast}$ is more complicated. Besides the two above mentioned mechanisms, a third effect can contribute to the fast increase of current under illumination. Charge carriers generated due to the internal photoelectrical effect [129] can be extracted directly at the contacts without being trapped in the process. However, since the photoconductive gain of this mechanism is limited to one, its influence on the obtained results is negligible. M. Furchi et al. [108] argued that for atomically thin MoS₂ layers the fast component most probably originates from the PC effect, which they substantiated with the low gate influence in their results. In Ge NWs however, $I_{ph,fast}$ is highly dependent on the “effective” gate, which has been observed in various measurements. Thus, it is believed that charges trapped into faster interface traps contribute to the PV effect as well. Hence, a combination of both mechanisms is observed in the conducted measurements.

Figure 4.14 depicts a similar measurement, but instead of a single pulse, the device is exposed to a chopped laser beam. Although all parameters are equal to figure 4.13, a significantly higher dark current is observed. This can be attributed to the filling of surface traps during the measurement, which causes a shift of V_t towards higher voltages on average. Since the modulation frequency is chosen to be 0.5 Hz in this case, only changes occurring faster than 1 s are visible in the diagram, which corresponds to the fast component of the previous measurement. This manifests also in the amplitude of the photocurrent which is approximately 600 nA in both cases.

The advantage of these measurements with chopped laser is twofold. First, by varying the modulation frequency, conclusions can be drawn on the frequency behavior of the detector and thus the mechanisms involved in the process. Second, and more important, conducting periodical measurements allows for an automatic extraction of the photocurrent by the means of a lock-in amplifier, which is resistant to longterm drifts and noise. This is essential in order to perform reproducible measurements with low signal amplitudes in high-noise environments such as they naturally occur at 300 K. From now on, all further measurements are conducted by using a lock-in amplifier as described in section 3.3.5. For the graph in figure 4.14, the lock-in amplifier estimates a photocurrent of 656 nA, which gives a very good fit to the raw data recorded on an oscilloscope.

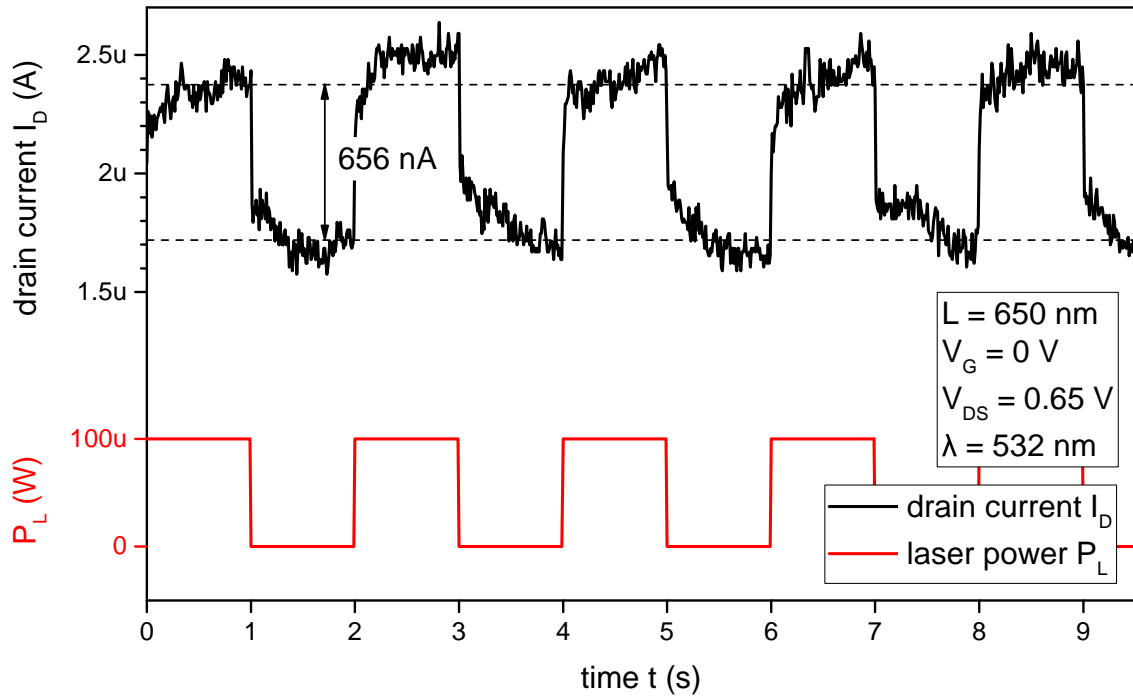


Figure 4.14: Change of drain current over time under periodically excitation with laser light measured by the means of an oscilloscope. The modulation frequency is set to 0.5 Hz at a wavelength of 532 nm and a laser power of 100 μ W.

In order to study the frequency behavior of the devices, measurements are conducted at various modulation frequencies. The obtained results are plotted in figure 4.15 on a logarithmic scale. An additional data point is added, which was extracted out of the single pulse measurement of figure 4.13. Since this is the photocurrent observed in equilibrium, it is the highest measurable value with this detector. The corresponding modulation frequency is estimated to be approximately 2 mHz, since it took 250 s of laser illumination to reach this value. By increasing the modulation frequency, a slight decrease in photocurrent can be observed until approximately 30 Hz, where a plateau is reached which remains stable over 2 orders of magnitude. After that, a steep drop indicates the cut-off frequency of the detector at about 10 kHz.

This behavior can be explained by the proposed trapping model, comprising slow and fast surface states. At low frequencies, the slow oxide traps are dominating, since they exhibit a much higher spatial density than the fast surface states residing directly at the interface (compare figure 2.12b). In equilibrium, which is reached after 250 s, the maximum number of traps are filled and a photocurrent of 1.3 μ A is observed. By increasing modulation frequencies, fewer traps are getting filled during the laser pulse, which results in a weaker “photogating” effect and therefore in less

photocurrent. This decrease continues until a modulation frequency of 30 Hz, which corresponds to a trapping time of roughly 15 ms. Since slow surface states exhibit capture times of milliseconds to minutes [61], it is believed that at this point the second type of surface states becomes dominating.

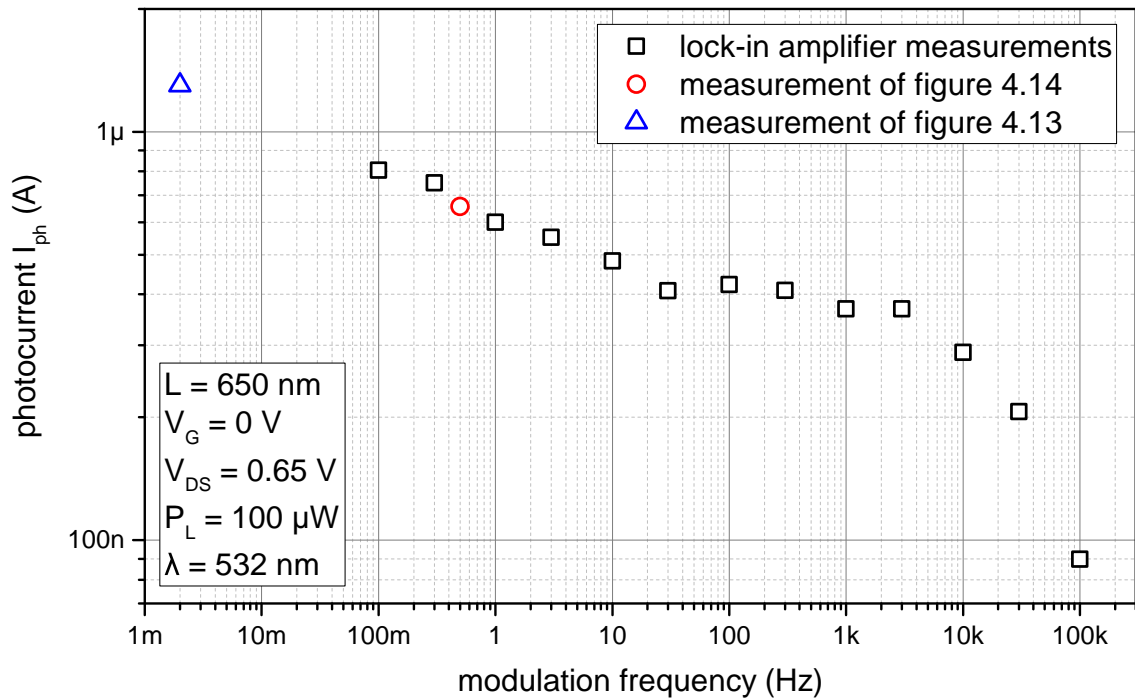


Figure 4.15: Photocurrent vs. modulation frequency for the Ge NW device with 650 nm segment length as measured with a lock-in amplifier. An additional data point (blue triangle) was extracted from the transient measurement in figure 4.13 to show the equilibrium value of the photodetector.

Fast surface traps, on the other hand, exhibit time constants lower than microseconds. Thus, they are easily filled until high modulation frequencies, which results in a constant photoresponse in this regime due to a combination of the PV and PC effect. Eventually, at 10 kHz, which corresponds to a trapping time of 50 μ s, the filling of fast states becomes inefficient as well resulting in a steep decrease of the photocurrent.

4.2.3 Low Power Measurements

It is commonly reported that the efficiency of high gain photoconductors, which rely on the trapping of surface states, is highly dependent on the power of incident

light [101, 104, 106, 113]. This is mainly attributed to the non-linearity of the PV effect (2.42) and trap saturation effects occurring in the PC mechanism. In order to study this phenomena, measurements are conducted in which the power of incident laser light is varied over 4 orders of magnitude. Results for NW devices with different segment lengths are depicted in a logarithmic plot in figure 4.16. According light intensities are calculated by using the peak power of the incident Gaussian laser beam and are indicated at the top of the graph. In this double-logarithmic representation, a straight line corresponds to a power function with the exponent being the slope of the curve.

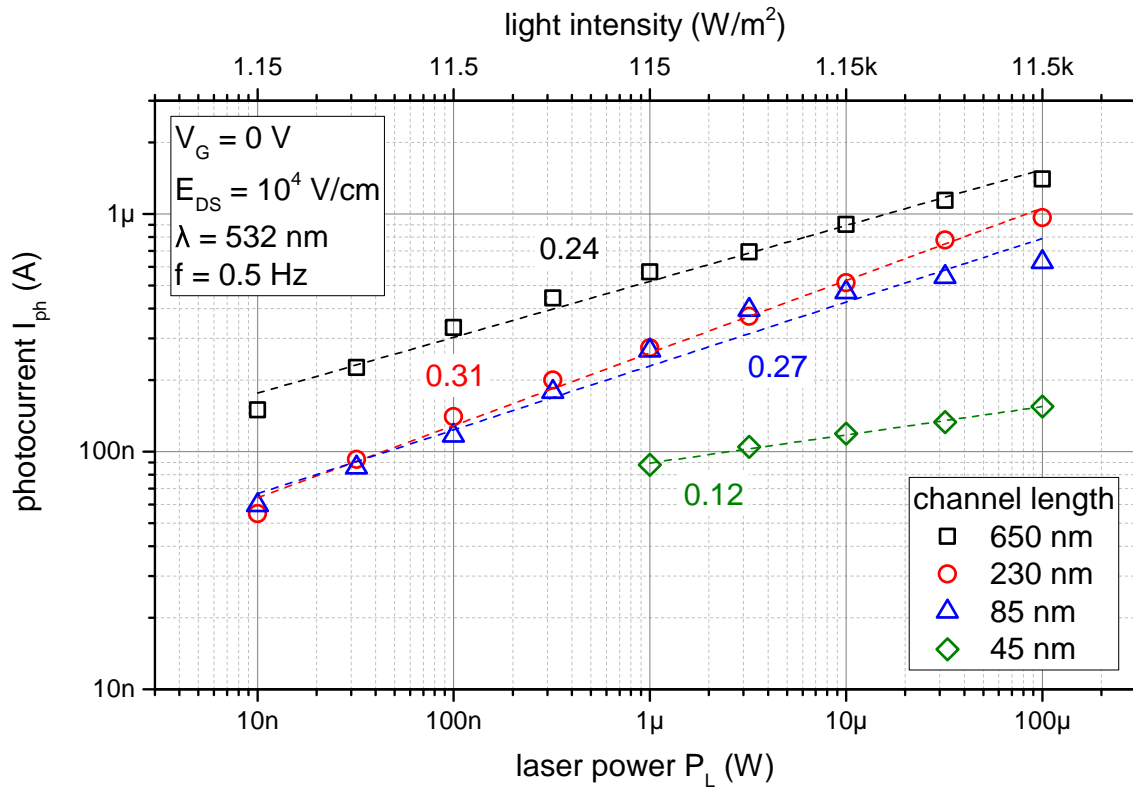


Figure 4.16: Double logarithmic plot of the photocurrent vs. incident laser power for Ge NW devices with segment lengths ranging from 650 nm down to 45 nm. The light intensity is estimated by using the peak power of the Gaussian laser beam. Data is measured at a modulation frequency of 0.5 Hz and the bias voltage was adopted in order to keep the electric field constant at 10^4 V cm^{-1} .

By reducing the incident power of the laser light, a decrease of the photo current can be observed for all NWs. However, for devices with channel length greater than 85 nm, this decrease is not linear but rather a power function with exponents in the

order of 0.2 to 0.3, which is in good agreement with previous publications on intrinsic Ge NWs, where an exponent of 0.29 was found [101]. This sublinear dependency causes the photodetectors to be highly sensitive especially at low excitation, which is a great advantage for detecting light at a high dynamic range. Thus, it is possible to reliably detect light at intensities down to nearly 1 W m^{-2} at room temperature with these devices. This becomes even more astonishing considering their spatial footprints of only about $3 \cdot 10^{-15} \text{ m}^2$.

Interestingly, even though generally less photocurrent is observed for the “ballistic” 45 nm device, it exhibits an even stronger sublinearity. Hence, if this power dependency continues, it is expected to reach similar or even higher photoresponses than the devices featuring larger segment lengths, at very weak excitation. Unfortunately, this could not be measured in the course of this thesis due to the high noise levels at 300 K. The mechanisms leading to high sensitivities in ballistic devices is still under debate. However, others reported similar findings for example in PbS quantum dots [128].

4.2.4 Photoconductive Gain in Germanium Nanowires

In order to quantify the performance of the photodetectors, the photoconductive gain is calculated. Therefore, the optical power absorbed in the NWs is estimated according to (3.11) by neglecting resonance effects like leaky modes or other quantum confinement effects. Subsequently, the gain is calculated by using (3.7) and plotted vs. the number of absorbed photons on a logarithmic plot (figure 4.17).

As expected due to the sublinearity of the photocurrent shown in figure 4.16, the photoconductive gain is strongly dependent on the light intensity of the laser beam. The fewer electrons absorbed, the higher is the efficiency of the photodetectors and the higher is also the observed gain. This is in accordance with literature [112, 113] and commonly modeled by an inverse power law (2.43):

$$g \propto P_{opt}^{-k} \quad (4.4)$$

where k is a fitting parameter, which is approximately 0.72 in the case of the fabricated Ge NW devices.

At low light intensities, photoconductive gains well above 10^7 are observable for devices with longer Ge channel lengths. The highest value measured in the course of this theses is about $5.3 \cdot 10^7$, meaning that for every photon absorbed, more

than 50 million electrons are extracted at the contacts. Furthermore, no saturation effects are observed at low light powers, which indicates that the gain may increase even further when less photons are incident on the NW. During this these it was accomplished to reliably detect an amount of only 7000 photons per seconds at feature sizes well below the diffraction limit of the incident light. Reducing noise by cooling down or using a specialized setup, could further pave the way towards single photon detection in Ge NW devices.

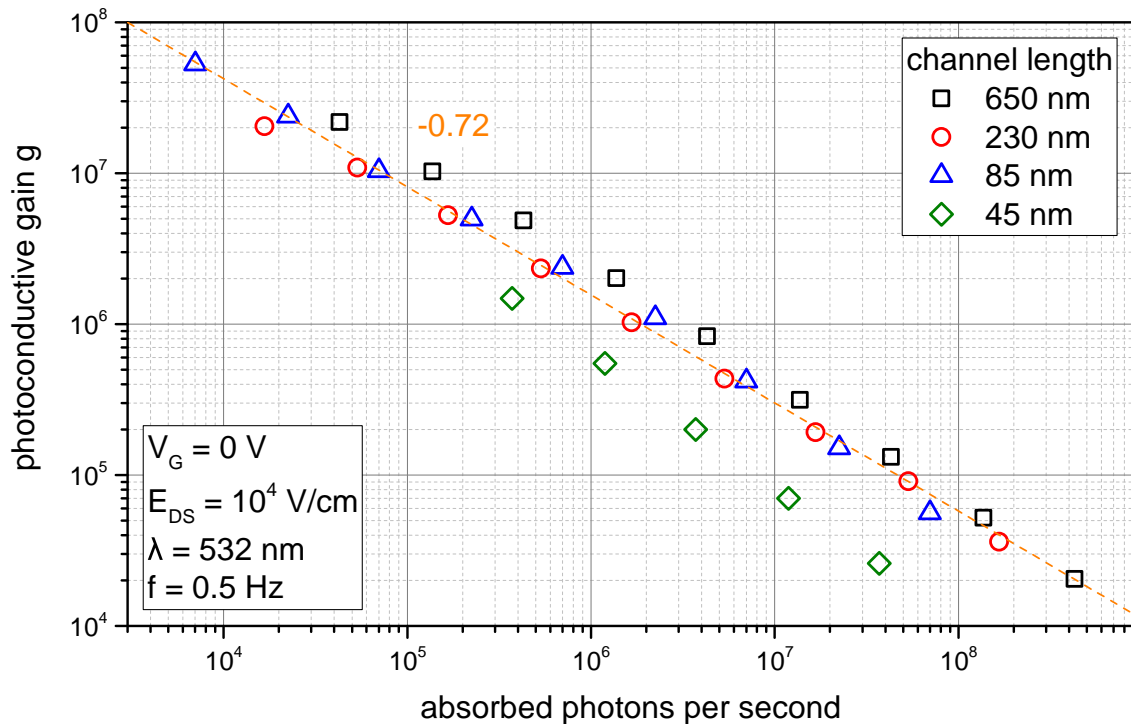


Figure 4.17: Photoconductive gain vs. absorbed photons per second for Ge NW devices with segment lengths ranging from 650 nm down to 45 nm, revealing a gain of more than 10^7 for low light intensities. The measurement data follows an inverse power law indicated by the linear trace in double-logarithmic representation.

Although the 45 nm device seems to be less efficient, it is expected to outperform devices featuring longer channel lengths at very low light intensities. By linear extrapolation of the data in the double-logarithmic plot, a gain of 10^{11} is expected, when only 1 photon per second is incident. This value corresponds to a photocurrent of 16 nA, which should be easily measurable in a low-noise environment. However, since optical experiments were conducted at room temperature only, the highest measurable gain for this detector was $1.5 \cdot 10^6$ at an illumination of approximately $3 \cdot 10^5$ photons per second.

4.2.5 Wavelength Dependent Measurements

As discussed in section 4.1.5, the mechanism of trapping is a thermally activated process. Therefore, in order to occupy empty surface states, electrons need a certain amount of kinetic energy. Such, so-called hot electrons, are generated randomly by thermal excitation due to lattice vibrations at finite temperatures. However, this mechanism is inefficient, which manifests in the long trapping lifetimes found during the electrical characterization. By promoting electrons from the valence band into the conduction band with photons exhibiting energies higher than the band gap of the semiconductor, hot electrons can be generated efficiently. This in return reduces trapping times, which gives rise to the photoconductive gain as it was observed in the previous section.

Measuring the gain as a function of wavelength, enables therefore to study the kinetic barriers of the surface traps in Ge. Such a measurement for the 650 nm

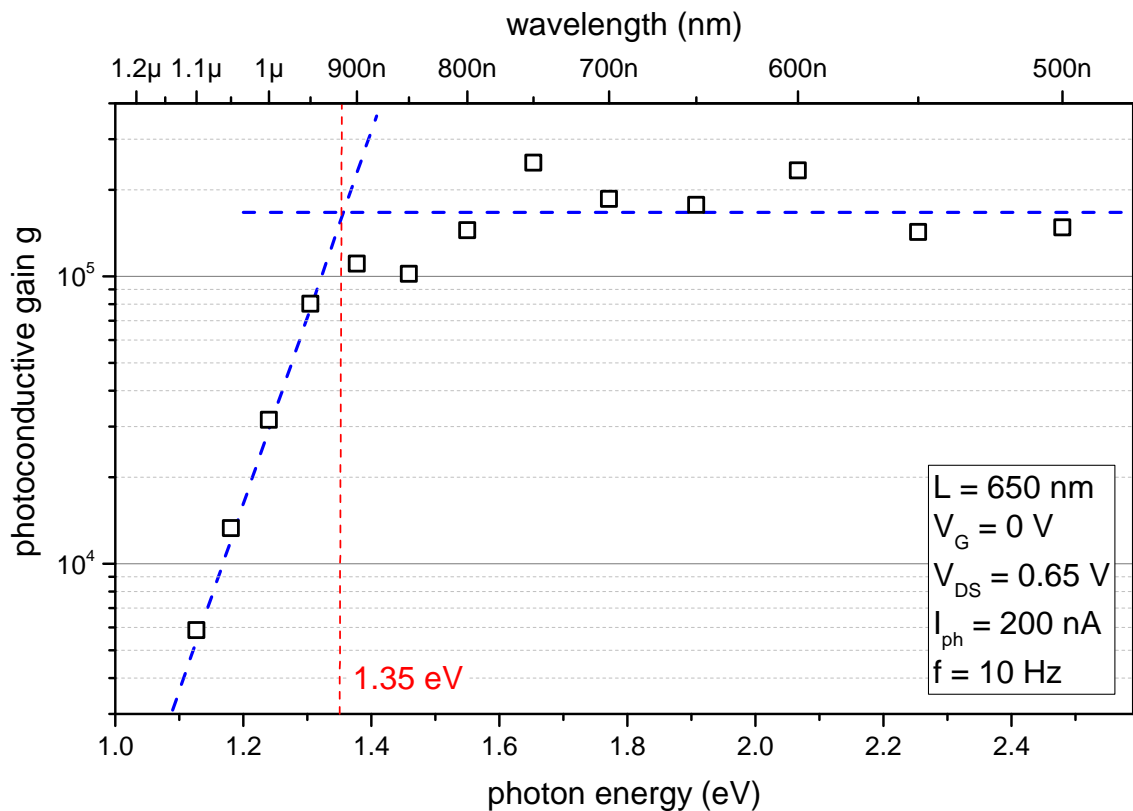


Figure 4.18: Photoconductive gain vs. photon energy for the Ge NW device with 650 nm segment length. The measurement was conducted at constant photocurrent by varying the power of the incident laser.

long Ge NW device is exemplarily depicted in figure 4.18. In order to eliminate influences of saturation or other parasitic effects, the measurement is conducted at constant photocurrent by varying the power of the incident laser during the wavelength sweep. This ensures that in every point the same number of traps is filled and the electrical conditions are equal. Furthermore, the reduced absorption coefficient at higher wavelengths (compare figure 3.9) is considered in the calculation of the gain. Hence, no dependency on the wavelength is expected in this plot, if it is assumed that the generation of hot electrons does not affect the photocurrent. In the measurements however, a strong dependency on the wavelength can be found. While the photoconductive gain remains more or less constant at high photon energies, a steep drop below 1.35 eV is observed. Considering previous observations on the mechanisms leading to high photoconductive gain in Ge NWs, it is believed that this energy corresponds to the trapping barrier of surface states. The existence of a kinetic barrier is in agreement with previous reports on trapping in Ge NWs [86]. However, the study of the barrier height was still outstanding. In this measurement it could be further proven that the fabricated photodetectors cover the whole visible light spectrum at similar sensitivities, which can be exploited for example in high resolution image sensors.

Conclusion and Outlook

In the present work, the device integration of axial Ge NW heterostructures employing monolithic Al contacts was successfully demonstrated. Thereby, devices with defined geometry, atomically sharp interfaces and high- κ passivation were established. By exploiting a thermal induced exchange process, it was further possible to achieve feature sizes without any lithographic restrictions, which allowed for the investigation of ultrashort NW segments and even Ge nanodots. Thus, a comprehensive study of the electrical and electro-optical properties of nanoscale Ge devices could be conducted during the course of this thesis.

The first part was dedicated to the investigation and characterization of surface trapping effects in Ge NWs. Thereby, a strong influence of surface states on the electrical transport was observed, which was attributed to the gating effect of trapped electrons. These filling and depletion processes counteract the external gate, which results in a relatively slow compensation mechanism as monitored in various transient measurements. A model was proposed, which describes most of the observed effects in this work and is consistent with publications of other research groups. Subsequently, a large number of different measurements both electrical and optical were designed and conducted in order to confirm this model. Transfer characteristics showed the predicted p-type behavior, NDR measurements verified the existence of a regime with electron dominated transport and low temperature measurements revealed the proposed kinetic barriers. Clear indications of both fast and slow surface states were found, even though the latter are dominating in the majority of measurements, due to their high spatial density. Although a high spread of trapping energies and

lifetimes is expected, an average time constant could be extracted for the filling and depletion processes.

After a clear understanding of the surface trapping mechanism has been gained, optical experiments were conducted subsequently. A specifically designed setup allowed thereby for the characterization in a wide spectral range and at low power conditions. Transient measurements under laser illumination revealed similar time constants as in the electrical characterization, which indicates photo-enhanced redistribution of surface charges. It could be demonstrated that photogenerated carriers can be efficiently trapped into the oxide due to the absorption of high energetic photons, which was attributed to the kinetic barriers observed earlier. The superior photoresponse was discussed on the basis of two distinct mechanisms and an attempt was given on entangling the individual contributions. Photoconductive gains were shown to critically depend on the power of incident light. At low power conditions, gains exceeding 10^7 were measured, which is, to the best of my knowledge, the highest ever reported in Ge NWs. It could be further proven that the fabricated detectors are sensitive in the whole visible spectral range, which is a great advantage for image sensors.

Operation frequencies up to 10 kHz were demonstrated during the course of this thesis. However, further optimizations towards shorter switching times are still necessary in order to employ them as optical sensors for modern high performance ICs. By shrinking sizes of channel lengths down to 45 nm, it could be proven that this concept is not restricted to classical devices, but remains valid for ballistic transport as well. Here, further investigations are necessary in order to fully understand the underlying mechanisms. However, by combining the trapping concept with confinement effects in quantum dots, an enormous range of applications is conceivable, from photodetectors with practically zero off-state current to LETs and even optical logic gates. This could be achieved by further miniaturization of the structures. Low temperature measurements could enhance the capability of Ge NWs to detect light at even smaller illumination densities and therefore higher photoconductive gain, which could pave the way towards single photon detection.

List of Figures

2.1	Density of states of different nanostructures	4
2.2	VLS growth mechanism for the synthesis of Ge NWs	6
2.3	Crystal structure and energy band structure of Ge	7
2.4	Density of states, Fermi distribution and carrier concentration	9
2.5	Resistivity of Ge as a function of impurity concentration	11
2.6	Energetic position of common impurities in the band gap of Ge	14
2.7	Schematic of possible band-to-impurity transfer processes at an impurity with one energy level	15
2.8	Direct and indirect optical transitions between valence and conduction band	16
2.9	Optical absorption coefficient of Ge as a function of photon energy at 77 K and 300 K	17
2.10	Schematic illustration of the transferred electron effect in Ge	18
2.11	Energy band diagram of an oxide semiconductor interface with a single trap level under applied field	21
2.12	Schematic of a GeO _x /Ge interface with relatively fast surface and slow oxide states along with their lifetimes and concentrations	23
2.13	Band bending mechanism of slightly n-doped Ge with acceptor-like surface states	24
2.14	Cross section and band diagram of an n-doped Ge NW with diameter d and acceptor-like surface states	25
2.15	Schematic of a photoconductor, which consists of a semiconductor connected with two ohmic contacts	27
2.16	Simulated two-dimensional electrostatic field distribution in Ge NWs for different diameters	30
2.17	Absorption efficiency spectra of Ge NWs with various radii along with the wavelength of the leaky modes	32
3.1	Sketch of the device processing steps for the integration of Ge NWs	37

List of Figures

3.2	Illustration of the integration of a fully featured Ge NW device	39
3.3	Schematic illustration of the measurement setup for electrical characterization of individual Ge NWs	40
3.4	Sketch of the optical measurement setup	43
3.5	Schematic illustration of the measurement setup for optical characterization of individual Ge NWs	44
3.6	Photograph of the measurement setup for conducting various optical measurements	45
3.7	Amplification characteristic of a EG&G 7265 Lock-In Amplifier	47
3.8	Beam profile of a 532 nm laser incident on the sample in vertical and horizontal direction	49
3.9	Optical absorption coefficient of Ge as a function of wavelength and absorbance in a Ge NW depending on diameter	50
4.1	I/V characteristics for Ge NWs with various channel lengths at 0 V back-gate voltage	55
4.2	Resistance for various channel lengths as extracted from the I/Vs in figure 4.1	56
4.3	Transfer characteristic of a device with 1940 nm channel length	58
4.4	Transient behavior of a device with 1940 nm channel length for step changes in gate voltage	59
4.5	Proposed mechanism for the transient behavior of I_D at abrupt changes of V_G	61
4.6	Calculated Fermi energy over time with respect to the band edges . . .	63
4.7	Trapping time constants as extracted from figure 4.6 by exponential fitting	64
4.8	Transient behavior for step changes in gate voltage and transfer characteristics at 80 K	66
4.9	Demonstration of the ability of the devices to tune the threshold voltage by applying V_G at room temperature	67
4.10	I/V curves showing clear indications of NDR in the regime with electron dominated transport	68
4.11	I/V characteristics and photocurrent vs. bias voltage for a Ge NW device with 650 nm channel length	70
4.12	Resistance for various channel lengths under dark conditions and laser illumination	71
4.13	Response of I_D for a Ge NW device exposed to a laser pulse	72
4.14	Change of drain current over time under periodically excitation with laser light	74
4.15	Photocurrent vs. modulation frequency for the Ge NW device with 650 nm segment length	75

4.16	Photocurrent vs. incident laser power for Ge NW devices with segment lengths ranging from 650 nm down to 45 nm	76
4.17	Photoconductive gain vs. absorbed photons per second for Ge NW devices with segment lengths ranging from 650 nm down to 45 nm . .	78
4.18	Photoconductive gain vs. photon energy for the Ge NW device with 650 nm segment length	79

List of Tables

2.1	Composition of thermally grown germanium oxide on a Ge(100) surface under atomic oxygen exposure at different oxidation temperatures . .	22
2.2	Figures of merit for photodetectors	28
2.3	Typical values of response time and gain of photodetectors	31
3.1	Applied optical filters of the brand Thorlabs to achieve the respective output laser power on the sample	46
4.1	Physical dimensions of characteristic NW devices investigated within the course of this thesis	54

Appendix

A Device Processing

Substrate Preparation

A 500 μm thick $\langle 100 \rangle$ oriented Si wafer with 100 nm thermally grown SiO_2 on top is used as substrate.

- Cleaving a 15×15 mm sample from the wafer using a diamond scribe
- Ultrasonic cleaning for 120 s at 100 % power in acetone
- Ultrasonic cleaning for 120 s at 100 % power in isopropanol
- Drying with nitrogen
- Baking for 5 min at 110 $^\circ\text{C}$

First Photolithography Step

In the next step the back-gate contacts are patterned using photolithography. A Karl Süss MicroTec MJB3 mask aligner is used featuring an exposure wavelength of 450 nm.

- Drop casting of image reversal photoresist AZ5214 on the sample surface
- Spin coating for 35 s at 9000 RPM with ramp-up constant 2

- Baking for 60 s at 100 °C
- Aligning of mask for back-gate contacts on sample
- UV exposure for 5.5 s at a power of 275 W
- Developing for 35 s in developer AZ726MIF
- Cleaning for 30 s in deionized water (DI)
- Drying with nitrogen

Etching with Hydrofluoric Acid

In order to contact the back-gate contacts SiO_2 is etched in patterned areas using BHF.

- Dipping in BHF (7:1) for 130 s
- Cleaning for 10 s in DI
- Drying with nitrogen
- Stripping of resist by submerging the sample in acetone
- Dipping in isopropanol
- Drying with nitrogen

Second Photolithography Step

In a second photolithography step the isolated contacts are patterned, which are used as source and drain.

- Drop casting of image reversal photoresist AZ5214 on the sample surface
- Spin coating for 35 s at 9000 RPM with ramp-up constant 2

- Baking for 60 s at 100 °C
- Aligning of mask for source and drain contacts on sample
- UV exposure for 4 s at a power of 275 W
- Reversal baking for 60 s at 130 °C
- UV flood exposure for 20 s at a power of 275 W
- Developing for 35 s in developer AZ726MIF
- Cleaning for 30 s in deionized water (DI)
- Drying with nitrogen
- Dipping in BHF (7:1) for 5 s
- Cleaning for 10 s in DI
- Drying with nitrogen

Ti/Au Sputtering and Lift-Off

Subsequently, a 10 nm Ti layer and a 100 nm Au layer are deposited with a VonArdenne LS320 S sputter system by using the following process parameters.

- Pumping sputter system with sample inside to a base pressure of $2 \cdot 10^{-5}$ mbar
- Setting working pressure to $8 \cdot 10^{-3}$ mbar
- Cleaning Ti target by sputtering Ti onto an unused sample holder for 60 s at 100 W
- Deposition of 10 nm Ti by sputtering onto the sample for 60 s at 50 W
- Deposition of 100 nm Au by sputtering onto the sample for 2×60 s at 50 W
- Submerging of sample in acetone

- Ultrasonic cleaning at 80 % power until the excess metal is fully removed
- Dipping in isopropanol
- Drying with nitrogen

Nanowire Deposition onto Sample

In order to transfer NWs from their growth substrate to the measurement module they are dissolved in isopropanol and drop casted onto the sample.

- Cleaving off a small piece of the growth sample
- Submerging in a few drops isopropanol placed in a small plastic container
- Breaking off the NWs by ultrasonic cleaning for 120 s at 30 % power
- Drop-casting 4 μ L of the solution onto the sample
- Carefully drying with nitrogen
- Repeating last two steps until desired NW density is reached

Electron Beam Lithography

EBL was used to contact individual NWs with Al to the existing macroscopic Au pads.

- Scratching off thermally grown SiO_2 at a back-gate contact to provide sufficient connection between the sample and the EBL system
- Placing sample on sample holder and inserting it into working chamber via loadlock
- Aligning of coordinate system and writefield
- Taking SEM images of desired NWs

- Removing sample via loadlock
- Drop casting of PMMA resist AR-P 679.04 on the sample surface
- Spin coating for 35 s at 4000 RPM with ramp-up constant 2
- Baking for 15 min at 170 °C
- Drawing contacts for chosen NWs with various spacing
- Placing sample on sample holder and inserting it into working chamber via loadlock
- Measuring electron beam current with Faraday cup to calculate dwell times
- Aligning of coordinate system and writefield
- Exposure with beam current of 200 pA and a dose of 0.110 pA s
- Removing sample via loadlock
- Developing for 35 s in developer AR 600-56
- Stopping development for 35 s in stopper AR 600-60
- Drying with nitrogen

Nanowire Passivation Removal

To achieve electrical contacts to the NWs their passivation has to be removed first. This is done by etching with BHF and HI.

- Dipping in BHF (7:1) for 20 s
- Cleaning for 10 s in DI
- Cleaning for 30 s under flowing DI
- Drying with nitrogen

- Dipping in HI (14 %) for 5 s
- Cleaning for 10 s in DI
- Cleaning for 30 s under flowing DI
- Drying with nitrogen

Al Sputtering and Lift-Off

Subsequently, a 100 nm Al layer are deposited with a VonArdenne LS320 S sputter system by using the following process parameters.

- Pumping sputter system with sample inside to a base pressure of $2 \cdot 10^{-5}$ mbar
- Setting working pressure to $8 \cdot 10^{-3}$ mbar
- Cleaning Al target by sputtering Al onto an unused sample holder for 2×60 s at 100 W
- Deposition of 100 nm Al by sputtering onto the sample for 4×60 s at 50 W
- Submerging of sample in acetone
- Heating to 55 °C on a heating plate until excess metal can be easily removed by squirting acetone onto it via a syringe
- Dipping in isopropanol
- Drying with nitrogen

Rapid Thermal Annealing

The diffusion of Al into the Ge NWs is achieved by a RTA procedure with following parameters.

- Placing sample on a wafer in RTA oven

- Cooling for 5 s
- Pumping for 120 s to reach a pressure of 2 mbar
- Flushing for 30 s with nitrogen
- Pumping for 120 s to reach a pressure of 2 mbar
- Flushing for 30 s with nitrogen
- Pumping for 120 s to reach a pressure of 2 mbar
- Flushing for 30 s with forming gas
- Heating to 300 °C in forming gas atmosphere at maximal ramping speed
- Heating to 350 °C in forming gas atmosphere using a 50 K s⁻¹ temperature ramp
- Holding temperature at 350 °C for 180 s in forming gas atmosphere
- Cooling to ambient temperature and removing sample

Mounting onto a Microscope Slide and Wire Bonding

After processing the sample, it is mounted onto a glass microscope slide in order to connect it to measurement instruments.

- Cleaning of the microscope slide and PCB with acetone and isopropanol
- Gluing of the PCB onto the microscope slide using epoxy resin
- Soldering of a socket strip onto the PCB
- Gluing of the sample onto the microscope slide using silver conductive paint
- Wire bonding of chosen devices with the PCB using a K&S iBond5000 Wedge Bond Model

B Symbols

Symbol	Description	Unit
a	Lattice constant	\AA
A	Cross section	cm^2
\mathcal{A}	Absorbance	–
c	Speed of light in vacuum	cm s^{-1}
$D(E)$	Density of states	$\text{eV}^{-1} \text{cm}^{-3}$
D^*	Normalized detectivity	$\text{cm}\sqrt{\text{Hz}}/\text{W}$
D_n	Diffusion coefficient for electrons	$\text{cm}^2 \text{s}^{-1}$
D_p	Diffusion coefficient for holes	$\text{cm}^2 \text{s}^{-1}$
D_t	Surface trap level density	$\text{cm}^{-2} \text{eV}^{-1}$
e	Elementary charge	C
e_n	Emission probability for electrons	s^{-1}
E	Energy	eV
\mathbf{E}	Electric field	V cm^{-1}
E_F	Fermi energy	eV
E_C	Bottom edge of conduction band	eV
E_g	Band gap energy	eV
E_t	Trap energy level	eV
E_V	Top edge of valence band	eV
\mathcal{E}	Electric field	V cm^{-1}
f	Frequency	Hz
$f(E)$	Fermi distribution	–
\mathbf{F}	Force	N
g	Gain	–
g_c	Emission rate for electrons	$\text{cm}^{-3} \text{s}^{-1}$
g_m	Transconductance	S
h	Planck constant	J s
\hbar	Reduced planck constant	J s
\mathbf{H}	Magnetic field	A cm^{-1}
I	Current	A
I_d	Dark current	A

Symbol	Description	Unit
I_{noise}	Noise current	A/\sqrt{Hz}
I_p	Primary photo current	A
I_{ph}	Photo current	A
\mathbf{j}	Current density	$A\text{ cm}^{-2}$
\mathbf{j}_n	Electron current density	$A\text{ cm}^{-2}$
\mathbf{j}_p	Hole current density	$A\text{ cm}^{-2}$
k	Wavenumber	cm^{-1}
k_B	Boltzmann constant	J K^{-1}
m^*	Effective mass	kg
n	Electron concentration in the conduction band	cm^{-3}
n_i	Intrinsic carrier concentration	cm^{-3}
N_A	Acceptor doping concentration	cm^{-3}
N_t	Trap concentration	cm^{-3}
N_C	Effective density of states in the conduction band	cm^{-3}
N_D	Donor doping concentration	cm^{-3}
N_V	Effective density of states in the valence band	cm^{-3}
NEP	Noise equivalent power	W/\sqrt{Hz}
\mathcal{O}	Overlap (of NW with Laser beam)	–
p	Hole concentration in the valence band	cm^{-3}
P_L	Laser power	W
P_{opt}	Absorbed optical power	W
Q_t	Surface trap charge density	C cm^{-2}
r_c	Capture rate for electrons	$\text{cm}^{-3}\text{ s}^{-1}$
r_{diff}	Differential resistance	Ω
R	Resistance	Ω
t	Time	s
t_n	Transit time for electrons	s
t_p	Transit time for holes	s
T	Temperature	K
T_{OX}	Oxidation temperature	K
\mathcal{T}	Transmittance	–
\mathbf{v}	Velocity	cm s^{-1}

Appendix

Symbol	Description	Unit
v_{th}	Thermal velocity	cm s^{-1}
V	Voltage	V
V_t	Threshold voltage	V
α	Optical absorption coefficient	cm^{-1}
ε	Permittivity	F cm^{-1}
ε_0	Permittivity of vacuum	F cm^{-1}
η	Quantum efficiency	–
κ_0	Tunneling decay constant	cm^{-1}
λ	Wavelength	nm
μ	Carrier mobility	$\text{cm}^2 \text{V}^{-1} \text{s}^{-1}$
μ_n	Electron mobility	$\text{cm}^2 \text{V}^{-1} \text{s}^{-1}$
μ_p	Hole mobility	$\text{cm}^2 \text{V}^{-1} \text{s}^{-1}$
ν	Frequency of light	Hz
ρ	Resistivity	$\Omega \text{ cm}$
σ	Standard distribution	cm
σ	Conductivity	S cm^{-1}
σ_i	Intrinsic Conductivity	S cm^{-1}
σ_n	Capture cross section for electrons	cm^2
τ	Average relaxation time of a scattering event	s
τ	Carrier lifetime	s
τ_n	Carrier lifetime for electrons	s
τ_p	Carrier lifetime for holes	s
τ_t	Trap lifetime	s
φ	Phase	rad
Φ_s	Surface potential	V
ω	Angular frequency	rad s^{-1}

C Abbreviations

Symbol	Description
ALD	Atomic Layer Deposition
AOTF	Acousto-Optical Tunable Filter
BHF	Buffered Hydrofluoric Acid
CCD	Charge Coupled Device
CMOS	Complementary Metal Oxide Semiconductor
CNL	Charge Neutrality Level
CVD	Chemical Vapor Deposition
EBL	Electron Beam Lithography
EDS	Energy-Dispersive X-ray Spectroscopy
fcc	Face-Centered Cubic
FET	Field Effect Transistor
FIB	Focused Ion Beam
FWHM	Full Width at Half Maximum
GPIO	General Purpose Interface Bus
IC	Integrated Circuit
IR	Infrared
JLFET	Junctionless Field Effect Transistor
LED	Light Emitting Diode
LET	Light Effect Transistor
LMR	Leaky Mode Resonance
MOSFET	Metal Oxide Semiconductor Field Effect Transistor
NDR	Negative Differential Resistance
NIR	Near Infrared
NW	Nanowire
PC	Photoconductive
PCB	Printed Circuit Board
PMMA	Polymethylmethacrylat
PV	Photovoltaic
RTA	Rapid Thermal Annealing
SEM	Scanning Electron Microscopy

Appendix

Symbol	Description
SMU	Source Measure Unit
SRH	Shockley-Read-Hall
TE	Transverse Electric
TM	Transverse Magnetic
UV	Ultraviolet
VIS	Visible
VLS	Vapor Liquid Solid

References

- [1] G. E. Moore. Cramming more components onto integrated circuits, Reprinted from *Electronics*, volume 38, number 8, April 19, 1965, pp.114 ff. *IEEE Solid-State Circuits Newsletter*, 20(3):33–35, 2006. ISSN 1098-4232. doi: 10.1109/N-SSC.2006.4785860.
- [2] A. A. Chien and V. Karamcheti. Moore’s Law: The First Ending and a New Beginning. *Computer*, 46(12):48–53, 2013. ISSN 0018-9162. doi: 10.1109/MC.2013.431.
- [3] J. M. Shalf and R. Leland. Computing beyond Moore’s Law. *Computer*, 48(12):14–23, 2015. ISSN 0018-9162. doi: 10.1109/MC.2015.374.
- [4] T. Ghani, M. Armstrong, C. Auth, M. Bost, P. Charvat, G. Glass, T. Hoffmann, K. Johnson, C. Kenyon, J. Klaus, B. McIntyre, K. Mistry, A. Murthy, J. Sandford, M. Silberstein, S. Sivakumar, P. Smith, K. Zawadzki, S. Thompson, and M. Bohr. A 90nm high volume manufacturing logic technology featuring novel 45nm gate length strained silicon CMOS transistors. In *IEEE International Electron Devices Meeting 2003*, pages 11.6.1–11.6.3. IEEE, 2003. ISBN 0-7803-7872-5. doi: 10.1109/IEDM.2003.1269442.
- [5] K. Mistry, C. Allen, C. Auth, B. Beattie, D. Bergstrom, M. Bost, M. Brazier, M. Buehler, A. Cappellani, R. Chau, C.-H. Choi, G. Ding, K. Fischer, T. Ghani, R. Grover, W. Han, D. Hanken, M. Hattendorf, J. He, J. Hicks, R. Huessner, D. Ingerly, P. Jain, R. James, L. Jong, S. Joshi, C. Kenyon, K. Kuhn, K. Lee, H. Liu, J. Maiz, B. McIntyre, P. Moon, J. Neiryneck, S. Pae, C. Parker, D. Parsons, C. Prasad, L. Pipes, M. Prince, P. Ranade, T. Reynolds, J. Sandford, L. Shifren, J. Sebastian, J. Seiple, D. Simon, S. Sivakumar, P. Smith, C. Thomas, T. Troeger, P. Vandervoorn, S. Williams, and K. Zawadzki. A 45nm Logic Technology with High-k+Metal Gate Transistors, Strained Silicon, 9 Cu Interconnect Layers, 193nm Dry Patterning, and 100% Pb-free Packaging.

- In *2007 IEEE International Electron Devices Meeting*, pages 247–250. IEEE, 2007. ISBN 978-1-4244-1507-6. doi: 10.1109/IEDM.2007.4418914.
- [6] C. Auth, C. Allen, A. Blattner, D. Bergstrom, M. Brazier, M. Bost, M. Buehler, V. Chikarmane, T. Ghani, T. Glassman, R. Grover, W. Han, D. Hanken, M. Hattendorf, P. Hentges, R. Heussner, J. Hicks, D. Ingerly, P. Jain, S. Jaloviar, R. James, D. Jones, J. Jopling, S. Joshi, C. Kenyon, H. Liu, R. McFadden, B. McIntyre, J. Neiryneck, C. Parker, L. Pipes, I. Post, S. Pradhan, M. Prince, S. Ramey, T. Reynolds, J. Roesler, J. Sandford, J. Seiple, P. Smith, C. Thomas, D. Towner, T. Troeger, C. Weber, P. Yashar, K. Zawadzki, and K. Mistry. A 22nm high performance and low-power CMOS technology featuring fully-depleted tri-gate transistors, self-aligned contacts and high density MIM capacitors. In *2012 Symposium on VLSI Technology (VLSIT)*, pages 131–132. IEEE, 2012. ISBN 978-1-4673-0847-2. doi: 10.1109/VLSIT.2012.6242496.
- [7] G. Chen, H. Chen, M. Haurylau, N. A. Nelson, D. H. Albonese, P. M. Fauchet, and E. G. Friedman. Predictions of CMOS compatible on-chip optical interconnect. *Integration, the VLSI Journal*, 40(4):434–446, 2007. ISSN 01679260. doi: 10.1016/j.vlsi.2006.10.001.
- [8] J.D. Meindl. Beyond Moore’s Law: the interconnect era. *Computing in Science & Engineering*, 5(1):20–24, 2003. ISSN 1521-9615. doi: 10.1109/MCISE.2003.1166548.
- [9] M. J. Kobrinsky, B. A. Block, J. F. Zheng, B. C. Barnett, E. Mohammed, M. Reshotko, F. Robertson, S. List, I. Young, and K. Cadien. On-Chip Optical Interconnects. *Intel Technology Journal*, 8(2):129–141, 2004.
- [10] G. Chen, H. Chen, M. Haurylau, N. Nelson, D. Albonese, P. M. Fauchet, and E. G. Friedman. Electrical and Optical On-Chip Interconnects in Scaled Microprocessors. In *2005 IEEE International Symposium on Circuits and Systems*, pages 2514–2517. IEEE, 2005. ISBN 0-7803-8834-8. doi: 10.1109/ISCAS.2005.1465137.
- [11] M. Haurylau, G. Chen, H. Chen, J. Zhang, N. A. Nelson, D. H. Albonese, E. G. Friedman, and P. M. Fauchet. On-chip optical interconnect roadmap: challenges and critical directions. *IEEE International Conference on Group IV Photonics, 2005. @nd*, 12(6):17–19, 2006. doi: 10.1109/GROUP4.2005.1516388.
- [12] A. L. Pyayt, B. Wiley, Y. Xia, A. Chen, and L. Dalton. Integration of photonic and silver nanowire plasmonic waveguides. *Nature Nanotechnology*, 3(11):660–665, 2008. ISSN 1748-3387. doi: 10.1038/nnano.2008.281.
- [13] J. A. Dionne, L. A. Sweatlock, M. T. Sheldon, A. P. Alivisatos, and H. A. Atwater. Silicon-Based Plasmonics for On-Chip Photonics. *IEEE Journal of*

-
- Selected Topics in Quantum Electronics*, 16(1):295–306, 2010. ISSN 1077-260X. doi: 10.1109/JSTQE.2009.2034983.
- [14] J. T. Kim. CMOS-Compatible Hybrid Plasmonic Waveguide for Subwavelength Light Confinement and On-Chip Integration. *IEEE Photonics Technology Letters*, 23(4):206–208, 2011. ISSN 1041-1135. doi: 10.1109/LPT.2010.2096805.
- [15] R. Yan, D. Gargas, and P. Yang. Nanowire photonics. *Nature Photonics*, 3(10):569–576, 2009. ISSN 1749-4885. doi: 10.1038/nphoton.2009.184.
- [16] G. Konstantatos and E. H. Sargent. Nanostructured materials for photon detection. *Nature Nanotechnology*, 5(6):391–400, 2010. ISSN 1748-3387. doi: 10.1038/nnano.2010.78.
- [17] M. D. Brubaker, P. T. Blanchard, J. B. Schlager, A. W. Sanders, A. Roshko, S. M. Duff, J. M. Gray, V. M. Bright, N. A. Sanford, and K. A. Bertness. On-Chip Optical Interconnects Made with Gallium Nitride Nanowires. *Nano Letters*, 13(2):374–377, 2013. ISSN 1530-6984. doi: 10.1021/nl303510h.
- [18] D. Dai and J. E. Bowers. Silicon-based on-chip multiplexing technologies and devices for Peta-bit optical interconnects. *Nanophotonics*, 3(4-5):283–311, 2014. ISSN 2192-8614. doi: 10.1515/nanoph-2013-0021.
- [19] K. Liu, N. Li, D. K. Sadana, and V. J. Sorger. Integrated Nanocavity Plasmon Light Sources for On-Chip Optical Interconnects. *ACS Photonics*, 3(2):233–242, 2016. ISSN 2330-4022. doi: 10.1021/acsp Photonics.5b00476.
- [20] P. Chaisakul, D. Marris-Morini, J. Frigerio, D. Chrastina, M. S. Rouifed, S. Cecchi, P. Crozat, G. Isella, and L. Vivien. Integrated germanium optical interconnects on silicon substrates. *Nature Photonics*, 8(6):482–488, 2014. ISSN 1749-4885. doi: 10.1038/nphoton.2014.73.
- [21] C. Buwen, L. Cheng, L. Zhi, and X. Chunlai. Research progress of Si-based germanium materials and devices. *Journal of Semiconductors*, 37(8):081001, 2016. ISSN 1674-4926. doi: 10.1088/1674-4926/37/8/081001.
- [22] M. J. Süess, R. Geiger, R. A. Minamisawa, G. Schiefler, J. Frigerio, D. Chrastina, G. Isella, R. Spolenak, J. Faist, and H. Sigg. Analysis of enhanced light emission from highly strained germanium microbridges. *Nature Photonics*, 7(6):466–472, 2013. ISSN 1749-4885. doi: 10.1038/nphoton.2013.67.
- [23] S. Wirths, R. Geiger, N. von den Driesch, G. Mussler, T. Stoica, S. Mantl, Z. Ikonic, M. Luysberg, S. Chiussi, J. M. Hartmann, H. Sigg, J. Faist, D. Buca, and D. Grützmacher. Lasing in direct-bandgap GeSn alloy grown on Si. *Nature Photonics*, 9(2):88–92, 2015. ISSN 1749-4885. doi: 10.1038/nphoton.2014.321.

- [24] S. Assefa, F. Xia, and Y. A. Vlasov. Reinventing germanium avalanche photodetector for nanophotonic on-chip optical interconnects. *Nature*, 464(7285):80–84, 2010. ISSN 0028-0836. doi: 10.1038/nature08813.
- [25] S. Kral, C. Zeiner, M. Stöger-Pollach, E. Bertagnolli, M. I. den Hertog, M. Lopez-Haro, E. Robin, K. El Hajraoui, and A. Lugstein. Abrupt Schottky Junctions in Al/Ge Nanowire Heterostructures. *Nano Letters*, 15(7):4783–4787, 2015. ISSN 1530-6984. doi: 10.1021/acs.nanolett.5b01748.
- [26] M. Sistani. *Ballistic Transport Phenomena in Al-Ge-Al Nanowire Heterostructures*. Master’s thesis, TU Wien, 2016.
- [27] R. H. Hadfield. Single-photon detectors for optical quantum information applications. *Nature Photonics*, 3(12):696–705, 2009. ISSN 1749-4885. doi: 10.1038/nphoton.2009.230.
- [28] C. Soci, A. Zhang, X. Y. Bao, H. Kim, Y. Lo, and D. Wang. Nanowire Photodetectors. *Journal of Nanoscience and Nanotechnology*, 10(3):1430–1449, 2010. ISSN 15334880. doi: 10.1166/jnn.2010.2157.
- [29] J. K. Marmon, S. C. Rai, K. Wang, W. Zhou, and Y. Zhang. Light-Effect Transistor (LET) with Multiple Independent Gating Controls for Optical Logic Gates and Optical Amplification. *arXiv preprint arXiv:1601.04748*, 2016.
- [30] D. A. B. Miller. Are optical transistors the logical next step? *Nature Photonics*, 4(1):3–5, 2010. ISSN 1749-4885. doi: 10.1038/nphoton.2009.240.
- [31] D. Woods and T. J. Naughton. Optical computing: Photonic neural networks. *Nature Physics*, 8(4):257–259, 2012. ISSN 1745-2473. doi: 10.1038/nphys2283.
- [32] K. D. Sattler. *Handbook of Nanophysics: Nanotubes and Nanowires*. CRC Press, 2010. ISBN 978-1-4200-7542-7.
- [33] G. Chen and A. Shakouri. Heat Transfer in Nanostructures for Solid-State Energy Conversion. *Journal of Heat Transfer*, 124(2):242, 2002. ISSN 00221481. doi: 10.1115/1.1448331.
- [34] L. Zhuang, L. Guo, and S. Y. Chou. Silicon single-electron quantum-dot transistor switch operating at room temperature. *Applied Physics Letters*, 72(10):1205, 1998. ISSN 00036951. doi: 10.1063/1.121014.
- [35] P. Yang, R. Yan, and M. Fardy. Semiconductor Nanowire: What’s Next? *Nano Letters*, 10(5):1529–1536, 2010. ISSN 1530-6984. doi: 10.1021/nl100665r.
- [36] N. Singh, A. Agarwal, L. K. Bera, T. Y. Liow, R. Yang, S. C. Rustagi, C. H. Tung, R. Kumar, G. Q. Lo, N. Balasubramanian, and D. L. Kwong. High-

-
- performance fully depleted silicon nanowire (diameter ≤ 5 nm) gate-all-around CMOS devices. *Electron Device Letters, IEEE*, 27(5):383–386, 2006.
- [37] K. M. Rosfjord, J. K. W. Yang, E. A. Dauler, A. J. Kerman, V. Anant, B. M. Voronov, G. N. Gol'tsman, and K. K. Berggren. Nanowire single-photon detector with an integrated optical cavity and anti-reflection coating. *Optics Express*, 14(2):527, 2006. ISSN 1094-4087. doi: 10.1364/OPEX.14.000527.
- [38] E. C. Garnett, M. L. Brongersma, Y. Cui, and M. D. McGehee. Nanowire Solar Cells. *Annual Review of Materials Research*, 41(1):269–295, 2011. ISSN 1531-7331. doi: 10.1146/annurev-matsci-062910-100434.
- [39] C. K. Chan, H. Peng, G. Liu, K. McIlwrath, X. F. Zhang, R. A. Huggins, and Y. Cui. High-performance lithium battery anodes using silicon nanowires. *Nature Nanotechnology*, 3(1):31–35, 2008. ISSN 1748-3387. doi: 10.1038/nnano.2007.411.
- [40] R. G. Hobbs, N. Petkov, and J. D. Holmes. Semiconductor Nanowire Fabrication by Bottom-Up and Top-Down Paradigms. *Chemistry of Materials*, 24(11):1975–1991, 2012. ISSN 0897-4756. doi: 10.1021/cm300570n.
- [41] D. P. Yu, Y. J. Xing, Q. L. Hang, H. F. Yan, J. Xu, Z. H. Xi, and S. Q. Feng. Controlled growth of oriented amorphous silicon nanowires via a solid–liquid–solid (SLS) mechanism. *Physica E: Low-dimensional Systems and Nanostructures*, 9(2):305–309, 2001. ISSN 13869477. doi: 10.1016/S1386-9477(00)00202-2.
- [42] H. Yu and W. E. Buhro. Solution–Liquid–Solid Growth of Soluble GaAs Nanowires. *Advanced Materials*, 15(5):416–419, 2003. ISSN 09359648. doi: 10.1002/adma.200390096.
- [43] R. S. Wagner and W. C. Ellis. Vapor-Liquid-Solid Mechanism of Single Crystal Growth. *Applied Physics Letters*, 4(5):89, 1964. ISSN 00036951. doi: 10.1063/1.1753975.
- [44] J. Westwater, D. P. Gosain, S. Tomiya, S. Usui, and H. Ruda. Growth of silicon nanowires via gold/silane vapor–liquid–solid reaction. *Journal of Vacuum Science & Technology B: Microelectronics and Nanometer Structures*, 15(3):554, 1997. ISSN 0734211X. doi: 10.1116/1.589291.
- [45] G. Gu, M. Burghard, G. T. Kim, G. S. Düsberg, P. W. Chiu, V. Krstic, S. Roth, and W. Q. Han. Growth and electrical transport of germanium nanowires. *Journal of Applied Physics*, 90(11):5747, 2001. ISSN 00218979. doi: 10.1063/1.1413495.
- [46] J. H. Paek, T. Nishiwaki, M. Yamaguchi, and N. Sawaki. Catalyst free MBE-

- VLS growth of GaAs nanowires on (111)Si substrate. *physica status solidi (c)*, 5(9):2740–2742, 2008. ISSN 16101634. doi: 10.1002/pssc.200779248.
- [47] P. Yang, H. Yan, S. Mao, R. Russo, J. Johnson, R. Saykally, N. Morris, J. Pham, R. He, and H. J. Choi. Controlled Growth of ZnO Nanowires and Their Optical Properties. *Advanced Functional Materials*, 12(5):323, 2002. ISSN 1616301X. doi: 10.1002/1616-3028(20020517)12:5<323::AID-ADFM323>3.0.CO;2-G.
- [48] E. Koren, J. K. Hyun, U. Givan, E. R. Hemesath, L. J. Lauhon, and Y. Rosenwaks. Obtaining Uniform Dopant Distributions in VLS-Grown Si Nanowires. *Nano Letters*, 11(1):183–187, 2011. ISSN 1530-6984. doi: 10.1021/nl103363c.
- [49] T. E. Clark, P. Nimmatoori, K. K. Lew, L. Pan, J. M. Redwing, and E. C. Dickey. Diameter Dependent Growth Rate and Interfacial Abruptness in Vapor-Liquid-Solid Si/Si(1-x) Ge(x) Heterostructure Nanowires. *Nano Letters*, 8(4):1246–1252, 2008. ISSN 1530-6984. doi: 10.1021/nl072849k.
- [50] L. J. Lauhon, M. S. Gudiksen, D. Wang, and C. M. Lieber. Epitaxial core-shell and core-multishell nanowire heterostructures. *Nature*, 420(6911):57–61, 2002. ISSN 0028-0836. doi: 10.1038/nature01141.
- [51] T. Hanrath and B. A. Korgel. Nucleation and Growth of Germanium Nanowires Seeded by Organic Monolayer-Coated Gold Nanocrystals. *Journal of the American Chemical Society*, 124(7):1424–1429, 2002. ISSN 0002-7863. doi: 10.1021/ja016788i.
- [52] M. S. Gudiksen, J. Wang, and C. M. Lieber. Synthetic Control of the Diameter and Length of Single Crystal Semiconductor Nanowires. *The Journal of Physical Chemistry B*, 105(19):4062–4064, 2001. ISSN 1520-6106. doi: 10.1021/jp010540y.
- [53] H. C. A. Winkler. Mittheilungen über das Germanium. *Journal für Praktische Chemie*, 34(1):177–229, 1886.
- [54] W. Martienssen and H. Warlimont. *Springer Handbook of Condensed Matter and Materials Data*. Springer Handbook of Condensed Matter and Materials Data. Springer, 2005. ISBN 3-540-44376-2.
- [55] W. C. Dash and R. Newman. Intrinsic optical absorption in single-crystal germanium and silicon at 77 K and 300 K. *Physical Review*, 99(4):1151–1155, 1955.
- [56] H. Tahini, A. Chroneos, R. W. Grimes, U. Schwingenschlögl, and A. Dimoulas. Strain-induced changes to the electronic structure of germanium. *Journal of Physics: Condensed Matter*, 24(19):195802, 2012. ISSN 0953-8984. doi: 10.1088/0953-8984/24/19/195802.

-
- [57] F. M. Brunbauer, E. Bertagnolli, and A. Lugstein. Gate-Tunable Electron Transport Phenomena in Al-Ge<111>-Al Nanowire Heterostructures. *Nano Letters*, 15(11):7514–7518, 2015. ISSN 1530-6984. doi: 10.1021/acs.nanolett.5b03169.
- [58] R. Pillarisetty. Academic and industry research progress in germanium nanodevices. *Nature*, 479(7373):324–328, 2011. ISSN 0028-0836. doi: 10.1038/nature10678.
- [59] S. M. Sze and K. K. Ng. *Physics of Semiconductor Devices*. John Wiley and Sons, 2006. ISBN 978-0-471-14323-9.
- [60] B. Yu, X. H. Sun, G. A. Calebotta, G. R. Dholakia, and M. Meyyappan. One-dimensional Germanium Nanowires for Future Electronics. *Journal of Cluster Science*, 17(4):579–597, 2006. ISSN 1040-7278. doi: 10.1007/s10876-006-0081-x.
- [61] R. H. Kingston. Review of germanium surface phenomena. *Journal of Applied Physics*, 27(2):101–114, 1956. doi: 10.1063/1.1722317.
- [62] Y. Kamata. High-k/Ge MOSFETs for future nanoelectronics. *Materials Today*, 11(1-2):30–38, 2008. ISSN 13697021. doi: 10.1016/S1369-7021(07)70350-4.
- [63] M. Grundmann. *The Physics of Semiconductors: An Introduction Including Devices and Nanophysics*. Springer, 2006. ISBN 978-3-540-25370-9.
- [64] D. B. Cuttriss. Relation Between Surface Concentration and Average Conductivity in Diffused Layers in Germanium. *Bell System Technical Journal*, 40(2): 509–521, 1961. ISSN 00058580. doi: 10.1002/j.1538-7305.1961.tb01627.x.
- [65] M. B. Prince. Drift mobilities in semiconductors. I. Germanium. *Physical Review*, 92(3):681–687, 1953.
- [66] W. W. Tyler and T. J. Soltys. General Electric Research Lab. *Memo Rept. No. P-193*.
- [67] J. Liu, X. Sun, L. C. Kimerling, and J. Michel. Direct-gap optical gain of Ge on Si at room temperature. *Optics Letters*, 34(11):1738, 2009. ISSN 0146-9592. doi: 10.1364/OL.34.001738.
- [68] C. Claeys and E. Simoen. *Germanium-Based Technologies: From Materials to Devices*. Elsevier Science, 2007. ISBN 978-0-08-044953-1.
- [69] S. M. Sze. *Physics of Semiconductor Devices*. John Wiley and Sons, 1981. ISBN 0-471-09837-X.
- [70] S. Luryi. Frequency limit of double-barrier resonant-tunneling oscillators. *Applied Physics Letters*, 47(5):490, 1985. ISSN 00036951. doi: 10.1063/1.96102.

- [71] M. Zhu, P. Chen, R. K. Y. Fu, Z. An, C. Lin, and P. K. Chu. Numerical study of self-heating effects of MOSFETs fabricated on SOAN substrate. *IEEE Transactions on Electron Devices*, 51(6):901–906, 2004.
- [72] D. Kazazis, A. Zaslavsky, E. Tutuc, N. A. Bojarczuk, and S. Guha. Negative differential resistance in ultrathin Ge-on-insulator FETs. *Semiconductor Science and Technology*, 22(1):S1–S4, 2006. ISSN 0268-1242. doi: 10.1088/0268-1242/22/1/S01.
- [73] M. K. Husain, X. V. Li, and C. H. de Groot. Observation of Negative Differential Conductance in a Reverse-Biased Ni/Ge Schottky Diode. *IEEE Electron Device Letters*, 30(9):966–968, 2009. ISSN 0741-3106. doi: 10.1109/LED.2009.2025673.
- [74] A. R. Hutson, A. Jayaraman, A. G. Chynoweth, A. S. Coriell, and W. L. Feldman. Mechanism of the Gunn Effect from a Pressure Experiment. *Physical Review Letters*, 14(16):639–641, 1965.
- [75] W. H. Brattain and J. Bardeen. Surface properties of germanium. *The Bell System Technical Journal*, 32(1):1–41, 1953.
- [76] Y. L. Sandler and M. Gazith. Surface Properties of germanium. *The Journal of Physical Chemistry*, 63(7):1095–1102, 1959.
- [77] M. D. Archer and A. J. Nozik. *Nanostructured and Photoelectrochemical Systems for Solar Photon Conversion*, volume 3 of *Series on Photoconversion of Solar Energy*. Imperial College Press, 2008. ISBN 978-1-86094-255-6.
- [78] F. P. Heiman and G. Warfield. The effects of oxide traps on the MOS capacitance. *IEEE Transactions on Electron Devices*, 12(4):167–178, 1965. ISSN 0018-9383. doi: 10.1109/T-ED.1965.15475.
- [79] W. Mönch. *Semiconductor Surfaces and Interfaces*. Springer, 2001. ISBN 978-3-642-08748-6. doi: 10.1007/978-3-662-04459-9.
- [80] L. Tsetseris and S. T. Pantelides. Morphology and defect properties of the Ge–GeO₂ interface. *Applied Physics Letters*, 95(26):262107, 2009. ISSN 00036951. doi: 10.1063/1.3280385.
- [81] M. Houssa, G. Pourtois, M. Caymax, M. Meuris, M. M. Heyns, V. V. Afanas’Ev, and A. Stesmans. Ge dangling bonds at the (100) Ge/ GeO₂ interface and the viscoelastic properties of GeO₂. *Applied Physics Letters*, 93(16):161909, 2008. ISSN 00036951. doi: 10.1063/1.3006320.
- [82] F. S. Minaye Hashemi, S. Thombare, F. M. Morral, M. L. Brongersma, and P.C. McIntyre. Effects of surface oxide formation on germanium nanowire

-
- band-edge photoluminescence. *Applied Physics Letters*, 102(25):251122, 2013. ISSN 00036951. doi: 10.1063/1.4812334.
- [83] D. Kuzum, T. Krishnamohan, A. J. Pethe, A. K. Okay, Y. Oshima, Y. Sun, J. P. McVittie, P. A. Pianetta, P. C. McIntyre, and K.C. Saraswat. Ge-Interface Engineering With Ozone Oxidation for Low Interface-State Density. *IEEE Electron Device Letters*, 29(4):328–330, 2008. ISSN 0741-3106. doi: 10.1109/LED.2008.918272.
- [84] A. Molle, Md. N. K. Bhuiyan, G. Tallarida, and M. Fanciulli. Formation and stability of germanium oxide induced by atomic oxygen exposure. *Materials Science in Semiconductor Processing*, 9(4-5):673–678, 2006. ISSN 13698001. doi: 10.1016/j.mssp.2006.09.002.
- [85] R. H. Kingston and A. L. McWhorter. Relaxation Time of Surface States on Germanium. *Physical Review*, 103(3):534–540, 1956. ISSN 0031-899X. doi: 10.1103/PhysRev.103.534.
- [86] T. Hanrath and B. A. Korgel. Influence of Surface States on Electron Transport through Intrinsic Ge Nanowires. *The Journal of Physical Chemistry B*, 109(12):5518–5524, 2005. ISSN 1520-6106. doi: 10.1021/jp044491b.
- [87] Z. Zhang and J. T. Yates. Band Bending in Semiconductors: Chemical and Physical Consequences at Surfaces and Interfaces. *Chemical Reviews*, 112(10):5520–5551, 2012. ISSN 0009-2665. doi: 10.1021/cr3000626.
- [88] P. Tsipas and A. Dimoulas. Modeling of negatively charged states at the Ge surface and interfaces. *Applied Physics Letters*, 94(1):012114, 2009. ISSN 00036951. doi: 10.1063/1.3068497.
- [89] J. T. Law. The Adsorption of Gases on a Germanium Surface. *The Journal of Physical Chemistry*, 59(6):543–549, 1955. ISSN 0022-3654. doi: 10.1021/j150528a015.
- [90] D. Wang and H. Dai. Germanium nanowires: from synthesis, surface chemistry, and assembly to devices. *Applied Physics A*, 85(3):217–225, 2006. ISSN 0947-8396. doi: 10.1007/s00339-006-3704-z.
- [91] A. Dimoulas, P. Tsipas, A. Sotiropoulos, and E. K. Evangelou. Fermi-level pinning and charge neutrality level in germanium. *Applied Physics Letters*, 89(25):252110, 2006. ISSN 00036951. doi: 10.1063/1.2410241.
- [92] S. Zhang, E. R. Hemesath, D. E. Perea, E. Wijaya, J. L. Lensch-Falk, and L. J. Lauhon. Relative Influence of Surface States and Bulk Impurities on the Electrical Properties of Ge Nanowires. *Nano Letters*, 9(9):3268–3274, 2009. ISSN 1530-6984. doi: 10.1021/nl901548u.

- [93] A. B. Greytak, L. J. Lauhon, M. S. Gudiksen, and C. M. Lieber. Growth and transport properties of complementary germanium nanowire field-effect transistors. *Applied Physics Letters*, 84(21):4176, 2004. ISSN 00036951. doi: 10.1063/1.1755846.
- [94] Q. Guo, A. Pospischil, M. Bhuiyan, H. Jiang, H. Tian, D. Farmer, B. Deng, C. Li, S. J. Han, H. Wang, Q. Xia, T. P. Ma, T. Mueller, and F. Xia. Black Phosphorus Mid-Infrared Photodetectors with High Gain. *Nano Letters*, 16(7): 4648–4655, 2016. ISSN 1530-6984. doi: 10.1021/acs.nanolett.6b01977.
- [95] H. Kosaka, D. S. Rao, H. D. Robinson, P. Bandaru, T. Sakamoto, and E. Yablonovitch. Photoconductance quantization in a single-photon detector. *Physical Review B*, 65(20):201307, 2002. ISSN 0163-1829. doi: 10.1103/PhysRevB.65.201307.
- [96] S. Thunich, L. Prechtel, D. Spirkoska, G. Abstreiter, A. Fontcuberta i Morral, and A. W. Holleitner. Photocurrent and photoconductance properties of a GaAs nanowire. *Applied Physics Letters*, 95(8):083111, 2009. ISSN 00036951. doi: 10.1063/1.3193540.
- [97] R. Soref. Mid-infrared photonics in silicon and germanium. *Nature Photonics*, 4(8):495–497, 2010. ISSN 1749-4885. doi: 10.1038/nphoton.2010.171.
- [98] A. Barski, M. Derivaz, J. L. Rouviere, and D. Buttard. Epitaxial growth of germanium dots on Si(001) surface covered by a very thin silicon oxide layer. *Applied Physics Letters*, 77(22):3541, 2000. ISSN 00036951. doi: 10.1063/1.1328771.
- [99] H. Jagannathan, M. Deal, Y. Nishi, J. Woodruff, C. Chidsey, and P. C. McIntyre. Nature of germanium nanowire heteroepitaxy on silicon substrates. *Journal of Applied Physics*, 100(2):024318, 2006. ISSN 00218979. doi: 10.1063/1.2219007.
- [100] J. C. Bean. Strained-Layer Epitaxy of Germanium-Silicon Alloys. *Science*, 230 (4722):127–131, 1985.
- [101] C. J. Kim, H. S. Lee, Y. J. Cho, K. Kang, and M. H. Jo. Diameter-Dependent Internal Gain in Ohmic Ge Nanowire Photodetectors. *Nano Letters*, 10(6): 2043–2048, 2010. ISSN 1530-6984. doi: 10.1021/nl100136b.
- [102] H. S. Lee, C. J. Kim, D. Lee, R. R. Lee, K. Kang, I. Hwang, and M. H. Jo. Large Electroabsorption Susceptibility Mediated by Internal Photoconductive Gain in Ge Nanowires. *Nano Letters*, 12(11):5913–5918, 2012. ISSN 1530-6984. doi: 10.1021/nl3033203.
- [103] L. Wang and P. Asbeck. Analysis of photoelectronic response in semiconductor nanowires. *2006 Sixth IEEE Conference on Nanotechnology*, 2:716–719, 2006.

-
- [104] R. S. Chen, H. Y. Chen, C. Y. Lu, K. H. Chen, C. P. Chen, L. C. Chen, and Y. J. Yang. Ultrahigh photocurrent gain in m-axial GaN nanowires. *Applied Physics Letters*, 91(22):223106, 2007. ISSN 00036951. doi: 10.1063/1.2817595.
- [105] J. D. Prades, F. Hernandez-Ramirez, R. Jimenez-Diaz, M. Manzanares, T. Andreu, A. Cirera, A. Romano-Rodriguez, and J. R. Morante. The effects of electron-hole separation on the photoconductivity of individual metal oxide nanowires. *Nanotechnology*, 19(46):465501, 2008. ISSN 0957-4484. doi: 10.1088/0957-4484/19/46/465501.
- [106] J. S. Jie, W. J. Zhang, Y. Jiang, X. M. Meng, Y. Q. Li, and S. T. Lee. Photoconductive Characteristics of Single-Crystal CdS Nanoribbons. *Nano Letters*, 6(9):1887–1892, 2006. ISSN 1530-6984. doi: 10.1021/nl060867g.
- [107] G. Konstantatos, M. Badioli, L. Gaudreau, J. Osmond, M. Bernechea, F. P. G. de Arquer, F. Gatti, and F. H. L. Koppens. Hybrid graphene-quantum dot phototransistors with ultrahigh gain. *Nature Nanotechnology*, 7(6):363–368, 2012. ISSN 1748-3387. doi: 10.1038/nnano.2012.60.
- [108] M. M. Furchi, D. K. Polyushkin, A. Pospischil, and T. Mueller. Mechanisms of Photoconductivity in Atomically Thin MoS₂. *Nano Letters*, 14(11):6165–6170, 2014. ISSN 1530-6984. doi: 10.1021/nl502339q.
- [109] H. Sakaki. Scattering Suppression and High-Mobility Effect of Size-Quantized Electrons in Ultrafine Semiconductor Wire Structures. *Japanese Journal of Applied Physics*, 19(12):L735–L738, 1980. ISSN 0021-4922. doi: 10.1143/JJAP.19.L735.
- [110] H. S. Kang, C. S. Choi, W. Y. Choi, D. H. Kim, and K. S. Seo. Characterization of phototransistor internal gain in metamorphic high-electron-mobility transistors. *Applied Physics Letters*, 84(19):3780, 2004. ISSN 00036951. doi: 10.1063/1.1739278.
- [111] Y. Y. Noh, D. Y. Kim, Y. Yoshida, K. Yase, B. J. Jung, E. Lim, and H. K. Shim. High-photosensitivity p-channel organic phototransistors based on a biphenyl end-capped fused bithiophene oligomer. *Applied Physics Letters*, 86(4):043501, 2005. ISSN 00036951. doi: 10.1063/1.1856144.
- [112] J. A. Garrido, E. Monroy, I. Izpura, and E. Muñoz. Photoconductive gain modelling of GaN photodetectors. *Semiconductor Science and Technology*, 13(6):563–568, 1998. ISSN 0268-1242. doi: 10.1088/0268-1242/13/6/005.
- [113] C. H. Lin, R. S. Chen, T. T. Chen, H. Y. Chen, Y. F. Chen, K. H. Chen, and L. C. Chen. High photocurrent gain in SnO₂ nanowires. *Applied Physics Letters*, 93(11):112115, 2008. ISSN 00036951. doi: 10.1063/1.2987422.

- [114] L. Cao, J. S. White, J. S. Park, J. A. Schuller, B. M. Clemens, and M. L. Brongersma. Engineering light absorption in semiconductor nanowire devices. *Nature Materials*, 8(8):643–647, 2009. ISSN 1476-1122. doi: 10.1038/nmat2477.
- [115] L. Cao, P. Fan, A. P. Vasudev, J. S. White, Z. Yu, W. Cai, J. A. Schuller, S. Fan, and M. L. Brongersma. Semiconductor Nanowire Optical Antenna Solar Absorbers. *Nano Letters*, 10(2):439–445, 2010. ISSN 1530-6984. doi: 10.1021/nl9036627.
- [116] L. Cao, J. S. Park, P. Fan, B. Clemens, and M. L. Brongersma. Resonant Germanium Nanoantenna Photodetectors. *Nano Letters*, 10(4):1229–1233, 2010. ISSN 1530-6984. doi: 10.1021/nl9037278.
- [117] S. Kral. *Herstellung und Charakterisierung von monolithischen Germanium-Nanodraht-Bauelementen mit Metall-Halbleiter-Heteroübergang*. Master’s thesis, TU Wien, 2014.
- [118] M. Law, L. E. Greene, A. Radenovic, T. Kuykendall, J. Liphardt, and P. Yang. ZnO-Al₂O₃ and ZnO-TiO₂ Core-Shell Nanowire Dye-Sensitized Solar Cells. *The Journal of Physical Chemistry B*, 110(45):22652–22663, 2006. ISSN 1520-6106. doi: 10.1021/jp0648644.
- [119] D. E. Aspnes and A. A. Studna. Dielectric functions and optical parameters of Si, Ge, GaP, GaAs, GaSb, InP, InAs, and InSb from 1.5 to 6.0 eV. *Physical Review B*, 27(2):985–1009, 1983. ISSN 0163-1829. doi: 10.1103/PhysRevB.27.985.
- [120] S. Datta. *Quantum Transport: Atom to Transistor*. Cambridge University Press, 2005. ISBN 978-0-521-63145-7.
- [121] C. W. Lee, A. Afzalain, N. D. Akhavan, R. Yan, I. Ferain, and J. P. Colinge. Junctionless multigate field-effect transistor. *Applied Physics Letters*, 94(5):053511, 2009. ISSN 00036951. doi: 10.1063/1.3079411.
- [122] J. P. Colinge, C. W. Lee, A. Afzalain, N. D. Akhavan, R. Yan, I. Ferain, P. Razavi, B. O’Neill, A. Blake, M. White, A. M. Kelleher, B. McCarthy, and R. Murphy. Nanowire transistors without junctions. *Nature Nanotechnology*, 5(3):225–229, 2010. ISSN 1748-3387. doi: 10.1038/nnano.2010.15.
- [123] K. Byon, D. Tham, J. E. Fischer, and A. T. Johnson. Systematic study of contact annealing: Ambipolar silicon nanowire transistor with improved performance. *Applied Physics Letters*, 90(14):143513, 2007. ISSN 00036951. doi: 10.1063/1.2720309.
- [124] L. Zhang, H. Li, Y. Guo, K. Tang, J. Woicik, J. Robertson, and P. C. McIntyre. Selective Passivation of GeO₂/Ge Interface Defects in Atomic Layer Deposited

-
- High- k MOS Structures. *ACS Applied Materials & Interfaces*, 7(37):20499–20506, 2015. ISSN 1944-8244. doi: 10.1021/acsami.5b06087.
- [125] S. Zafar, A. Callegari, E. Gusev, and M. V. Fischetti. Charge trapping related threshold voltage instabilities in high permittivity gate dielectric stacks. *Journal of Applied Physics*, 93(11):9298, 2003. ISSN 00218979. doi: 10.1063/1.1570933.
- [126] W. Zhang, C. P. Chuu, J. K. Huang, C. H. Chen, M. L. Tsai, Y. H. Chang, C. T. Liang, Y. Z. Chen, Y. L. Chueh, J. H. He, M. Y. Chou, and L. J. Li. Ultrahigh-Gain Photodetectors Based on Atomically Thin Graphene-MoS₂ Heterostructures. *Scientific Reports*, 4:1–8, 2014. ISSN 2045-2322. doi: 10.1038/srep03826.
- [127] C. Soci, A. Zhang, B. Xiang, S. A. Dayeh, D. P. R. Aplin, J. Park, X .Y. Bao, Y. H. Lo, and D. Wang. ZnO Nanowire UV Photodetectors with High Internal Gain. *Nano Letters*, 7(4):1003–1009, 2007. ISSN 1530-6984. doi: 10.1021/nl070111x.
- [128] G. Konstantatos and E. H. Sargent. PbS colloidal quantum dot photoconductive photodetectors: Transport, traps, and gain. *Applied Physics Letters*, 91(17):173505, 2007. ISSN 00036951. doi: 10.1063/1.2800805.
- [129] O. Christensen. Quantum efficiency of the internal photoelectric effect in silicon and germanium. *Journal of Applied Physics*, 47(2):689, 1976. ISSN 00218979. doi: 10.1063/1.322635.

